Monographs of the School of Doctoral Studies in Environmental Engineering
12

Hydrothermodynamics of a small alpine lake

Giuliano Rizzi

UNIVERSITÀ DEGLI STUDI DI TRENTO

2008

Based on the Doctoral thesis in Environmental Engineering (XV cycle)
defended in February 2004 at the Faculty of Engineering, University of Trento.
Academic year 2002/2003
Supervisor: prof. Marco Tubino

On the cover: Lake Tovel (Trentino, Italy)

Direttore della collana: Alberto Bellin
Segreteria di redazione: Laura Martuscelli
Dipartimento di Ingegneria Civile e Ambientale
Università degli Studi di Trento, Italia
Maggio 2008

ISBN: 978-88-8443-246-9

To my primary schoolteacher:
for her so important teaching...

Acknowledgements

I thank first at all my parents for supporting me in these years.

Special thanks to Silvia that I have met during the period dedicated to the doctoral researches.

Great acknowledgements to my friends and companions in adventure (Marco, Gianlinux, Gianduca, Walter, Z, Michele, Max, Lupo, ... I sure forget someone) and to students that have shared with me lakes studies: without their help I will not able to finish this work.

I can't leave out to acknowledge Marco Tubino, specially when he strives to be a friend.

Finally, I just want to thank people who never gets recognition for that are they doing: it is hidden but is still more indispensable...

And most of all, I thank the One who has taken care of me in the difficult way of my life .

Contents

List of Figures

List of Tables

Foreword

The present research is aimed at investigating the hydrothermodynamic properties of small alpine lakes, with specific reference to the case of lake Tovel (Trentino, Italy). The lake was subject to a spectacular reddening which had been occurring each year until 1964, when the phenomenon suddenly ceased.

The work has been developed within the framework of the research project "SALTO", funded by "Provincia Autonoma di Trento" which is oriented to the study of different ecological, biological and physical aspects of lake Tovel, along with his historical development.

The present thesis is divided in three parts.

In the first part we summarize the fundamental processes which characterize the hydrothermodynamics of lakes, which specific reference to those aspects that we have also investigated through field measurements.

In the second part a detailed report is given on the procedures and results of the field campaign performed during the year 2003 on lake Tovel. In particular, the experimental techniques are illustrated along with the data post-processing procedures. The temperature data measured by thermistor chains and velocity data collected through current meter and profiler are then analysed to provide a quantitative estimate of the main circulations that may develop within the lake, due to different meteorological conditions.

Finally, the third part is devoted to numerical modelling. Results of a 1-D vertical model and of a 3-D model are discussed. The former model (DYRESM), developed in Western Australia University, has been used to study the seasonal evolution of the lake; the latter has been specifically developed in the framework of this project to investigate the hydrodynamic behaviour of small lakes on short time scale. The results of numerical simulation display a fairly good agreement with observed data.

Part I.

Literature review

1. Physical Limnology: introduction

1.1. Basic characteristics of lakes

The hydrodynamics of lakes is strictly connected with the temperature profile that develops in each water body characterized by low mixing. In fact, the motion of currents of a stratified fluid is much different with respect to the motion in homogeneous fluids affected by external forcing. Another basic characteristic of lakes is the lack of well defined currents or a single direction of the flow, as in rivers. Lakes are named "lentic" systems from *lenis*, that means calm, because gravity force does not move directly the water and flow doesn't dominate transport and mixing phenomena as in streams (called "lotic" systems from *lotus*, that means washed).

While the flowing nature of rivers dominates their transport and causes the complete mixing over the depth and width, the standing nature of lakes tends to move water quality constituents and contaminants slowly. Moreover, the stratification retards vertical mixing. In almost all cases wind mixing and solar heating dominate gravity-driven flow. (Martin and McCutcheon, 1999)

Most lakes become stratified as the solar energy is input at the surface; due to the dependence of water behaviour on temperature, this thermal energy is converted to a mechanical stability that inhibits water motion (Imberger and Patterson, 1990).

The stronger is the thermal insolation, the stronger is the stratification and, in general, more quiescent is the water body. Wind, stream inflows and outflows, all modify the stratification.

The dynamic balance in a lake could be considered similar to that of an engine; the disturbing forces work against the potential energy gradient set up by radiation. The internal dynamics of this engine is extremely inefficient, in fact up to 90% of this mechanical energy (usually provided by winds) is lost to dissipation (Imboden and Wuest, 1995).

Temperature in lakes is significantly affected by river valley inflows, outflows and underground springs, but the most important external forcing is generally due to heat transfers at the surface. Short wave solar radiation (of wavelength ranging between $300nm$ to

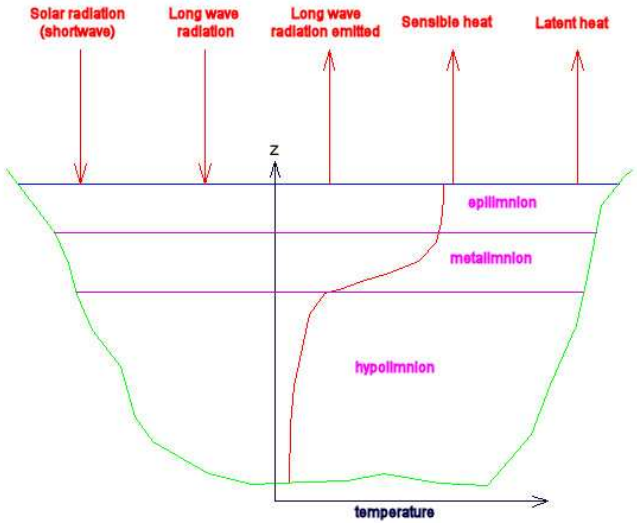

Figure 1.1.: Main energetic fluxes on the lake

$1000nm$) and long wave radiation (of wavelength greater than $1000nm$) emitted by clouds and atmospheric water vapor heat the water. Other mechanisms, like evaporation, sensible heat transfer and back radiation from the surface, cool the superficial water in a dynamic equilibrium. The net heat input from these sources depends on the season and the meteorological conditions: this balance may change suddenly as the weather conditions change (Imberger, 1994).

Other important forcings are inflows and outflows: they are responsible of water level in lakes, temperature and water supplies and mixing.

In terms of the above fluxes, a fundamental parameter can be defined, the hydraulic residence time.

The hydraulic residence time τ_w, which is a measure of the average time that a water particle resides within a lake or impoundment, is defined as the ratio between the mean water volume V and the mean flow Q (total rate flow of all inflows or outflows):

$$\tau_w = \frac{V}{Q}. \tag{1.1}$$

This ratio only provides a rough estimate since stratification and short circuit phenomena may confine the change only in the superficial layers, specially in big lakes or where the morphological context is complex, while deep waters can remain in the basin for very long time. In fact the time required for the complete flushing of a lake varies typically

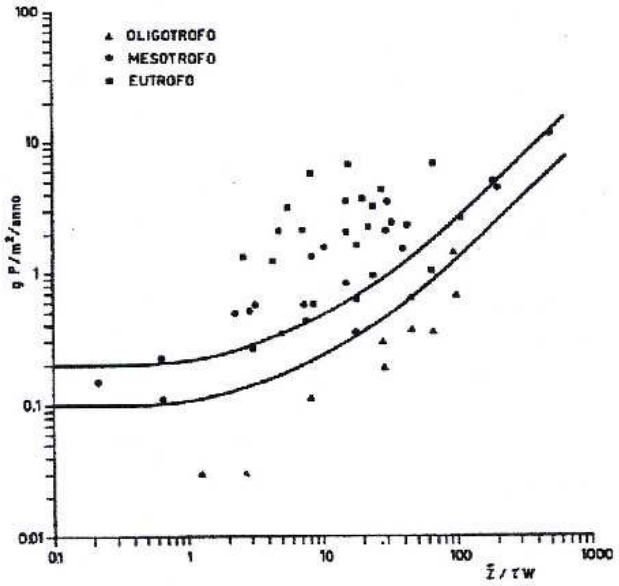

Figure 1.2.: Comparison between phosphorous loading rate q and mean depth versus residence time ratio z/τ_w.

from 10 to 10.000 days while the mixing across the thermocline can take up to 100.000 days: for instance, the lake Zurich displays a residence time equal to 400 days, which is much shorter than 7000 days required for the complete mixing when the lake is stratified (Martin and McCutcheon, 1999).

Another "global" parameter characterizing lakes is the mean depth, defined as:

$$\overline{z} = \frac{V}{A}, \tag{1.2}$$

where A is the surface area.

The mean depth and the hydraulic residence time largely influence the mixing and water quality characteristics of lakes and reservoirs. It may worth noticing that the classification proposed by Vollenweider in the end of '70s in terms of the eutrophication potential of a lake is simply based on the hydraulic retention time, mean depth and phosphorus loading rate (figure 1.2).

In terms of the above parameters it is possible to draw a simplified trophic classification and foresee potential algae blooms or anoxic conditions.

1.2. Thermal forcing

The thermal behaviour and heat balance of lakes are dependent in many ways on the unique thermal properties of water. The high specific heat of water allows dissipation of light energy and accumulation of heat. Factors that determine the retention of heat and concurrently influence the distribution of heat within the lake system include wind energy, currents and other water movements, morphometry of the basin and water losses (Wetzel, 1983).

The heat balance of a lake is made up of several components including short-wave radiation, long-wave radiation, back radiation, sensible heat exchange, and latent heat exchange (Martin and McCutcheon, 1999).

1.2.1. Short-wave solar radiation

Short-wave solar radiation constitutes the greatest source of heat to lakes and is the major energy source driving the productivity of aquatic ecosystems (Wetzel, 1983). The sun provides short-wave radiation, which passes through the atmosphere, eventually reaching the earth's surface. The intensity of solar energy impinging on water bodies is dependent on the damping effect of the atmosphere, the altitude of the sun (which varies according to latitude on a daily and seasonal basis), and the reflection from the water surface (Martin and McCutcheon, 1999).

Short-wave radiation consists of two components, penetrative and non-penetrative, whose behaviour depend on the wavelength. Solar radiation that penetrates the water surface is absorbed by the water. The absorption, and thus the heating of the water, takes place over a considerable depth due to the relative transparency of water to light in the visible spectrum. The depth distribution of the radiation can be expressed in exponential form using Beer's law, which reads (Ragotzkie, 1978):

$$I_z = I_0 \, e^{-k \, z}, \tag{1.3}$$

where $I_z$is the intensity of radiation at depth z, I_0 is the intensity at the surface and k is an extinction coefficient.

The extinction coefficient depends on the transparency of water and is therefore related to trophism of pools.

In the limnological literature the following values are found, (Spence, 1981):

A simple method is often used to estimate extinction coefficient, namely the Secchi depth measurements. According to this technique a Secchi disk (a round plate with alternating

Table 1.1.: Extinction coefficients for different water quality.

condition	k **values** $[m^{-1}]$
pure water	0.03
oligotrophic lake	0.1 - 0.2
mesotrophic lake	0.3 - 0.4
eutrophic lake	0.5 - 4.

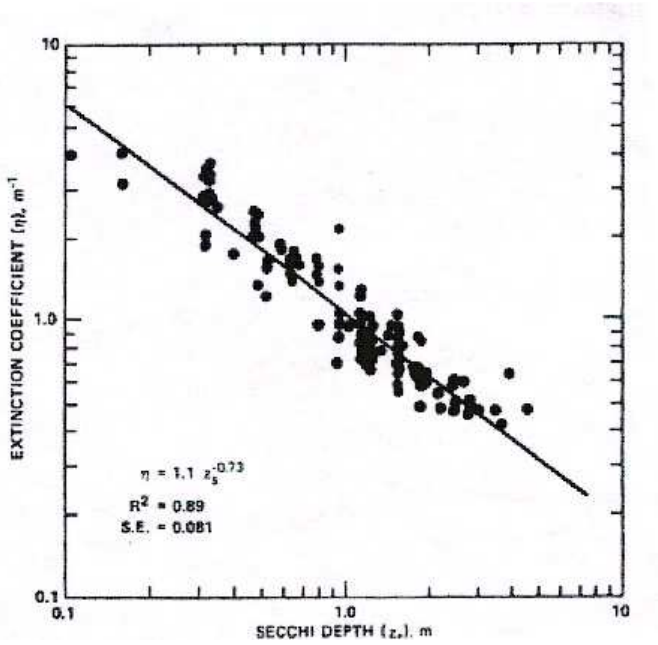

Figure 1.3.: Relationship between Secchi depth z [m] for the extinction coefficient η $[m^{-1}]$.

white and black arcs) is lowered through the water until it becomes no more visible; furthermore an empirical relationship is formulated which links this depth to the extinction coefficient (Williams, 1980), as shown in figure 1.3.

The reflection coefficient of short-wave radiation is termed the albedo of the substance. This coefficient varies from lake to lake and depends on the angle of the sun, the lake colour and the surface wave state (Hamilton and Schladow, 1996). The albedo value ranges from 0, indicating no reflection, to 1, meaning 100% reflection.

1.2.2. Long-wave radiation

Due to its relatively low absolute temperature, water experiences heat losses through the emission of long-wave radiation. On cloudy days, the effects of long-wave radiation are most pronounced, and are often the greatest source of heat at the water surface (Martin and McCutcheon, 1999).

The Stefan-Boltzman law is used to estimate the emission of long-wave radiation from the surface of the water body:

$$Q_{lw} = \epsilon_w \sigma T_w^4, \tag{1.4}$$

where ε_w is the emissivity of the water surface ($\simeq 0.96$), which is close to that of a black body, σ is the Stefan-Boltzman constant ($\sigma = 5.6697 \cdot 10^{-8}\ Wm^{-2}K^{-4}$) and T_w is the absolute temperature of the water surface (Antenucci and Imerito, 2001).

1.2.3. Sensible heat flux

Sensible heat transfer refers to the transport of heat due to conduction and convection processes occurring between the lake and the atmosphere. Heat is transferred across the water's surface by conduction to or from the air at the air/ water boundary. This conduction occurs only in a very thin layer of water or air at the boundary and depends directly on the temperature gradient across that boundary (Ragotzkie, 1978). Sensible heat can also be transferred by turbulence or convective processes in both air and water. The following expression is used:

$$Q_{sh} = C_s \rho_a C_p U_a \left(T_a - T_s\right), \tag{1.5}$$

where Q_{sh} is the sensible heat flux, C_s is the sensible heat transfer coefficient ($C_s = 1.3 \cdot 10^{-3}$), ρ_a is the density of air ($\rho_A = 1.2 kgm^{-3}$), C_p is the specific heat of water ($C_p = 4200 Jkg^{-1}{}^{\circ}C^{-1}$), U_a is the wind speed at the water surface in ms^{-1}, T_a is the temperature of air, T_s is the temperature of the surface water.

These transfer processes are also controlled by the wind and the stability of the overlying air. When the water is cooler than the overlying air, the air is cooled from below and has the tendency to become stably stratified. This causes a reduction or complete elimination of wind action on the lake, thereby decreasing heat transfer. When the lake is warmer than the air above, convection is activated and sensible heat transfer is intensified (Ragotzkie, 1978).

1.2.4. Latent heat flux

Evaporation is one of the major source of heat loss for lakes. The heat loss can be determined from the density of the water being evaporated, the latent heat of the water and the rate of evaporation. The latent heat of evaporation is weakly dependent on water temperature, while the amount of evaporation is proportional to the water vapour pressure gradient between the water atmosphere interface (Martin and McCutcheon, 1999). Calm meteorological conditions allow the rapid attainment of equilibrium between the water vapour pressure and the air immediately above the surface of the water. Then the rate of vapour diffusion away from the surface layer plays a regulating role in the evaporation rate. However, wind induced turbulence both in the water and in atmosphere enhances the transport. The transfer rate is then a function of the wind speed close to the water surface.

Latent heat flux Q_l can be expressed using the following formula (Hamilton and Schladow, 1996):

$$Q_l = -\rho_a \; L_w \; C_L \; U_a \; \left(e_a - e_w\right), \tag{1.6}$$

where C_L is the latent coefficient, e_a is the saturated vapor pressure at the water surface temperature and e_w is the vapor pressure at the air temperature, L_w is the latent heat of evaporation ($L_w \approx 2.4 \; \cdot 10^6 J \; Kg^{-1}$) and U_a is the wind velocity.

1.2.5. The cycle of thermal stratification

The majority of lakes shows some degree of thermal stratification for at least 9 months of the year. Thermal stratification occurs when mixing due to wind and inflows or outflows becomes dominated by solar heating. Thermal stratification mainly occurs in the vertical direction (Imberger, 1994), but stratification may also occur in the horizontal plane ("thermal obstacle" phenomena, see figure 5.11).

Density stratification between the epilimnion and hypolimnion occurs as a result of the relationship between water density and temperature and salinity:

$$\rho = \rho(S, T). \tag{1.7}$$

In fresh water salinity can be neglected and the water density depends only on temperature through the following expression:

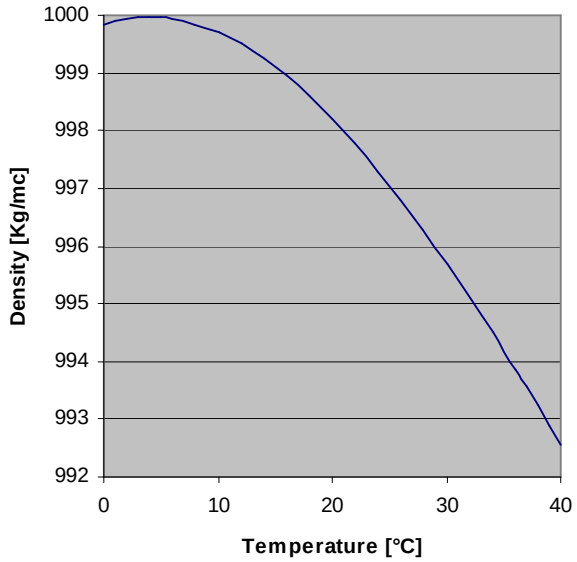

Figure 1.4.: Relationship between water temperature and density

$$\rho(T) = 999.84298 + 10^{-3}\left(65.4891\,T - 8.56272\,T^2 + 0.059385\,T^3\right), \tag{1.8}$$

where ρ is in $kg\,m^{-3}$ and T in C; this behaviour is responsible for the floatation of ice and the inverted winter stratification.

Between 0C density increases with increasing temperature; as water temperature increases from 4C (boiling), density decreases nonlinearly. A temperature difference of few degrees results in a pronounced density difference, which is able to create stratification in lakes and reservoirs. Stratification tends to be more prominent during summer heating because wind and currents from inflows and outflows do not have sufficient energy to erode the density differences that arise (Martin and McCutcheon, 1999).

Stable vertical stratification is attained when the water column is heavier near the bottom than near the surface. This separation of layers constrains the vertical motions within the lake, allowing the fluid to move or mix vertically only to the extent that the input energy can overcome the internal dissipation and the potential energy associated with the stratification. The stratification also supports internal waves, which are able to propagate over large distances distributing kinetic energy and momentum. Thus, the motion within a stratified lake results from the interplay between four dominant disturbances (wind,

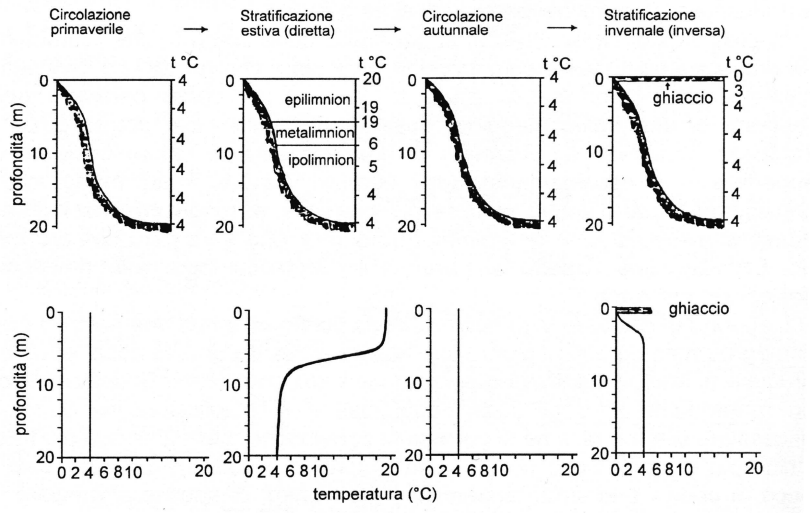

Figure 1.5.: Stratification and destratification cycle in temperate zones.

inflow, outflow, differential heating), the potential energy of the resident stratification, the bathymetry of the lake and the earth's rotation, if the lake is sufficiently large (Imberger, 1994). The effect of Coriolis's forces can be neglected whenever the inertial Rossby radius $R_r = \frac{c_i}{f}$, namely the ratio between the wave speed c_i and the inertial frequency $f = 2\Omega \sin\Phi$ (Ω being the velocity of Earth rotation and Φ the latitude), is much larger than the basin dimension.

The water column of a lake is conventionally separated into three layers: epilimnion, metalimnion and hypolimnion.

In temperate climate, typical temperature profiles in lakes follow the well-known cycle of stratification and destratification reported in figure 1.5 (Tonolli, 1964).

When heat enters the water surface faster than it is mixed over the depth, stratification begins. Heating usually begins in spring or early summer at the latest. The surface layer heats more rapidly and becomes less dense than deeper waters. The increasing vertical-density differences further decrease vertical mixing. Stable stratification sets up and persists until fall. However, even after stratification sets up, there is normally sufficient energy from wind and currents to mix the upper layer and erode the thermocline to form a well-mixed epilimnion (Martin and McCutcheon, 1999).

Below there is another well mixed cooler layer, called hypolimnion. These two layers are separated by the metalimnion or thermocline, where the maximum vertical temperature

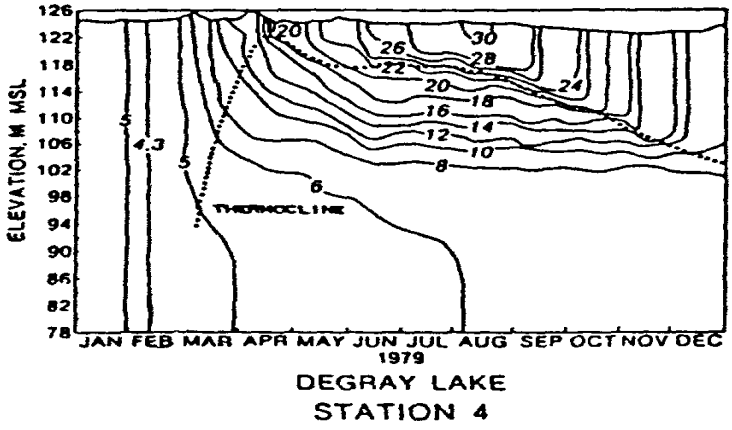

Figure 1.6.: Thermocline seasonal moving.

gradients occur. The thermocline is usually defined as the region where a minimum of 1°C temperature change per meter of depth occurs. Late spring and summer storms can episodically lower the thermocline, but generally the thermocline rises nearer the surface as solar heating continues. After midsummer solar radiation decreases and consequently epilimnion cools; the thermocline begins to deepen until fall overturn occurs, when the weakened difference in density within the hypolimnion allows for more mixing (Martin and McCutcheon, 1999).

In addition, other layers can be individuated: the diurnal mixed layer and the diurnal thermocline (Imberger, 1985a). The diurnal mixed layer is a very small surface region in which the temperature appears to actively mix, located at the top of the epilimnetic layer. The diurnal thermocline (normally located within the epilimnion also) is a gradient region, resulting from the daily solar heating and differs from the seasonal thermocline, which is the sharp gradient region within the stepped structure of the metalimnion.

In cold regions or in mountain lakes inverse temperature stratification may occur when 4°

C water remains on the bottom of the lake and the surface waters become cooler and less dense. Once the lake freezes,the ice cover prevents wind mixing and the erosion of the density differences. Surface layers close to the ice keep nearly at 0°

C. Inverse stratification is so mild that is not possible to recognize a distinct thermocline and the epilimnion and hypolimnion are not well defined. This kind of stratification may persist until spring warming heats the surface layer. As the temperature approaches that

of the hypolimnion, usually 4°

C, spring overturn occurs and a new stratification cycle begins.

In terms of thermal stratification, lakes can be classified as following (Martin and McCutcheon, 1999):

1. **Holomictic** lakes are those in which the entire water column completely mixes during the year;

2. **Meromictic** lakes do not mix completely and exhibit a deep stratum underneath that is completely stagnant; meromixis can result from chemical, biological or physical effects and meromictic lakes often have oxygen-depleted hypolimnion;

3. **Monomictic** lakes mix only once a year. For instance, at high elevations or latitudes, the temperature of lakes may never exceed 4°

   C, which implies that mixing can occur once during summer months, while at lower elevations or latitudes lakes may never reach temperatures below 4°

   C, in which case lakes may stratify during the summer months and then mix freely during winter. The latter are referred to as cold monomictic lakes while the former are referred to as warm monomictic lakes;

4. **Dimictic** lakes mix twice a year and are the typical lakes in temperate regions;

5. **Polymictic** lakes have frequent or continuous complete mixing. These lakes often display more variable vertical water quality distributions, being uniform during times of complete mixing;

6. **Oligomictic** lakes, which are typical of tropical regions, keep stratified almost continuously and rarely mix;

7. **Amictic** lakes never mix, due to the large density induced by high dissolved solids concentrations.

The above classification is reported in figure 1.7 in terms of the geographic location (Wetzel, 1983).

1.2.6. Stability of stratification

Stability is a measure of the amount of work required to attain thermal uniformity within the water column of a lake. Basically, it quantifies the resistance of stratification to disrup-

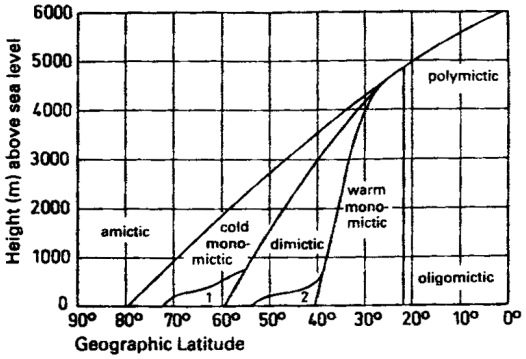

Figure 1.7.: Thermal kind of lakes respect to geographical location.

tion by the wind and thus the extent to which the hypolimnion is isolated from epilimnetic and superficial movements (Wetzel, 1983).

In general, the difference in temperature between the top and bottom of a stratified lake is the lowest near the equator, reaches a maximum at approximately 30°

latitude and then declines. If the change in density were constant across temperature, this latitudinal trend in the range of water column temperatures would be reflected in a similar trend of water column stabilities (Lewis, 1987). The rate of change in density with temperature, however, increases substantially above 4°

C. This variation causes the stability associated with a given temperature range to be stronger at high temperatures. Therefore, two factors affect the latitudinal trends in stability, the range of temperature and the mean temperature.

The thickness of the mixed layer of a temperate lake is quite stable during the season of maximum heat content. In fact, temperate lakes are stable within the mixed layer until seasonal heat loss begins, in autumn. The absolute stability of layers in temperate lakes is therefore high enough to prevent a variation of the thickness of the mixed layer due to frontal events causing alternating loss and gain of heat from the water column (Lewis, 2000).

The erosion of the metalimnion due to superficial currents associated with wind shear gets on until the mixed layer has thickened sufficiently to ensure that the turbulence induced by water movement under the influence of wind stress is counterbalanced by the magnitude of the density gradient. The water column then stabilizes until there is a reversal in heat budget during cooling periods. A secondary thermocline within the mixed layer is likely to develop, resulting in a new mixed layer, which is thinner than the seasonal one (Lewis,

1987).

If the mixed layer of a lake is fairly stable, as it is typical of temperate lakes, primary producers cannot use nutrients lost from the epilimnion until the autumn mixing, except for small quantities that are transferred by eddy diffusion from the metalimnion into the mixed layer.

The stratification stability can be defined in terms of the buoyancy frequency of Brunt-Vaisala, which takes the following form:

$$N^2 = -\frac{g}{\rho_0}\frac{\partial \rho}{\partial z}, \tag{1.9}$$

where g is the acceleration due to gravity, ρ_0 is the mean density and the minus sign is included to make N^2 positive for a stable gradient. The parameter N^{-1} represents the time scale for a particle displaced from its original position in a stratified fluid to return to its stable position under the effect of gravity (Imberger, 1994).

A bulk value of the above frequency can be defined as follows:

$$N^2 = \frac{g^*}{\Delta z}, \tag{1.10}$$

where g^* is the modified gravity acceleration across the upper most thermocline, which reads:

$$g^* = -g\frac{\Delta \rho}{\rho_0}, \tag{1.11}$$

$\Delta\rho$ is the density difference across the thermocline and ρ_0 is the hypolimnion density.

The Brunt Vaisala frequency is used to define a non-dimensional number, the Richardson number,which expresses the resistance that stratification opposes to shear mixing of two layers within density differences:

$$Ri = \frac{N^2}{S^2}, \tag{1.12}$$

where

$$S = \frac{\partial u}{\partial z} \tag{1.13}$$

is the velocity shear.

A further indicator which is commonly used to describe the strength of stratification is the Schmidt stability dimensional index, St. It represents the stability of the lake in terms of the amount of work required to mix the entire water body to a uniform density without adding or subtracting heat (Hutchinson, 1957). St is defined in the following form:

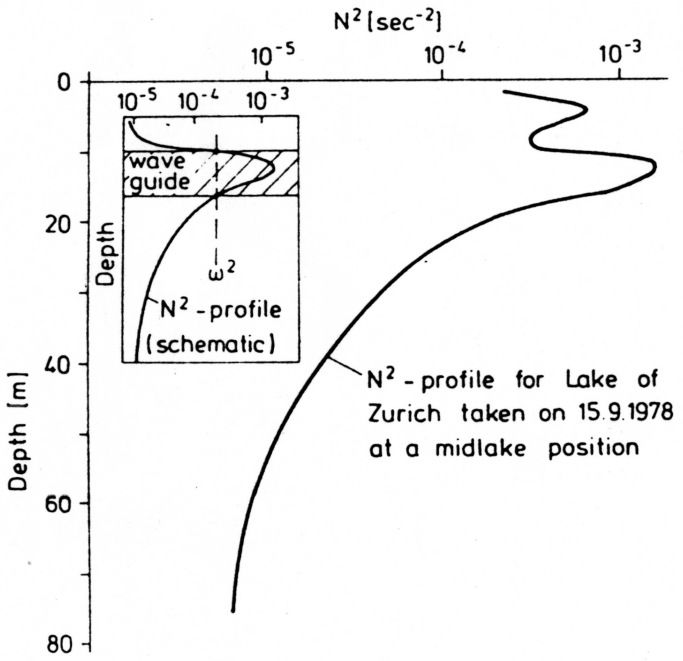

Figure 1.8.: Typical buoyancy frequency. For the selected ω, waves can only exist in the indicated band

$$S_t = \frac{1}{\rho_0} \int_0^{z_m} g\,(z - z_g)\;\; A\,(z)\;\; \rho\,(z)\;\; dz, \tag{1.14}$$

where z_m is the water depth, z is the vertical coordinate from the bottom of the lake, $A(z)$ is the lake surface at height z, $\rho(z)$ is the water density at height z, and z_g is the height of the centre of volume of the lake, given by:

$$z_g = \frac{\int_0^{z_m} z\;\; A\,(z)\;\; dz}{\int_0^{z_m} A\,(z)\;\; dz}. \tag{1.15}$$

Notice that St does not actually describe the amount of mixing, because it only takes into account the strength of stratification. Even in the case of very low stability values, which correspond to weak density stratification, a lake may experience negligible mixing if low wind velocities are present (Cacciatori, 2000).

1.3. Wind action

The degree of thermal stratification in a water body influences the physical response of a lake or reservoir to the surface wind stress. The wind acting on the surface, during the period of stratification, imparts both momentum and turbulent kinetic energy to the water in the surface layer (Imberger, 1985b). The turbulent mixing then causes the momentum to be distributed vertically downward, initiating a general motion in the surface layer in the direction of the wind. The water movement displaces the metalimnion downward at the downwind end and causes upwelling at the upwind end of the lake. This process continues until the baroclinic pressure gradient, associated with the tilted metalimnion, begins to counter-balance the introduced inertia, inducing a long internal wave response. In general the vertical mode "one" is excited, though higher modes may also be excited: the relative importance of the different modes may depend on the shape of the lake and the strength, duration and distribution of the wind field (Saggio and Imberger, 1998).

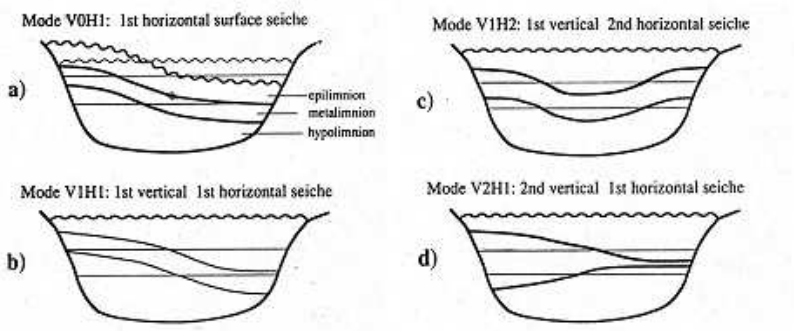

Figure 1.9.: Schematic view of various seiche modes in a closed basin with three homogenous layers.

Depending on the strength of the wind, the size and shape of the lake, the depth and strength of the stratification, the long waves degenerate into a spectrum of waves. The period of these waves ranges from days, as it is typical of long waves whose scale is determined by the size of the basin, to minutes (buoyancy frequency) for the free waves (Imberger, 1999). The nature of the high-frequency free waves may vary and consists of solitary waves, non-linear dispersive waves or bores; most of the energy in the waves is found in the vertical mode one, but modes two and three are also quite frequently observed (Antenucci and Imberger, 2001).

The time-frequency analysis suggests a kind of universal spectrum of internals waves,

which is characterized by peaks at low frequencies (representing discrete Kelvin, Poincaré or seiche modes), followed by a central band of frequencies and by energy peaks just below the buoyancy frequency representing solitary waves or waves induced directly by shear instabilities (Munnich, 1992).

In the long period, waves display predominantly the structure of the first vertical mode; hence, also the hypolimnion water may experience seiche motion across the bottom boundary. This generates turbulence and forms a benthic boundary layer in the hypolimnion which may attains the thickness of several meters.

1.4. Mixing

Transport and mixing phenomena are among the most important processes in natural systems (Imboden and Wuest, 1995). Water movements are vital components of the lake system and their effects on changes in the distribution of temperature, dissolved gases, nutrients and other chemical parameters must be considered. Turbulent movement in water creates mixing (Martin and McCutcheon, 1999). The extent of mixing in lakes and reservoirs depends on the balance between the forces supplying energy for mixing the system and the forces opposing to the process. The mixing patterns are the result of both external forces and internal properties of the system such as the morphometry of the water body or the stability of the water column. Mixing is generally highly variable in both time and space due to the temporal and spatial structure of the principal driving forces (Imboden and Wuest, 1995). The dominant mixing forces providing energy are meteorological conditions (like convective cooling, thermal energy due to radiation, sensible heat transfer, evaporation, and mechanical energy due to wind), inflows (streams, underground and surface overland runoff) and outflows.

1.4.1. Mixing in the Surface Layer

The surface mixed layer of a lake extends from the surface to a depth whereby the effect of surface winds and surface heat fluxes are no longer felt. The major external sources providing energy for turbulent mixing in the surface layer of a lake are wind stress and surface buoyancy flux (Imberger and Hamblin, 1982).

Wind acting on the surface of the lake introduces both momentum and turbulent kinetic energy to the lake by creating a shear stress, which can be expressed by:

$$\tau_0 = C_D \, \rho_a \, W_{10}^2, \tag{1.16}$$

where ρ is the density of water, C_D is the drag coefficient and W_{10} is the wind speed at a height of $10m$ above ground level. Wind stress is generally responsible for the majority of the mixing in the uppermost part of the surface layer.

Turbulent kinetic energy sources are transported and redistributed through the surface layer predominantly by large scale or secondary motions such as turbulent diffusion and Langmuir circulation. The small amount of energy which remains after dissipation increases the potential energy of the system, leading to deepening of the mixed layer (Imberger and Hamblin, 1982).

Shear instability may develop, arising from the velocity differences between the surface mixed layer and the metalimnion. This may give rise to interfacial waves known as Kelvin Helmholtz instabilities or billows. Billows can weaken the density gradient at the base of the mixed layer, which implies that this gradient can be eroded more easily (Imberger and Patterson, 1990).

1.4.2. Mixing in the Metalimnion

The metalimnion is a region of rapid density change, which separates the epilimnion from the hypolimnion. Buoyancy effects damp the turbulent fluxes of momentum, heat and mass; the velocity within this layer changes from the high values of the surface-layer to the very small intensity in the hypolimnion. Hence, in this region high shear occurs, with intense production of turbulent kinetic energy (Imberger and Hamblin, 1982).

The barrier formed by the density gradient in the metalimnion tends to suppress the transfer of turbulence through the metalimnion to the hypolimnion. If the wind stress persists for relatively long period of time, the vertical distribution of momentum may lead to a general motion in the direction of the wind. This causes the metalimnion to be displaced downward at the downwind end and hence, upwelling may occur at the upwind end of the lake (Wetzel, 1983). When the wind ceases, the tilted interface begins to oscillate and the solid barrier of the lake boundary reflects internal waves. The consequent superposition of the original and reflected waves results in internal seiches (standing internal waves) (Imboden and Wuest, 1995).

1.4.3. Mixing in the Hypolimnion

The horizontal and vertical mixing of mass, heat, and momentum in the weakly stratified hypolimnion are important processes affecting the health of lakes (Imberger, 1999). External forcing such as storms, inflows, outflows, or differential heat inputs cause the ex-

citation of large scale motions, whose scale is determined by the size of the basin. In turn, smaller-scale internal waves propagate into the main basin, leading to the establishment of a relatively continuous broad spectrum of internal waves. These waves rapidly fill the lake basin; however, their motions normally do not create enough shear for mixing processes to occur. Mixing, however, may occur if lake boundary or internal interactions lead to isolated sporadic turbulent patches (Imberger and Hamblin, 1982).

Internal waves produce horizontal currents in the hypolimnion that can lead to turbulent mixing provided they are strong enough to overcome the density stratification. If the Richardson number Ri is greater than a critical value nearly equal to 0.25, turbulence and mixing are fairly weak and consequently the energy dissipation is low: under these conditions the persistence of internal waves can reach periods of weeks. Instead, for $Ri < 0.25$ an increased disturbance arises within streamlines and turnover occurs between adjacent layers. In this case the energy dissipation is large and the decay of the internal wave is quite fast (Imboden and Wuest, 1995).

1.4.4. Diapycnal diffusivity coefficient

To estimate the vertical diffusion through vertical column, limnologists usually consider a single eddy diffusivity coefficient.

A variety of formulations and methods have been proposed in the literature, from the simplest approaches according to which the coefficient is assumed to be in dependent of external forcing to more refined approaches, where the effect several parameters which may affect the diffusion is taken into account (Martin and McCutcheon, 1999).

At first, vertical turbulent diffusivity coefficient has been related to the mean lake depth in the following form:

$$\epsilon_z = 0.142 m^{1/2} s^{-1} \cdot D^{1.5}, \tag{1.17}$$

where D is the total mean depth. The above formulation has been improved to account for the effect of wind, which is, usually, considered as the only source of mixing energy in eddy-diffusivity approaches. Since wind energy depends not only on the wind speed but also on the fetch, the eddy diffusivity coefficient has been related to the surface area A_s:

$$\epsilon_z = 3.3 \cdot 10^{-9} m s^{-1} \sqrt{A_s}. \tag{1.18}$$

Furthermore, another parameterization has been proposed which includes both effects:

$$\epsilon_z = \frac{D}{34} u^*, \tag{1.19}$$

where u^* is the shear velocity (wind friction or bottom shear velocity).

The above methods provide neutral eddy diffusivity coefficients $\epsilon_{z,0}$, that is the coefficient governing mixing phenomena in unstratified basins (Henderson-Sellers, 1976).

Given the pronounced effect of stratification on damping vertical mixing, in stratified conditions a correction is required which takes into account that density is changing on depth. Generally this correction is expressed as:

$$\epsilon_z = \epsilon_{z,0} \cdot f(St), \tag{1.20}$$

where $f(St)$ is a dimensionless stability function which varies from 0 (when the stratification is strong and vertical mixing is inhibited) to 1 (when the effect of stratification can be neglected).

Stability is expressed usually as a function of Richardson number in the following form:

$$f(St) = (1 + a\ Ri)^b\,, \tag{1.21}$$

where $a = 10 \div 30$ and $b = -0.5$ (Henderson-Sellers, 1976).

2. Velocity field induced in lakes

Circulations in lakes are induced by wind, differential heat fluxes, and inflows and outflows dynamics.

Generally, the wind is the main cause of motion in lakes, while inflows and outflows only induce local effects, except for man-made reservoir where the water direction may be quite constant and flow intensity is strongly connected to regulation. The differential heating and cooling may yield a flushing motion only on lakes with littoral long mild slopes.

The stratification strongly influences the circulation and can affect the dynamics over a depth of several meters; in some cases it may happen that the deeper interior remains completely parted from upper layers and does not show traces of any motion.

2.1. Wind-induced steady circulation

The equations of motion can be written as:

$$\frac{du}{dt} = -\frac{1}{\rho}\left(\frac{\partial p}{\partial x} + \frac{\partial F_{xx}}{\partial x} + \frac{\partial F_{yx}}{\partial y} + \frac{\partial F_{zx}}{\partial z}\right) + fv, \tag{2.1}$$

$$\frac{dv}{dt} = -\frac{1}{\rho}\left(\frac{\partial p}{\partial y} + \frac{\partial F_{xy}}{\partial x} + \frac{\partial F_{yy}}{\partial y} + \frac{\partial F_{zy}}{\partial z}\right) - fu, \tag{2.2}$$

$$\frac{dw}{dt} = -\frac{1}{\rho}\left(\frac{\partial p}{\partial z} + \frac{\partial F_{xz}}{\partial x} + \frac{\partial F_{yz}}{\partial y} + \frac{\partial F_{zz}}{\partial z}\right) + g, \tag{2.3}$$

where (x,y,z) denote an orthogonal coordinate system with z vertical coordinate, (u,v,w) denote the corresponding three-dimensional velocity components, t is the time, p is pressure, ρ is density, Fij are the "ij" components of the stress tensor, g is gravity and the last term in (2.1) and (2.2) accounts for the effect of Coriolis forces.

Furthermore, continuity equation reads:

$$\frac{\partial u}{\partial x} + \frac{\partial v}{\partial y} + \frac{\partial w}{\partial z} = 0. \tag{2.4}$$

The simple case of steady state can be analyzed assuming that inertial terms and Coriolis forces are negligible, and the pressure is hydrostatic (Hutter, 1984). In two dimensions, hence considering the lake as a rectangular box in the xz plane section (see figure 2.1), the previous system reduces to:

$$\frac{\partial p}{\partial x} + \frac{\partial F_{xz}}{\partial z} = 0, \tag{2.5}$$

$$-\frac{1}{\rho}\frac{\partial p}{\partial z} + g = 0, \tag{2.6}$$

$$\frac{\partial u}{\partial x} + \frac{\partial w}{\partial z} = 0, \tag{2.7}$$

Moreover, the vertical shear can be expressed in terms of the eddy viscosity ν:

$$F = F_{xz} = -\rho\nu\frac{\partial u}{\partial z}. \tag{2.8}$$

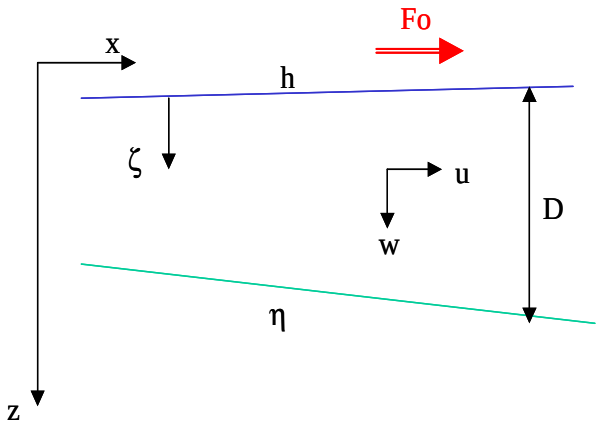

Figure 2.1.: Scheme of a semplified lake subjected to wind.

The above equations can be rewritten in terms of a boundary fitted coordinate system x-ζ, where:

$$\zeta = \frac{z-h}{D}, \tag{2.9}$$

h e D denote the elevation and flow depth, respectively.

The following momentum equations are obtained:

$$\frac{\partial p}{\partial x} - \left[\frac{\partial h}{\partial x} + \zeta\frac{\partial D}{\partial x}\right]\frac{1}{D}\frac{\partial p}{\partial \zeta} + \frac{1}{D}\frac{\partial F}{\partial \zeta} = 0, \tag{2.10}$$

$$\frac{1}{D}\frac{\partial p}{\partial \zeta} = \rho g. \tag{2.11}$$

Integrating equation (2.11) and substituting into (2.10) we obtain:

$$-\rho g\frac{\partial h}{\partial x} + \frac{\partial p_h}{\partial x} + \frac{1}{D}\frac{\partial F}{\partial \zeta} = 0, \tag{2.12}$$

where p_h denotes the external pressure at the lake surface.

Introducing the piezometric level $H = h - \frac{p_h}{\rho g}$ and integrating from $\zeta = 0$ to a generic position ζ, we obtain (Hutter, 1984):

$$F = \rho g D\frac{\partial H}{\partial x}\zeta + F_h, \tag{2.13}$$

where $F_h = F(\zeta = 0)$. Since $F = -\rho\upsilon\frac{1}{D}\frac{\partial u}{\partial \zeta}$ in stretched coordinates, it is possible to obtain a simple solution for the velocity field in x direction, when the eddy viscosity is assumed to be constant, which takes the following form:

$$u = -\frac{gD^2}{2\nu}\frac{\partial H}{\partial x}\zeta^2 - D\frac{F_h}{\rho\nu}\zeta + C_1. \tag{2.14}$$

The constant C_1 can be determined imposing the continuity equation integrated over the water column and assuming that the vertical velocity w vanishes at the boundaries:

$$\int_0^1 \left\{D\frac{\partial u}{\partial x} - \left[\frac{\partial h}{\partial x} + \zeta\frac{\partial D}{\partial x}\right]\frac{\partial u}{\partial \zeta} + \frac{\partial w}{\partial \zeta}\right\} d\zeta = \frac{\partial}{\partial x}\left[D\int_0^1 u\, d\zeta\right] = 0. \tag{2.15}$$

Since the basin is closed, the depth averaged value of velocity must vanish:

$$D\int_0^1 u\, d\zeta = \text{ cost} = 0. \tag{2.16}$$

Hence, using (2.16), from (2.14) we obtain

$$u = -\frac{gD^2}{6\nu}\frac{\partial H}{\partial x}\left(3\zeta^2 - 1\right) - D\frac{F_h}{2\rho\nu}\left(2\zeta - 1\right). \tag{2.17}$$

Denoting by F_η the value of F at the bottom of each layer considered, $F(\zeta = 1) = F_\eta$, the pressure gradient can be expressed through (2.13) in the following form:

$$\frac{\partial H}{\partial x} = \frac{F_\eta - F_h}{\rho g D}. \tag{2.18}$$

2.1.1. The case of homogenous lake

If we assume that the density of the water column is homogeneous and we impose the no slip condition $u = 0$ at the bottom, the piezometric slope can be expressed by:

$$\frac{\partial H}{\partial x} = -\frac{3}{2}\frac{F_0}{\rho g D}, \tag{2.19}$$

where F_0 is the wind stress, while the velocity profile takes the following form (Hutter, 1984):

$$u = D\frac{F_0}{4\rho\nu}\left(1-\zeta\right)\left(1-3\zeta\right). \tag{2.20}$$

From (2.20) appears that there are two points along the water column where the horizontal velocity vanishes namely for $\zeta = 1$, that is at the bottom and for $\zeta = \frac{1}{3}$, where the velocity changes sign. Moreover, the displacement of the free surface h depends on the wind stress F_0, the length along which the wind can affect the lake and the total depth.

Notice that, neglecting the spatial variations of the atmospheric pressure p_h, $\frac{\partial h}{\partial x}$ and $\frac{\partial H}{\partial x}$ coincide.

2.1.2. The case of non-homogenous lake

In the generic case of more layers, the shear at the boundary can be imposed as following:

$$F_\eta = F(1) = \rho k\left[u(1) - u_s\right], \tag{2.21}$$

where u_s is the slip velocity and k is a constant.

Therefore, the case of slip $F(1) = \rho k u(1)$ is included when u_s is negligible small, while the no-slip condition $u(1) = 0$ is recovered as k$\longrightarrow \infty$.

Defining $M = \frac{\nu}{kD}$, $U = \frac{D}{\nu\rho}$, $S = \frac{u_s}{U}$, the shear can be rewritten as:

$$F_\eta = \frac{1}{M}\left(\frac{u_\eta}{U} - S\right). \tag{2.22}$$

Hence we can write:

$$F_\eta = -\varphi F_h, \tag{2.23}$$

where $\varphi = \frac{1+6S}{2(1+3M)}$. Furthermore, the velocity profile, the pressure gradient and the shear profile can be given the following form:

$$u = \frac{U}{4\left(1+3M\right)}\left[\left(1-\zeta\right)\left(1-3\zeta\right)+2M\left(3\zeta^2-6\zeta+2\right)+2S\left(3\zeta^2-1\right)\right], \tag{2.24}$$

$$\frac{\partial H}{\partial x} = \frac{F_\eta - F_h}{\rho g D} = -\left(1+\varphi\right)\frac{F_h}{\rho g D}, \tag{2.25}$$

$$F = -\rho\upsilon\frac{1}{D}\frac{\partial u}{\partial \zeta} = \frac{F_h}{4\left(1+3M\right)}\left[4-6\zeta+12M\left(1-\zeta\right)-12S\zeta\right]. \tag{2.26}$$

Two layers case

In this case at the surface we have the conditions $F_{h1} = F_0$ and $\frac{\partial p_{h1}}{\partial x} = 0$, hence:

$$\frac{\partial H_1}{\partial x} = \frac{\partial h_1}{\partial x} = -\left(1+\varphi\right)\frac{F_{h1}}{\rho_1 g D_1}, \tag{2.27}$$

while at the interface between the two layers the conditions $\eta_1 = h_2$, $u_{s_1} = u_{h_2}$ and $F_{\eta 1} = F_{h2} = -\varphi F_{h1}$ hold. Since $p_{h2} = p_{h1} + D_1\rho_1 g$, the pressure gradient can be expressed in the following form:

$$\frac{\partial H_2}{\partial x} = \frac{\partial h_2}{\partial x} - \frac{1}{\rho g}\frac{\partial p_{h2}}{\partial x} = -\frac{3}{2}\frac{F_{h2}}{\rho_2 g D_2}, \tag{2.28}$$

while at the bottom, where $\eta_2 = \eta_0$, the shear is $F_{\eta 2} = -\frac{F_{h2}}{2}$.

The slope of the free surface is:

$$\frac{\partial h_1}{\partial x} = \frac{\partial H_1}{\partial x} = -\left(1+\varphi_1\right)\frac{F_0}{\rho_1 g D_1}, \tag{2.29}$$

while the slope of interface reads:

$$\frac{\partial h_2}{\partial x} = -\left(1+\varphi_1+\frac{3}{2}\frac{D_1}{D_2}\varphi_1\right)\frac{F_0}{\rho_1 g D_1 \Delta}, \tag{2.30}$$

where $s_1 = -\left[8\left(1+3M_1\right)\frac{\rho_2}{\rho_1}\frac{D_1}{D_2}+6\right]^{-1}$, $M_1 = \frac{\nu}{kD_1}$, $\varphi_1 = \frac{1+6S_1}{2(1+3M_1)}$ and $\Delta = \frac{\rho_1}{\rho_2-\rho_1}$.

It is worth noting that Δ is roughly equal to 1000; consequently, the interface is much more tilted than the free surface to counterbalance the pressure gradient (Hutter, 1984). This equilibrium implies the occurrence of horizontal motion which exhibits the following structure.

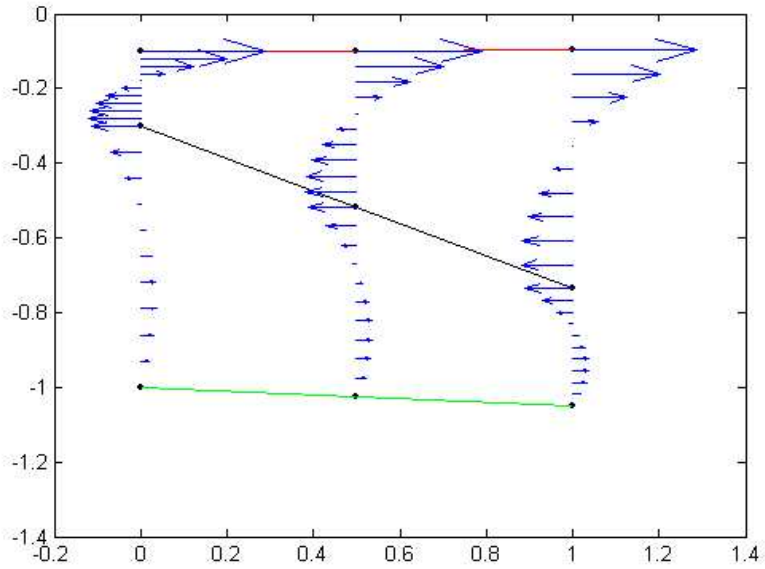

Figure 2.2.: Theoretical velocity profiles and isopycnal surfaces for a two-layered lake subject to a constant wind.

The velocities in the superficial layers are much higher than in the bottom layer; the inversion always occurs near the value of $\zeta = \frac{1}{3}$.

When the surface wind stress increases, the isopycnal surface rises at the upwind end and deepens at the downwind end. This phenomenon is called upwelling. (Imberger and Patterson, 1990). Typically, the isopycnals display a certain degree of disturbance some hours later the wind event. The response is complicated by several factors such as the unsteady nature of the wind, the deepening of the surface layer and by any pre-existing background circulation and internal wave field (Horn et al., 2001), but in general the following behaviour is observed: the wind stress applied on the water surface of a lake initiates a tilting motion of the surface which in turn causes downwelling at the downwind end and upwelling at the upwind end. At first, the underlying water moves in the same direction as the wind. The tilting of the water surface continues until the applied wind force is balanced by the pressure force.

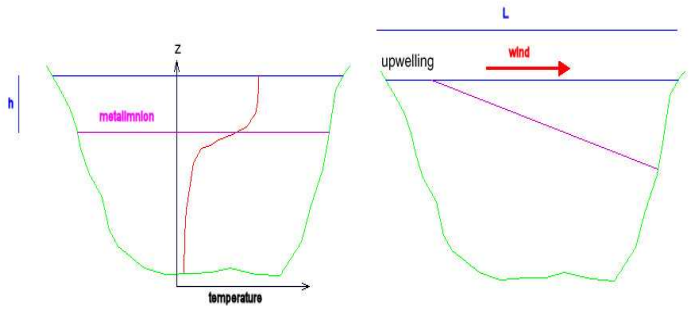

Figure 2.3.: Upwelling of metalimnetic water of a two-layered lake.

Upwelling of metalinetic water

The Wedderburn number W is a non-dimensional parameter determining the response of the surface layer to an impulsive wind stress introduced for a two-layer scheme (Thompson and Imberger, 1980). It can be defined as the ratio of the surface layer Richardson number to the aspect ratio (L/D), where L is the length of the lake in the direction of the wind and D is the mean depth (Horn et al., 2001); hence it represents the ratio of the baroclinic restoring force at the point of upwelling (e.g. the pressure gradient resulting from the slope of the interface or thermocline) to the wind disturbance force at the surface:

$$W = \frac{Ri}{L/D} = \frac{g^* h^2}{u_*^2 L} \tag{2.31}$$

where L is the fetch length of the lake, g^* is the modified gravity acceleration and h is the depth of the diurnal thermocline.

For $W >> 1$, tilting of the isotherms due to the applied wind stress is small and horizontal variations are negligible because of strong stratification, light winds and slow deepening of the mixed layer (which means that Richardson Number Ri is small). For $W << 1$, internal shear production and complete mixing occur (Imberger and Patterson, 1990).

The analysis of the n-layers case, with wind stress varying arbitrarily in time, shows that when W is small, the mode 2 is excited. This leads to a large shear across the base of the surface layer, with an associated strong tilt of the interface between the first and the second layer, while the second interface remains essentially horizontal (Monismith, 1985). However, when the density differences between the two interfaces are of the same order of magnitude and the depths of the top and bottom layer are comparable, the response is

strongly influenced both by the first mode and by the second mode, with a comparable tilt of the two interfacies and the occurrence of larger velocity in the bottom layer.

A mode 2 response concentrates the shear and induces turbulence in the upper surface layer, while the lower layer remains nearly stationary with horizontal interface, whereas a mode 1 introduces motion and turbulence within the entire water column, tilting the isopycnals both in the metalimnion and in the hypolimnion (Cacciatori, 2000).

Upwelling of hypolinetic water

As the wind stress increases, W decreases and the amplitude of the mode 1 response increases, causing the metalimnion to tilt, which induces upwelling not only from the metalimnion but also from the hypolimnion. In this case it is not the Wedderburn number that controls the mode 1 response, but the Lake number L_N. In fact, while the upwelling response of the epilimnion is determined by the magnitude of W, the upwelling response of the metalimnion depends on the magnitude of L_N. When W is small but L_N is large, only the surface layers respond to wind stress, while when W and L_N are both small, the lake as a whole responds and vertical mixing greatly increases throughout the lake.

The Lake Number is a dimensionless parameter representing the ratio of the moment of the stabilizing force of gravity (due to stratification) to the moment of the destabilizing forces (fundamentally the wind, since inflow, outflow or artificial mixing devices can be neglected) calculated with respect to the centre of volume of the lake:

$$L_N = \frac{S_t \, (D - h_t)}{u_*^2 \; A_s^{3/2} \; (D - h_v)}, \tag{2.32}$$

where D is the maximum depth of the water body, h_t is the seasonal thermocline depth from the bottom of the lake, h_v is height to the centre of volume of the lake, A_s is the lake surface area, and S_t is the Schmidt stability index 1.14.

The Schmidt stability index, in case of a 2 layers lake schematization, can be expressed by:

$$S_t = \frac{1}{2} \frac{g^*}{\rho_0} \left(\rho_2 - \rho_1\right) \left[\frac{A_1 h_1 A_2 h_2 \left(h_1 + h_2\right)}{A_1 h_1 + A_2 h_2}\right], \tag{2.33}$$

where symbols are illustrated in figure 2.5.

The Lake number is a quantitative index of the dynamic stability of the water column and is an indicator of deep mixing in lakes. It describes the vertical exchange between the surface and deep waters in stratified lakes. This is a central issue in the understanding of the

fluxes of particles and nutrients, which in turn play an important role in the eutrophication of these water bodies.

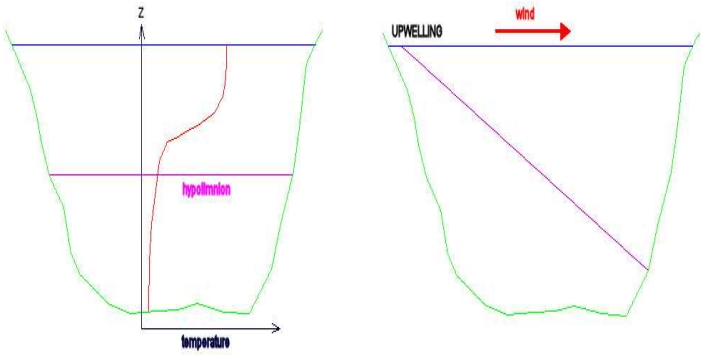

Figure 2.4.: Upwelling of hypolimnetic water of a two-layered lake scheme.

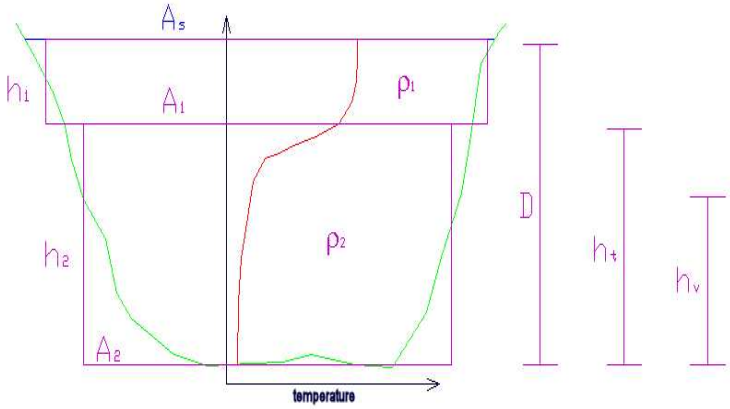

Figure 2.5.: Two-layered lake scheme.

When L_N is equal to one, the wind is able to force the seasonal thermocline to reach the surface at the upwind end of the lake. When $L_N >> 1$, stratification is strong and dominates the forces introduced by surface wind energy: deep upwelling does not occur and seiching within the thermocline is expected to be minimal, as the turbulent mixing in the metalimnion and hypolimnion. For $L_N << 1$, the stratification is weak with respect to the wind induced forces and the deep, often nutrient rich, waters from the hypolimnion can reach the surface layer during the wind event (Imberger, 1999). In this case strong seiching is expected in the thermocline and a large amount of turbulent mixing is expected

to occur in the metalimnion and hypolimnion (Cacciatori, 2000).

2.2. Circulation induced by differential heat fluxes

Differential cooling and heating are very important in shallow lakes, wetlands, riverine embayments or sidearms of large lakes and may be responsible for flushing of littoral water. The turbulent convection induced by these mechanisms leads to very effective lateral transport between the littoral water and the surface water in the center of the lake (Sturman et al., 1999). This effective lateral mixing is highly time-dependent as well as strongly related to the diurnal thermal cycle in a lake. It represents one of the most significant, physical processes occurring in a lake, from an ecological point of view.

Differential cooling has mainly two causes: the different distribution of back radiation flux (heat loss from the surface) over different depths of water and the heat differences due to variations of wind speed across different parts of the stretch of water (Cacciatori, 2000).

Differential cooling phenomenon occurs at night when the influx of solar radiation falls below the rate of flux emitted from the surface. Generally, the shallow littoral water cools to a temperature lower than that in the deeper interior and this heat loss increases the littoral water density until it becomes heavier than the underlying water. This generates instability within the water column, causing the cooler water to fall by gravitational adjustment down the sloping boundary, until it reaches a depth of approximate isopycnity, normally at a depth corresponding to the metalimnion or more rarely within the hypolimnion (Cacciatori, 2000). As a result, water from the centre deeper part of the lake replaces littoral water falling down the slopes. This process continues as long as a net heat imbalance exists between the surface water and the atmosphere, resulting in the replacement of water in the littoral zone with the surface water from the interior of the lake (Cacciatori, 2000).

The ratio between T_f, flushing time, and T_c, time over which night cooling occurs, provides a measure on whether the convective mechanism and flushing of the littoral zone may occur (Imberger, 2001):

$$C = \frac{T_f}{T_c} = \frac{V D^{1/3}}{w_* \; L^{7/3} T \; \tan\phi}. \tag{2.34}$$

Notice that the convective velocity is given by $w_* = \left(\frac{\alpha H g D}{c_p \rho_0}\right)^{1/3}$, V, D and L are the volume, the maximum depth and the lengthscale (radius) of the lake, respectively, ϕ is the mean embankment angle and T is night time duration, expressed in seconds (typically 43200 s). The convective velocity can be calculated when the heat loss H is known.

Table 2.1.: Parameters for convective velocity calculation.

thermal expansion $\alpha =$	$2.57{\cdot}10^{-4\circ}C^{-1}$
gravitational acceleration $g =$	9.8 m/s^2
heat capacity $c_p =$	4179 J Kg$^{-1\circ}C^{-1}$

When the value of this ratio is less than 1, the littoral zone will experience flushing during night time cooling, while if it rises above 1, then the effect of night time cooling is negligible and water exchange is small (Imberger, 2001).

2.3. Motion related to inflows and outflows

The prediction of inflows and outlows mixing and currents in lakes is a complex three-dimensional problem, complicated by the variations in the morphometry of the lake as well as by the interactions between flows and entrainment processes. However a large set of simplified methods provide suitable approximations which can be used to understand mixing and transport phenomena (Martin and McCutcheon, 1999).

Inflows

In general hypolimnetic water is replenished by a cold water river inflow that reaches the bottom through underflows.

The most critical aspect is to determine whether the inflow will separate and proceed into the lake as an underflow. River inflows always possess large values of the Reynolds number, such that whether an inflow underflows is determined solely by the ratio of the inertia to internal buoyancy forces, the internal Froude number (Imberger, 1999).

If flow separation occurs as the river enters the lake, the internal Froude number Fr of an underflow is constant:

$$Fr = \frac{u}{\sqrt{g^* D}} = \frac{Q}{\sqrt{g^* D A}} = \text{constant}, \tag{2.35}$$

where Q is the inflow rate, g^* is the modified gravity due to the difference in density between the inflowing water and the surface water, R is the hydraulic radius of the underflow and A is the inflowing area. Suppose B represents the width of the lake: then $R = A/B$ and $A = DB$. Hence the depth h_i at which the inflow becomes an under- or overflow can be defined as follows:

$$\frac{h_i}{H} = \left(\frac{Q}{\sqrt{g^*} D^{\frac{3}{2}} B} \right) Fr_c, \tag{2.36}$$

where Fr_c is the critical value of the plunge point (Imberger, 1999).

Outflows

In natural lakes the outflows take place via a river removing surface water. Because of stratification, water particles preferentially move horizontally rather than vertically. For small outflows or strong stratification, the water is removed via a thin layer adjacent to the level of the outflow. This is called "selective withdrawal".

The majority of selective withdrawal layers are governed by a simple inertia-buoyancy force balance. According to (Imberger, 1999), whether the outflow is drawn selectively from the depth corresponding to the outflow level (the surface for a river leaving a natural lake) or from a range of depths spanning the depth of the lake, depends on whether the Froude number

$$Fr = \frac{Q}{\sqrt{g^*} D^{\frac{5}{2}}} \tag{2.37}$$

is greater or lower than 1.

Part II.

Experimental section

In this part we present the case study of lake Tovel. The investigation is aimed at characterizing the thermodynamic and hydrodynamic behaviour of the lake through the collection of data and the subsequent analysis of experimental results.

The experimental observations started in summer 2002. The first field campaign has been mainly devoted to the set-up, test and calibration of instruments. A second campaign has been performed in 2003, from late spring to the beginning of fall, during which temperature and velocity data have been collected through extensive measurements.

In the experiments advanced instruments have been used like precision temperature minilogger probes, acoustic velocity profiler and current meter. Further measurements have been carried out using drifters equipped by GPS systems.

3. Lake Tovel

3.1. Introduction

The lakes are one of the most important features in the landscape of Trentino, which is located in Northern/Eastern part of Italy within the alpine region. In the area there are 297 lakes covering a total area of 35 square kilometers out of the 6212 of the provincial territory. They show an interesting altimetric distribution: in the valley areas from the 65 metres altitude of Garda lake up to 1200 metres, the largest lakes are located: 40 lakes correspond to a lacustrian area of nearly 32 square kilometres. Furthermore, there are no lakes between 1200 and 1500 metres. Above this height up to a maximum altitude of 3200 metres, there are 257 very small alpine lakes, with a modest total area of nearly 3 square kilometres. This distribution is due to the origin of Trentino lakes. Nearly all of them were created by glacial excavation, Pleistocene at low altitudes, historical or current at higher altitudes. The morphology of high altitude lakes is typically ”cirque” alpine: a fairly regular shape tending to be circular. They last for a predictable length of time as they are supplied with light, calm surface water free of any solid content. This is why they are so transparent.

One of these lakes, the Tovel lake, is also well-known as the "red lake" due to the red color of its water.

The reddening of Tovel's lake was considered one of the most suggestive natural happening that Trentino Alto Adige region could offer to their tourists in summertime: the case of Tovel lake was the only reddening known to happen yearly. The reddening was produced by a seaweed called ”Glenodinium Sanguineum”, studied and catalogued by Marchesoni. The process suddenly ceased after the last reddering observed in summer 1964. Since then many studies have been developed and hypothesis have been formulated to explain the extinction of the phenomena. However, the problem is still unresolved.

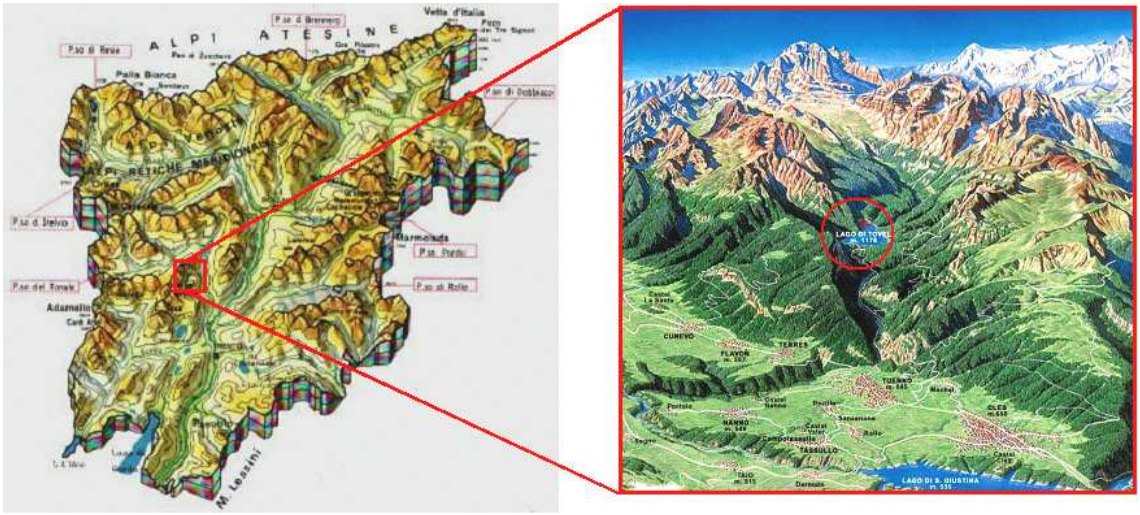

Figure 3.1.: Overview on Tovel valley.

3.2. Tovel lake: reddening and environmental context

Tovel lake is a temperate, meromictic (with dimictic mixolimnion), oligotrophic mountain lake, characterized by marked water level fluctuations.

The lake is located in Tovel Valley within the northern Brenta Group (see figure 3.1): the northern section of the Brenta Group is the wildest part of the Brenta chain, famous dolomites; because of his natural beauty, this zone is a reserve, the Adamello-Brenta Natural Park.

The valley covers a zone from the confluence of S. Emerenziana stream and Tresenga stream to the dolomitic "pass Grosté". The length of valley is about 17 km and the lake is located nearly in the middle, at 1178 m altitude.

The valley extends from North East to South West and is limited, in the Western part, by an Alpine ridge, whose height reaches 3000 m, in the eastern part by another smaller ridge, while in northern direction the valley is open.

The valley is characterized by the presence of several landslides, even of recent formation, that pile up the old glacial moraines and originate the phenomenon of "marocche".

The origin of lake Tovel is due to the the deposition of collapsed material ("marocche") in the centre of valley drill that made possible the formation of this stretch of water.

The lake has an outlet, Tresenga river, that disappears close to Glare village under the collapsed material and reappears further downstream, creating some small pools which are used to feed two irrigation plants.

Figure 3.2.: The river Tresenga outlet from lake Tovel.

The tributaries of Tovel lake are the Rislà creek, that originates a water fall just before the entrance to the lake and the Tresenga creek, that originates in a gorge at 1900m altitude, disappears and feeds the lake by underground inflows. The catchment area is slightly less than 40 km^2 and the mean elevation of the surrounding rocky crests is about 2500 m a.m.s.l.

The available bathimetry indicates isobathes up to 38 meter depth with respect to the zero level, which corresponds to a lake volume of $7.367.600\,m^3$, an area of $382.000\,m^2$ and coast line extension of 3480 m. It is important to note that the pool is characterised by marked water level fluctuations $(3 \div 5\,m)$. The lake displays a length of roughly 1 km in the NE-SW direction and a width of about 750 m in the NW-SE direction.

The mean depth is

$$z_m = \frac{V}{A} = 19.28\,m,$$

while the characteristic lenght of lake is

$$L = \sqrt{2A} = 874\,m.$$

In figure 3.3 the volume and the area of Tovel lake are plotted as functions of the water level.

A better characterization of the lake is obtained dividing the lake in three parts. In fact Tovel lake shows a nearly triangular planimetric shape, while the bathimetric map

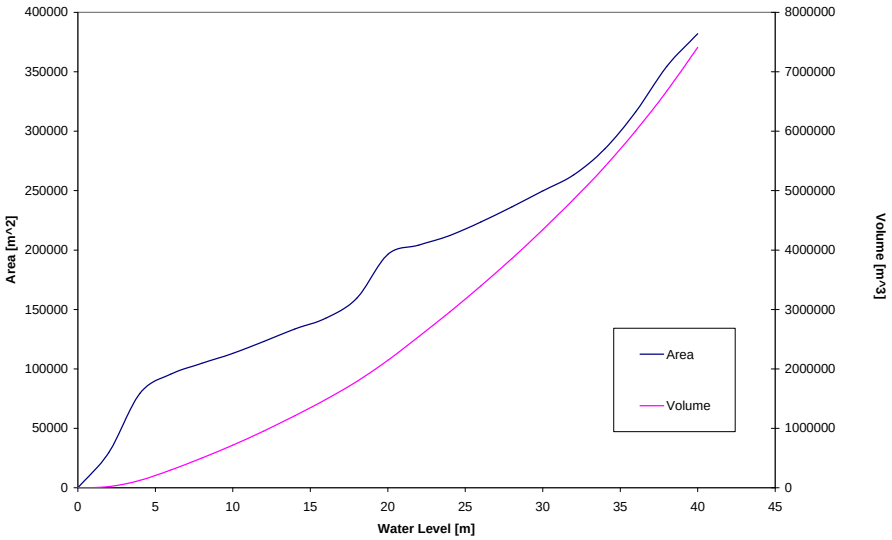

Figure 3.3.: Volume and area of Lake Tovel versus depth.

Table 3.1.: Characteristics of the main sub-zones of lake Tovel.

	$z_{max}\,[m]$	$z_{mean}\,[m]$	area $[m^2]$	volume $[m^3]$
Centre Lake	39	19.46	382000	7411473
Joining Gulf	9	4.19	43320	181843
Red Bay	4.5	2.64	24200	64018

allows one to distinguish 3 different behaviours of sounding: the SO gulf (called "red bay") presents a maximum depth smaller than 6 m and mild shores, while in the bulk part (NE part) the lake reaches a depth of 39 m and shores are steep. An intermediate zone joins the SO gulf to the bulk lake through a first part nearly flat and a second with a sharp slope, as shown in figure 3.4.

The shallowness of the red bay seemed to play a basic role in the reddening phenomenon.

In fact, the process was related to the concurrence of two distinct effects: the first one, biological, due to the nature of algae and the second one, geophysical, caused by the breeze.

The dinoflagellate "Glenodinium sanguineum Marchesoni" is a polymorphous alga: during the summer, besides the chlorophyll in biosynthesis, it produces and accumulates carotenoids (astaxanthin-like compound), turning red.

The last process, called carotenogenesis, requires warm temperature (more than 14°) and

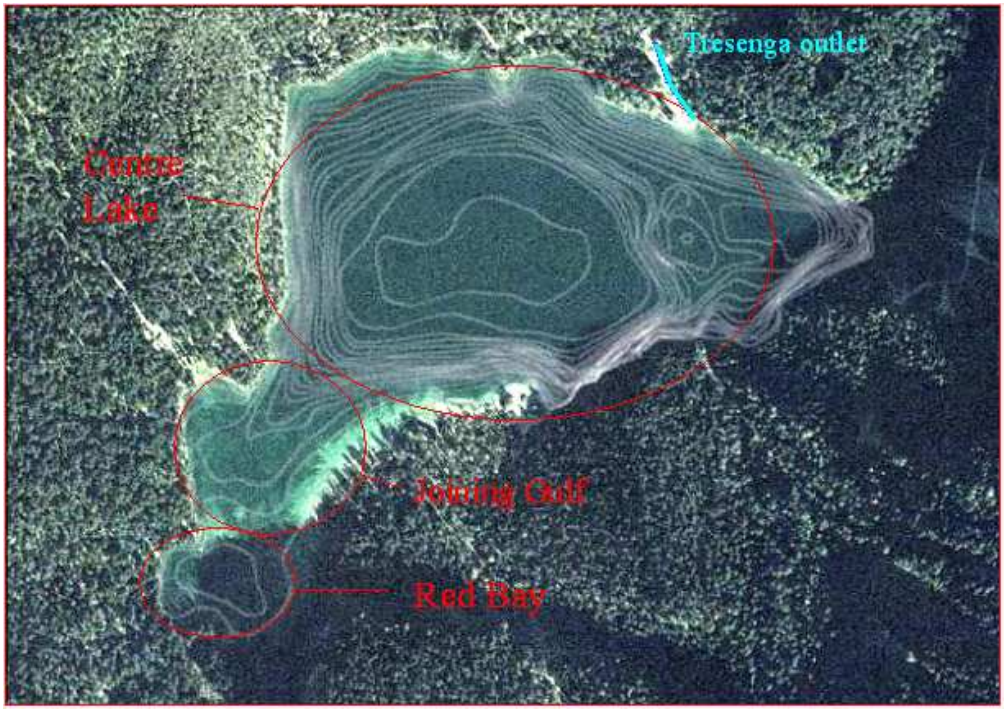

Figure 3.4.: The three sub-zones of Lake Tovel.

strong direct light for enough time. These conditions, typical of summer days, favour two further important phenomena: the phototropism, which results in the upward movement of red algae caused by density difference and the passive transport driven by valley breeze.

The bay was the ideal zone for this process to occur: the shallow water could receive more nutrients from underground spring, warm up more because of small thermal inertia and hold all Glenodinium driven by surface currents.

As pointed out before this spectacular and regular "summer reddening" ceased suddenly in 1964 and never occurred after that year, except for some light cases, called "prereddening".

Several hypotheses have been proposed to explain it. The most reliable are:

1. the increasing of humidity of air (and therefore of cloudiness) in Tovel Valley due to strong sprinkler irrigation for apple intensive cultivation and the S.Giustina dam construction.

2. the vanished supply of phosforous and other organic material linked to the sewerage system construction and the vanishing of alpine grazing

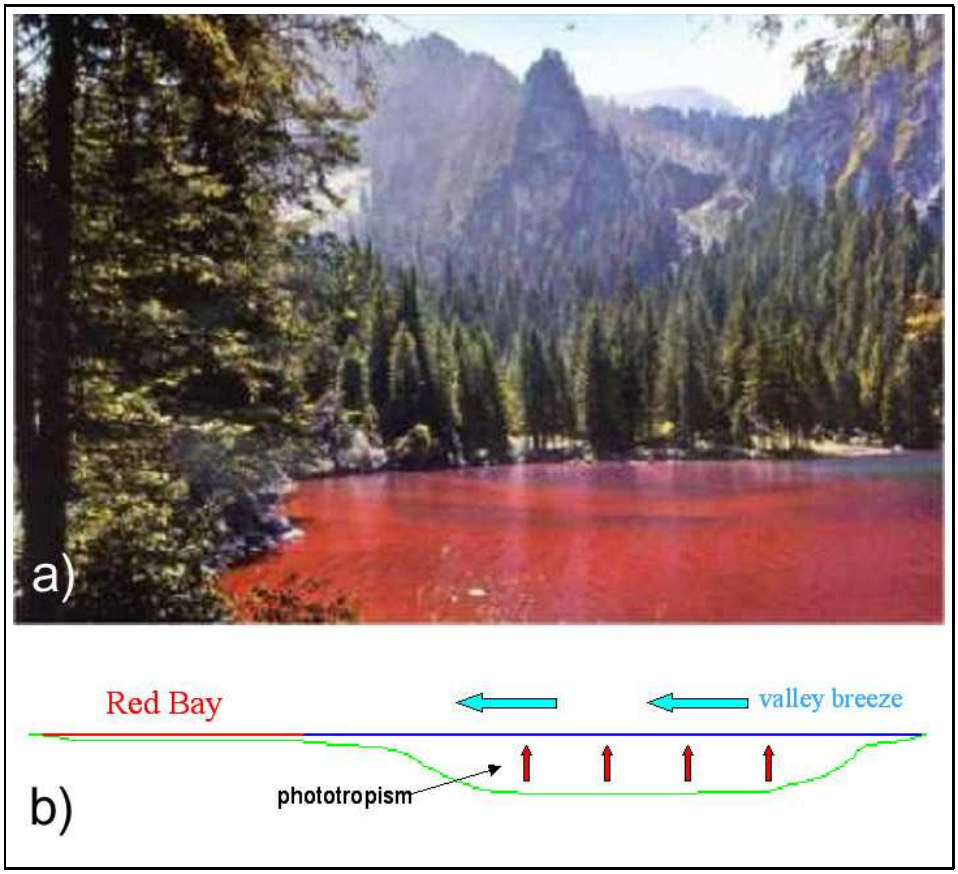

Figure 3.5.: a) the Red Bay in a picture of 1963; b) the possible mechanism for the glenodinium accumulation in the bay.

3. the illegal opening of the outlet in 1963 to get more water for irrigation from the lake.

In 2000 a special project, called SALTO, has been funded by the Province of Trento with the aim of understanding the reason for the disappearance of the reddering phenomenon.

4. External forcings

4.1. Meteorological data

The survey of weather conditions has basic significance for the analysis of the dominant dynamics in a lake; to this end, in the centre of lake, a new floating platform has been located where all data acquisition instruments have been mounted.

The weather station was placed on a floating platform (2.5 x 2.5 m^2) operated by the "Istituto Agrario di San Michele all'Adige" and moored in the middle of the lake where the maximum depth occurs. The instruments were as follows: a low-inertia cup anemometer on the top of a thin mast at 2.3 m above the lake surface; a shielded and naturally ventilated thermohygrometer fixed on the same mast, 1.7 m above the lake surface; a net radiometer (covering the range 0.3-60 μm) placed nearly 60 cm off the platform and close to the water surface (approx. 30 cm). The sampling time was set to 30 s for all the sensors, storing the average values as well as standard deviations every 10 min (De Franceschi et al., 2003).

Along the shore, southward in red bay, there was another weather station belonging to "Istituto Agrario di S.Michele", that have been collecting meteorological data every hour since long time.

This station stores, in addition to data collected by anemometer, thermohygrometer and radiometer as the previous station, information about pressure, precipitation and water level.

4.1.1. Weather conditions

The field measurements has been carried on for the entire year 2003 and provide important information about valley dynamics.

The year 2003 has been characterized by a considerable drought: in fact the precipitation data collected during the summer show values typically lower than those observed in previous summer: measured values are constantly lower than 20 mm/d while in the same period of 2002 values greater than 50 mm/d have been measured. This fact has strongly influenced the water level and the water supplies of lake.

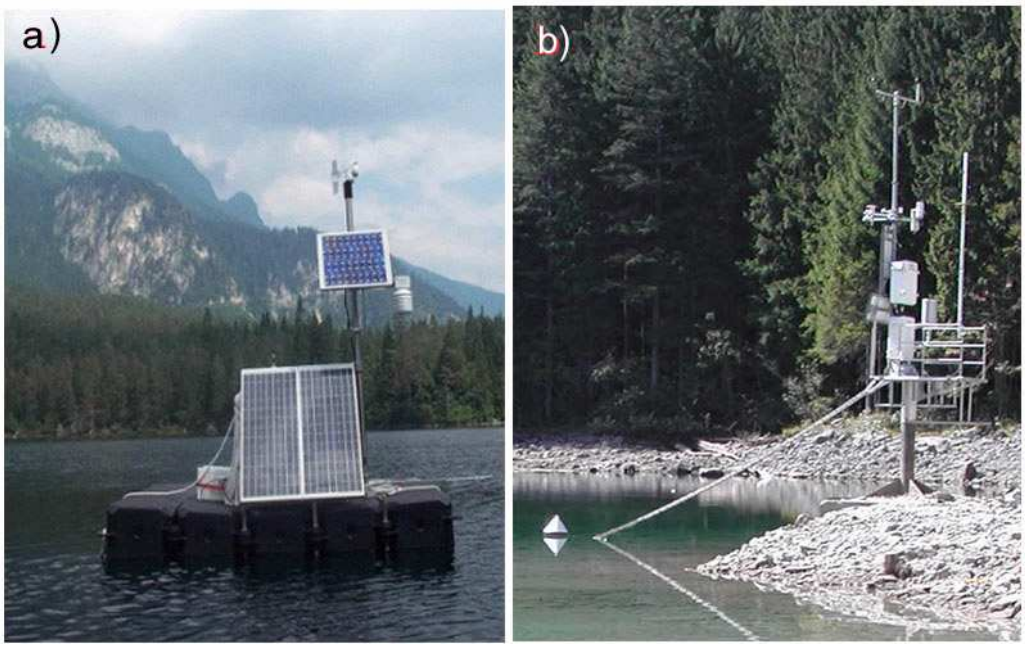

Figure 4.1.: Weather stations: a) University of Trento, located in Centre Lake b) Institute of S.Michele, located in Red Bay.

The graph reported in figure 4.2 shows the absence of significant precipitations for relatively long periods, like for instance in August and in September; furthermore, when it rained, the precipitations have reached values roughly equal to half the value observed in the previous year. It is worth noticing that the micro-climate of Tovel valleyin summer is characterized by the convective formation of clouds that often provides short precipitations.

In summer 2003 high temperature values have been measured during stable weather conditions in the first two weeks of August, when air temperature reached nearly $30°C$, with average values nearly equal to $20°C$. The prevailing perturbations were represented by local rains caused by uplift of moist air masses close to the mountain crests, as it is typical of summer season, but they were also characterized by some frontal systems which induced relatively strong precipitations in the periods 17, 21 July and 18, 24, 29-31 August (De Franceschi et al., 2003).

Moreover, the good weather influences the temperature in lake and over the free surface: in this case the processes of cooling and heating (which drive the breezes) are increased. The net radiation data display incoming energy fluxes ranging between 700 to 800 Wm^2 and outgoing fluxes nearly equal to $-40W/m^2$. In rainy and cloudy days the radiation was considerably reduced.

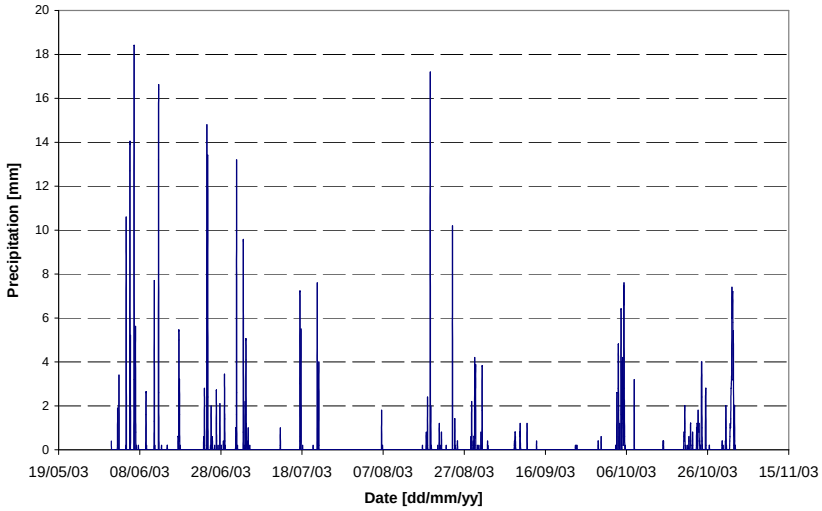

Figure 4.2.: Precipitations on Lake Tovel in Summer 2003.

Excluding the rainy days, it is easy to distinguish an undisturbed diurnal cycle of net radiation and up- and down-valley winds as the response of the valley atmosphere to the solar radiation input.

The average net radiation evaluated through the data corresponding to sunny days displays a higher maximum value, at noon, with respect to that obtained from the whole dataset (nearly $250 W m^{-2}$ of difference). In fact, the frequent formation of convective clouds close to the lake reduces sufficiently the incoming radiation.

The incoming solar radiation occurs only in the window 08:00÷16:00 and shows a rapid roll-off in the afternoon. Both these effects are induced by the high mountain crests surrounding the lake. The temperature maximum occurs about two hours later than the radiation maximum, and the afternoon cooling phase displays a slow drop, which is associated to the heat flux slowly released by the water surface after sunset (De Franceschi et al., 2003).

The temperature data provided by both stations find a good agreement, with discrepancy lower than $0.5°C$. Night temperature is often lower in Red Bay with respect to other parts of the lake, while peak values are similar: a time lag is exhibited by the incoming radiation that first reaches the centre and than the Red Bay.

The values of relative humidity values display a similar behaviour: during the night saturation has been reached (though in Red Bay values equal to 100% are never found)

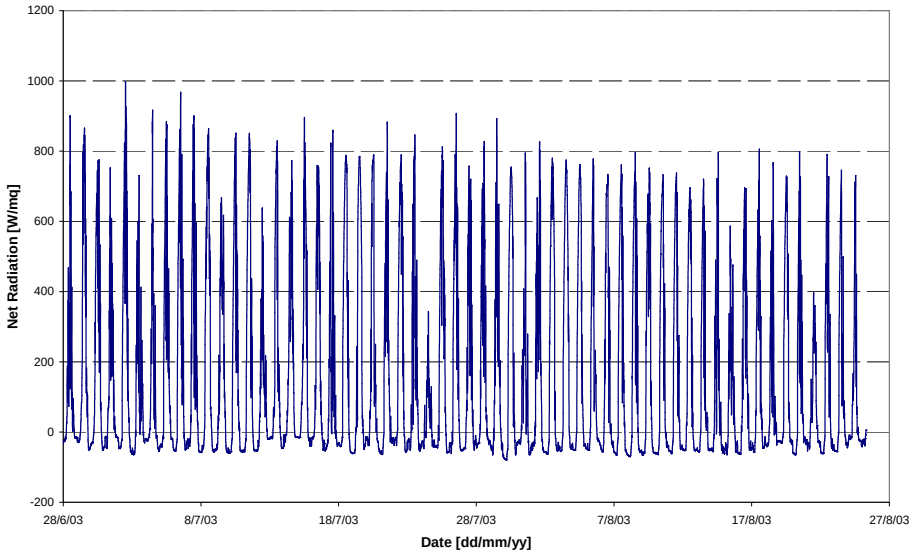

Figure 4.3.: Net Radiation Flux measured in centre lake.

while during the sunny period relative humidity decreases in both zones. Atmospheric pressure keeps nearly constant (888 mb) for all the period.

Typically, during the sunny periods (i.e. 27-31 July 2003), the wind speed during night time is quite high (up to 1 m/s) except around 07:00 when the net radiation becomes positive and the down-valley wind is strongly attenuated (figure 4.5 shows the wind speed and direction). The wind direction gradually turns to up-valley and the intensity steadily increases, reaching a maximum approximately around 14:00, a couple of hours after the net radiation maximum, in agreement with the air temperature time evolution measured in the weather station located in centre lake.

During the afternoon, in coincidence with the rapid roll-off of the net radiation around 15:00, we observe a quick change in wind direction such that a down-valley flow rapidly replaces the preceding up-valley wind. It's important to notice that these flows do not seem to affect significantly the air temperature over the lake, which continues to supply heat to the air above (De Franceschi et al., 2003).

In analysing a rainy period (i.e. the last week of August) we have found a similar behaviour, characterized by a different window of up-valley and down-valley breezes, because different temperatures have occurred in these days, but with the same alternation of the sunny periods (figure 4.6). The most important feature is the decrease of the wind intensity, that moves from the peak value of $2 \div 3\ m/s$ to $1.5\ m/s$: this occurs because

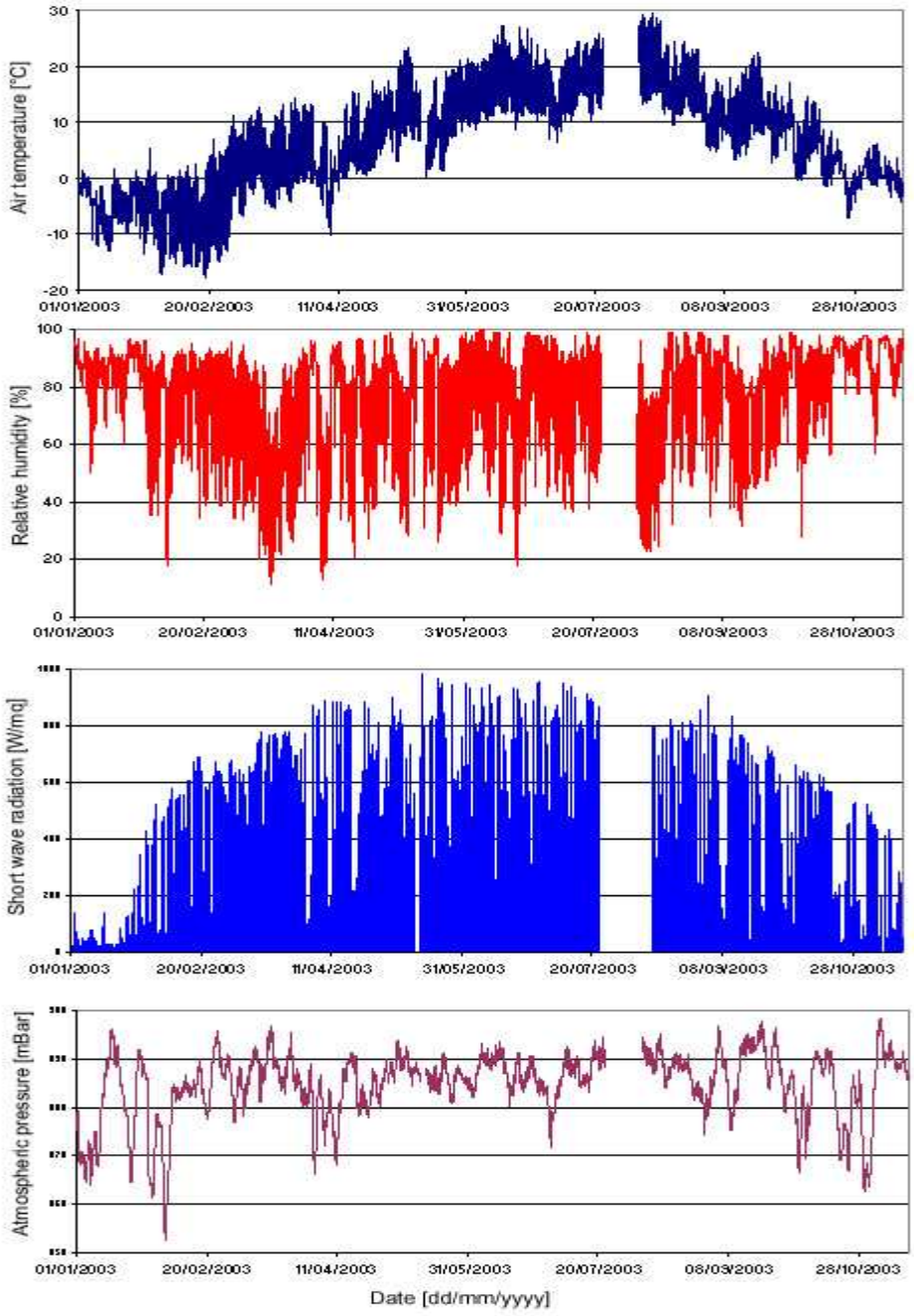

Figure 4.4.: General atmospheric data collected by weather station of "Istituto Agrario San Michele all'Adige" from January 1st to November 15th 2003.

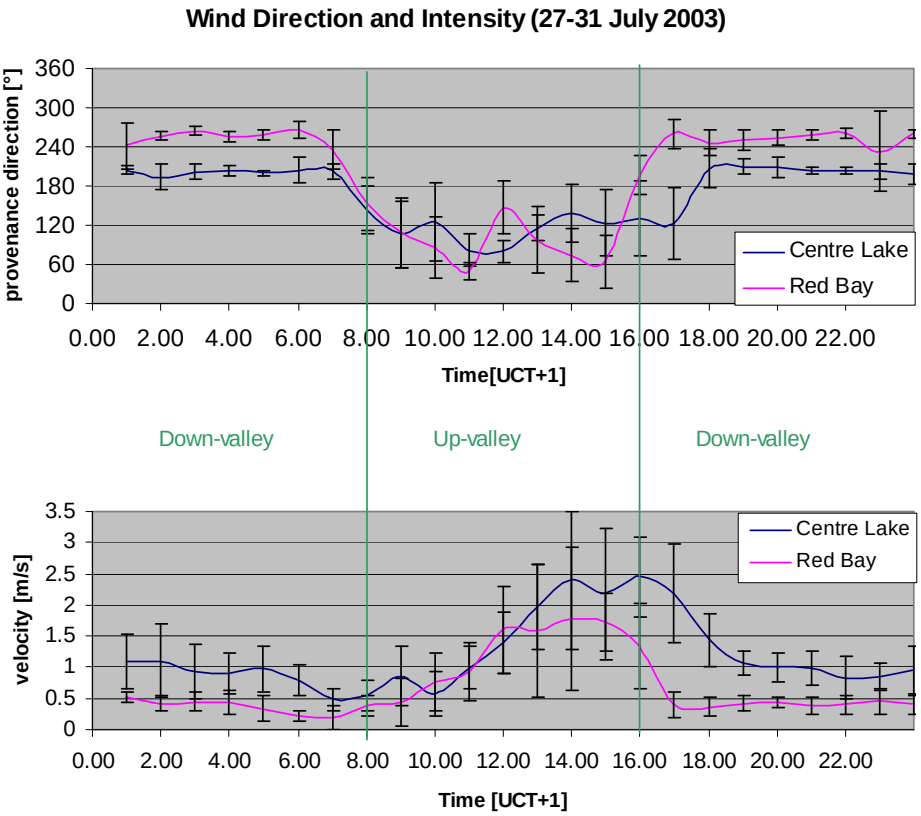

Figure 4.5.: Mean diurnal wind properties in summer sunny period. Thick line: mean values; bars: standard deviations.

the pressure gradient which is produced by the differential heating of mountain rocks and valley, is lower and draws smaller quantity of air from the bottom of the valley.

In Autumn, all these processes persist but display a very small intensity, such that the wind velocity doesn't change in moving down or up-valley, as shown in figure 4.7 which represents a sunny period in the middle of October 2003.

From these figures it may also be inferred that the wind flows in down-valley direction during the night and in up-valley direction during the day: in particular, the breeze pushes on until Red Bay as the solar radiation incomes. In any case wind speed is greater in centre lake with respect to the bay.

Moreover, looking at the steady differences between the profile of wind direction stored in the two weather stations a change of wind direction can be detected: the walls of the

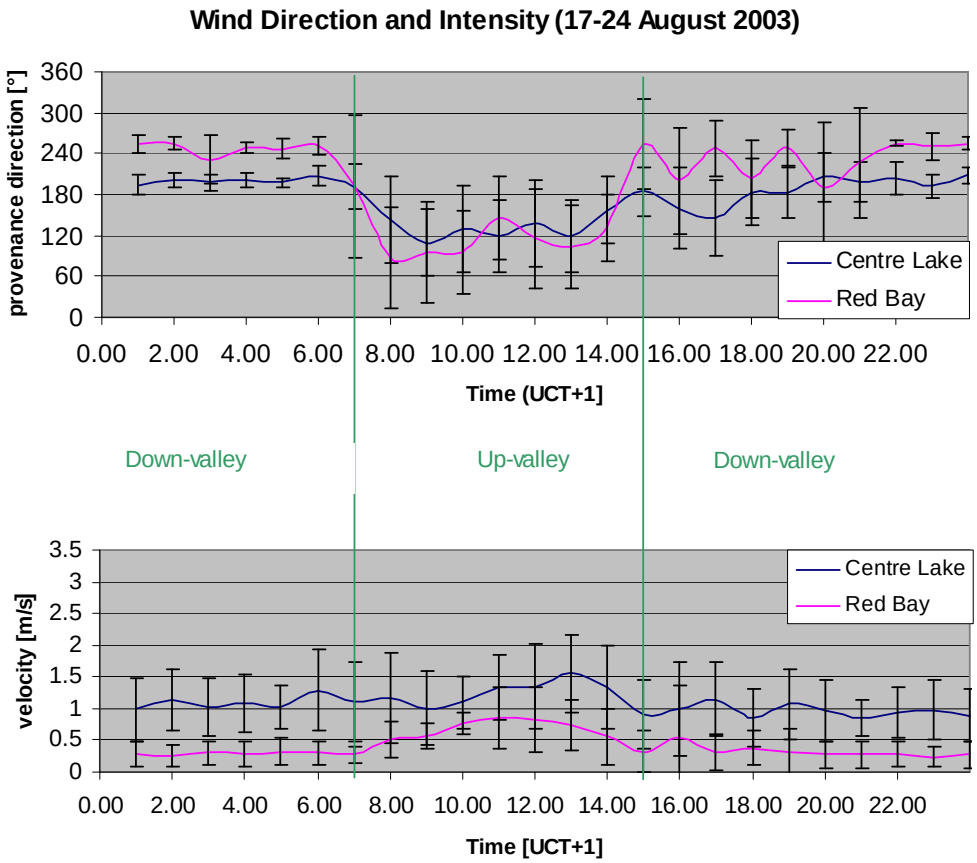

Figure 4.6.: Mean diurnal wind properties in summer rainy period. Thick line: mean values; bars: standard deviations.

valley drive the wind path such that the up-valley breeze moves from 120° measured in centre lake to 80° in Red Bay, while the down-valley breeze moves from 250° in Red Bay to 190° in the centre lake, as shown in the figure 4.8.

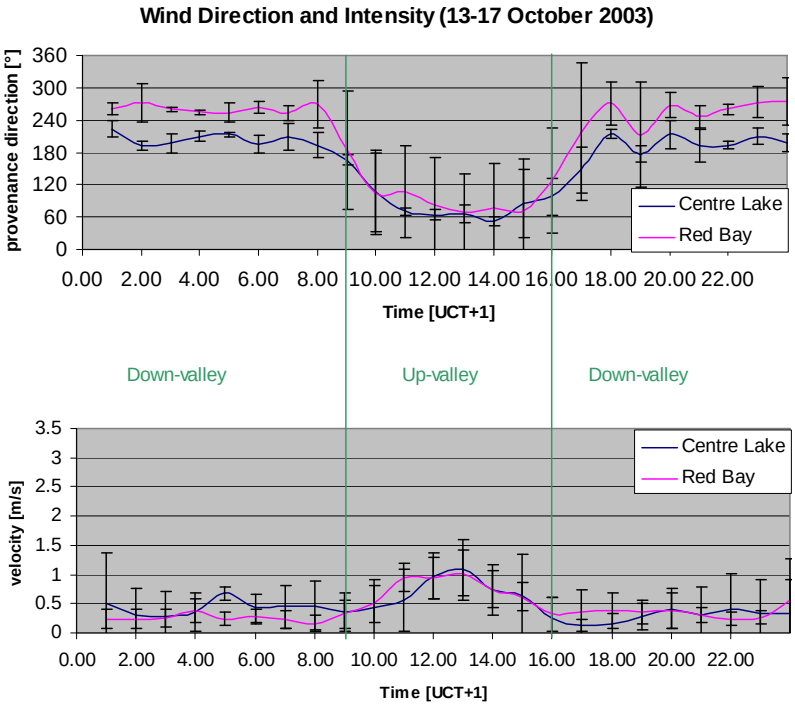

Figure 4.7.: Mean diurnal wind properties in autumnal sunny period. Thick line: mean values; bars: standard deviations.

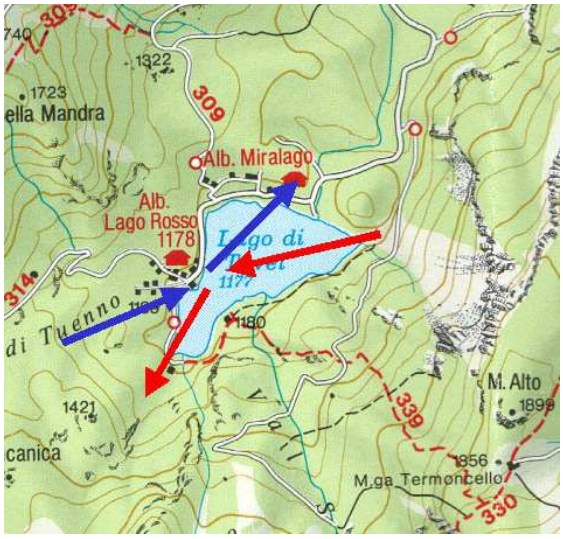

Figure 4.8.: Wind path deviation.

4.2. Inflows and outflows

The study of the dynamics of a lake can not leave out of consideration inflow and outflow contributions: one of most relevant problems in the case of Lake Tovel is to determine external flows in the pool. The lake has two superficial inflows, Tresenga and Rislà creeks, the latter reaches directly the stretch of water, while the former infiltrates in the ground and supply the lake by underground springs.

The outflow is the Tresenga river: it drains the surface water in the NE part of the lake and downgoes for several kilometers in Tovel Valley: the maximum discharges measured can achieve nearly 1 $m^3 s^{-1}$.

During the entire year 2003 (and since 2001) these two superficial inflows (Tresenga and Rislà creeks) and the outflow (Tresenga creek) have been monitored by "Museo di scienze Naturali di Trento".

In figure 4.9 the genearal behaviour of superficial flows is shown: it clearly displays that Rislà creek carries a contribution which is negligible in comparison with the Tresenga inflow. Moreover, the discharge from the outlet is much greater than inflows, until the first week of July, when all these measured flow rates turn to small values.

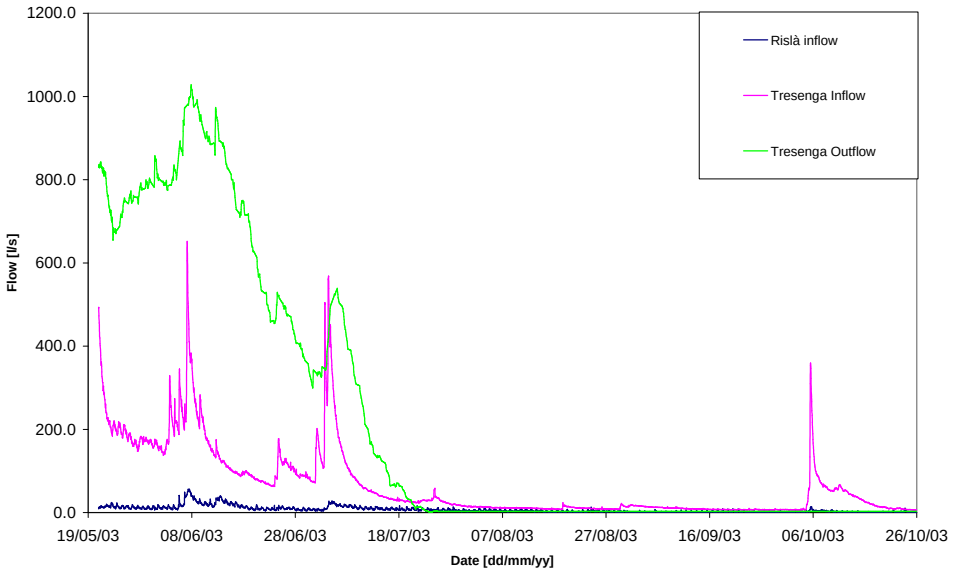

Figure 4.9.: Superficial flows in lake Tovel

In the summer 2003, due to a long period of dry weather, the level of the lake decreased from 1177.5 m a.m.s.l. to 1174.5 m a.m.s.l., with a mean lowering equal to $4 \div 5$ cm per

day from the first week of August to the first week of October. On the basis of free surface level data and through the continuity equation we have estimated that the non-measured groundwater seepages must be the greater flow contributions: in fact, even though measured superficial flows are nearly insignificant, the free surface level keeps decreasing until 6th October, when, due to a rainstorm, the Tresenga inflow supplies a large water volume; whence, the lake level remains stable until it increases again in November, due to another atmospheric perturbation.

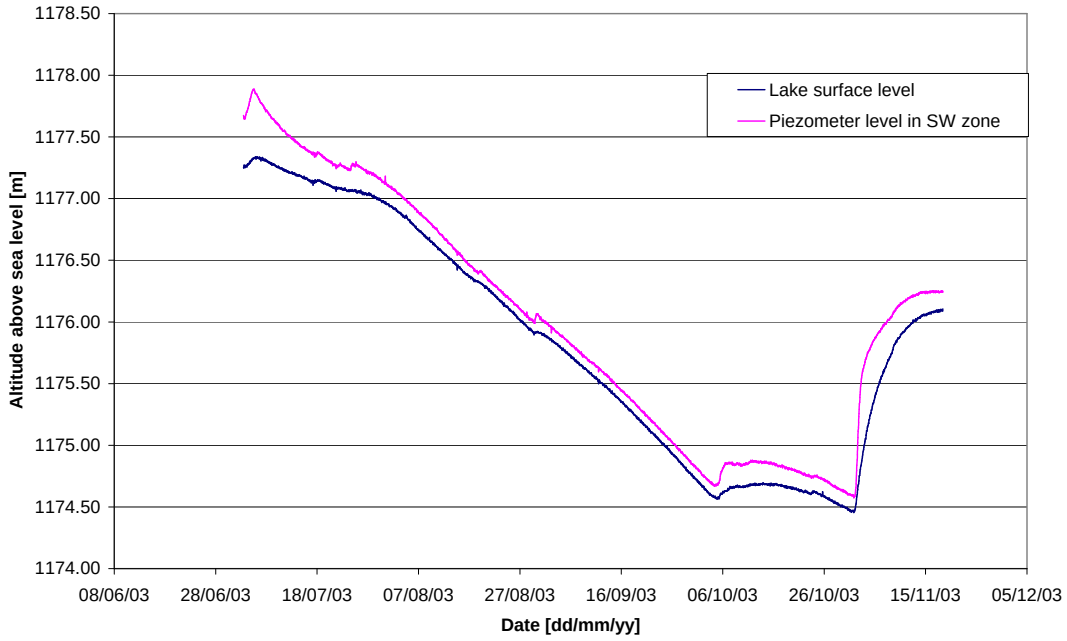

Figure 4.10.: Behaviour of lake level in Summer 2003

This fact has made possible the estimate of underground loss of volume: in fact, in some days the level of the piezometer located near the lake in part SW was nearly equal to the level of the free surface of the pool (lower than 10 cm). In this situation the infiltration entering in the lake can be estimated using the Darcy's law:

$$Q = -kA\frac{\partial h}{\partial x}, \tag{4.1}$$

were the hypothetical area A can vary from $1{\cdot}10^4$ to $4{\cdot}10^4 m^2$, the hydraulic conducibility is roughly $10^{-4} ms^{-1}$ and the distance between the two points of measurement is 300 m. We then obtain a rough estimate of $500 \div 1000$ m^3 per day of cold water infiltrating in the

South part of Lake Tovel.

However, the estimated supply can't explain the water level increase which occurred at the end of Summer.

From the other side, the nearly constant decrease of free surface means that a volume of $15000 \div 20000\ m^3$ outgoes from the lake as underground loss, which is probably located in the superficial part of the basin.Therefore the uncertainty about water supplies is strong.

In this way the same volume of water per day has been computed every time in underground inflow and outflow when the lake surface remains nearly constant, adding the volume required to satisfy the continuity equation: the superficial total flows plus the underground total flow must match the change of water volume due to the lake level fluctuation.

Finally, we note that from July until October, only the estimated underground supplies are responsible of the free surface movement, while all measured flows do not contribute to the volume balance (see figure 4.11).

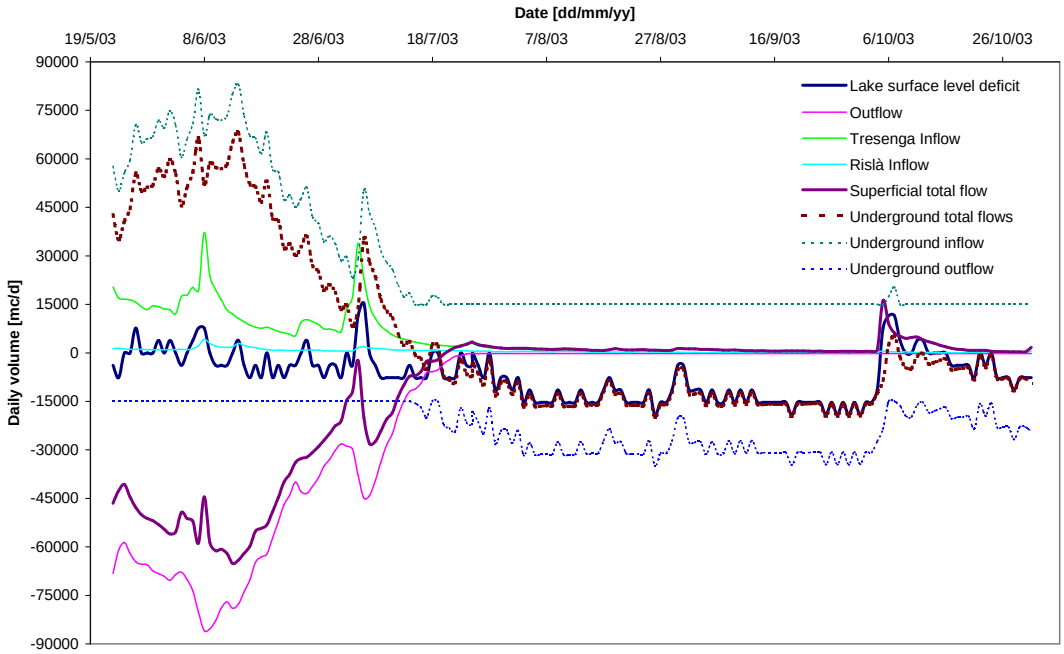

Figure 4.11.: Global behaviour of estimated (broken lines) and measured (solid lines) flows in lake Tovel.

5. Field instruments and field measurements

5.1. Introduction

Extensive field measurements have been realized during the year 2003 with the aim of collecting temperature and velocity data required for a detailed understanding of lake thermodynamics and hydrodynamics.

In late Winter and Spring 2 chains of temperature sensors have been positioned in the lake, even under the frozen surface, while during the Summer, 5 chains have been arranged along the main lake axis.

Moreover, we have collected additional temperature profiles using another probe to better characterize the temperature distribution in lake, with particular emphasis on the Red Bay.

Field velocity have been measured by an ADCP (Acoustic Doppler Current Profiler) profiler, that has been placed at several representative points to obtain velocity profile on water column, an ADV (Acoustic Doppler Velocimeter), which has been used to get current local measurements and a fluxmeter.

In order to get indication about the main circulations and horizontal dispersion the motion of 8 drifters with GPS systems have been monitored in continuos during August and September.

At the same time meteorological data have been collected using two weather stations, positioned nearly in the centre of lake and in the Red Bay.

A rubber dinghy has been specifically equipped to recover ropes and weights, to use notebook and serial interface and to fix special instruments as ADCP or ADV.

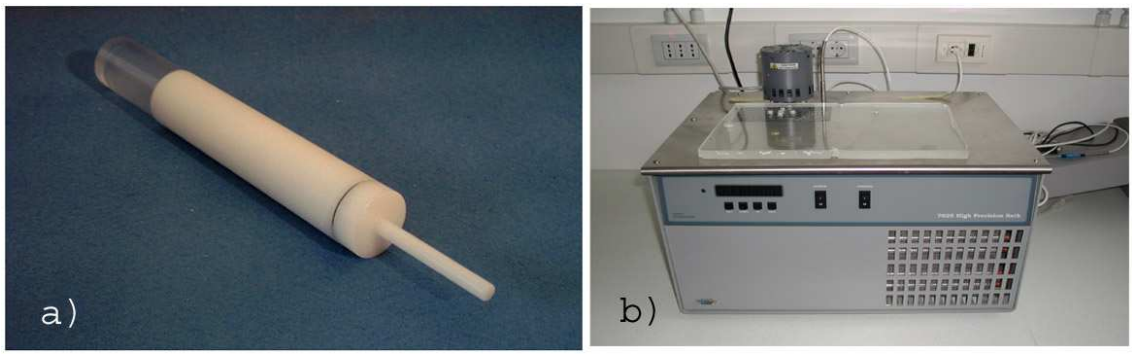

Figure 5.1.: a) Temperature probe; b) thermostated bath

5.2. Temperature data

5.2.1. Probes

In order to perform the temperature survey, 40 probes Handylog DK500 have been used: these sensors have a large application spectrum, from $-20°C$ to $+80°C$, and are equipped with internal loggers able to store a maximum of 64000 measurements.

The resolution of temperature sensors is very high: in fact we have calibrated all probes to get an accuracy of $\pm 0.05°C$.

The calibration has been carried out using a thermostated bath, with temperature controlled by a thermistor PT100. Measurements have been collected every minute and the stored data have been downloaded using Infralog software, connecting the probe to a notebook by a infra-red connection. To minimize download period we have modified the probe cap using material which is transparent to infra-red rays.

A portable probe with a lower precision has been also used during intensive field measurement to get temperature profiles on water column.

5.2.2. Chains

All probes have been arranged on ropes (see figure 5.2), positioned to different depths according to expected temperature profile. The criterion used to get as much comparability as possible was that of locating the same number of probes roughly at the same distance from surface in the first two meters depth, while arranging the remaining probes with a different spacing, depending of the total depth.

Chains have been arranged as follows:

Table 5.1.: Position of thermistors.

Chain	Zone	North coordinate	East coordinate	Depth	Number of probes
A	red bay	5124471	32649927	3.5	6
B	near gulf	5124582	32649976	5	5
C	joining slope	5124698	32650016	9.5	7
D	center lake	5124912	32650204	38	12
E	NE part	5125093	32650280	31	9

Table 5.2.: Depths of temperature sensors.

chain A	chain B	chain C	chain D	chain E
0.3 m	0.3 m	0.3 m	0.3 m (surface)	0.3 m(surface)
1.0 m	0.7 m	0.7 m	0.7 m	0.7 m
1.5 m	1.0 m	1.0 m	1.0 m	0.9 m
2.0 m	2.1 m	1.6 m	1.5 m	1.4 m
2.5 m	4.8 m	3.9 m	3.0 m	1.9 m
3.5 m		6.9 m	4.1 m	3.9 m
		8.9 m	5.7 m	10 m
			8.1 m	20 m
			11.4 m	31 m (bottom)
			18.4 m	
			28.4 m	
			38.4 m (bottom)	

We may notice that the depth was fluctuating during the measurement period; to ensure that all devices were located in the correct positions, we have realized a system to keep the rope subject to tension, mooring the ends by a buoy at the surface and by a weight at the bottom and putting another small weight and buoy at middle rope.

All chains have been positioned along the main lake axis: one chain in centre lake, one in N E part, one in the joining slope, one in the intermediate zone near the gulf and the last in Red Bay.

Since the main axis corresponds to the main wind direction, in this way it is possible to get informations about isopycnal interfaces displacements.

During the Winter season only 2 chains have been placed in the lake, namely chain A

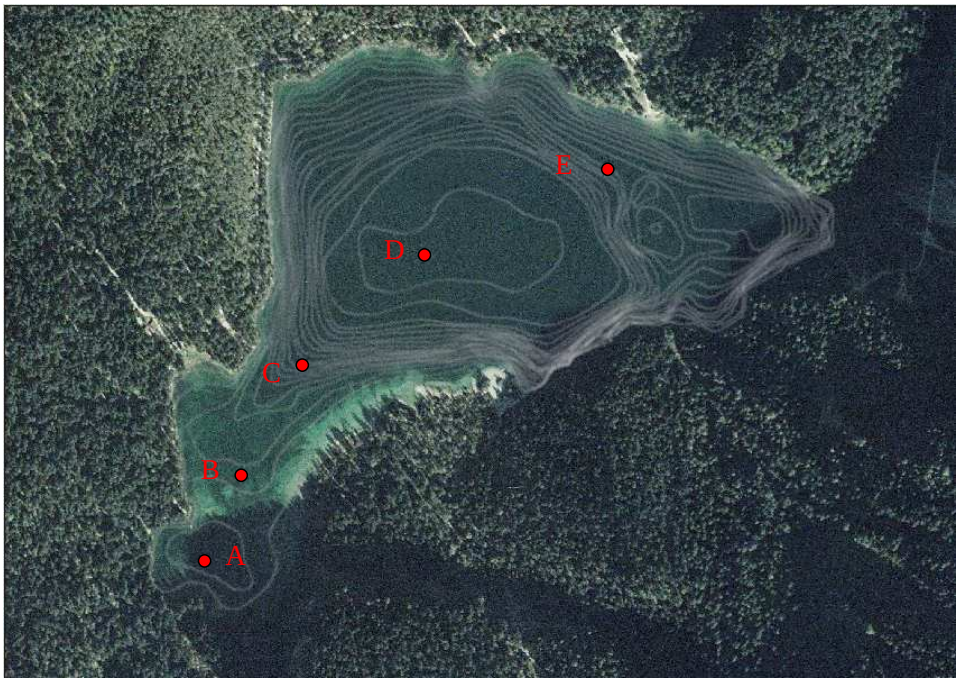

Figure 5.2.: Location of temperature sensor chains

and D, in order to obtain information on the thermodynamics in Red Bay and in centre lake.

Once recovered, 5 chains have been prepared for the summer measurements.

Chain A, located in "Red Bay", is formed by 6 sensors: it reached the bottom at the maximum depth of 3.7 m, at the beginning of the field measurement, and the minimum depth of 1.2 m in October. It has been measuring from June 9th until the end of the year and it has not been recovered yet due to freezing of the lake surface in December.

Chain B has been positioned near the gulf S W from July 25th and is formed by 5 sensors: it reached at the maximum depth of 5 m.

Chain C has been positioned on 9th June in the joining slope, where the depth is around 9 m and consisted of 7 probes: the first meter of water has been monitored as far chain B while below probes were placed with different spacing depending of chain length.

Chain D is representative of the bulk lake, since it has been positioned nearly in centre lake and reached the largest depth, about 38 m. Notice that in this case the distance between two consecutive probes increases downward up to the value of 10 m. This chain has been arranged with 12 probes and data have been recovered from 20th May to 15th November.

Chain E has been placed in the NE part of lake with 9 probes (6 probes in the superficial layer and the remaining probes with a vertical spacing of nearly 10 m) and registered temperature data from July 3rd to November 15th.

Missing data have been reconstructed every time that we have recovered chain for downloading operations or batteries replacement.

5.2.3. Summary of data collected

Data analysis has been performed paying specific attention to the following aspects: the seasonal trend of probes in each chain, the diurnal trend, the comparison between data from different chains and with temperature profiles collected by portable probe.

Chain A

The Red Bay, where chain A is located, is characterized by shallow water (lower than 4 m) and underground springs.

This zone, unlike the centre lake zone, which is deep and well sunny, doesn't receive for most of the morning direct solar radiation and very often, in the late afternoon, clouds cover the gulf.

A first look at the data suggests that stratification is strong, with a smooth temperature variation of few degrees associated with the alternation of sunny and cloudy periods.

Due to the relatively small depth we could expect strong variations related to weather conditions; however, near the bottom the stored data show a quite constant value of temperature in the last meter, nearly equal to $6°C$, due to the presence of a cold water flux supplied by underground springs.

In summer 2003 the highest temperature measured has been $22.96°C$ (August 4th at 16:20) at the surface.

The surface layer is very thin, roughly 1 meter deep, and superficial temperature changes from $12°C$ to $22°C$, while at the bottom we have found a temperature change ranging between $4.89 \div 7.31°C$.

From the data set three periods of strong heating are clearly distinguishable: the first occurs in June and ends with a rainy periods at the end of the month, the second starts on July 4th and ends on July 22nd with the occurrence of another atmospheric perturbation and the last period, in which the surface layer reaches the maximum temperature, lasts until August 14th when the weather conditions suddenly change.

For chain A it is very difficult to interpret the behaviour of sensors located at interme-

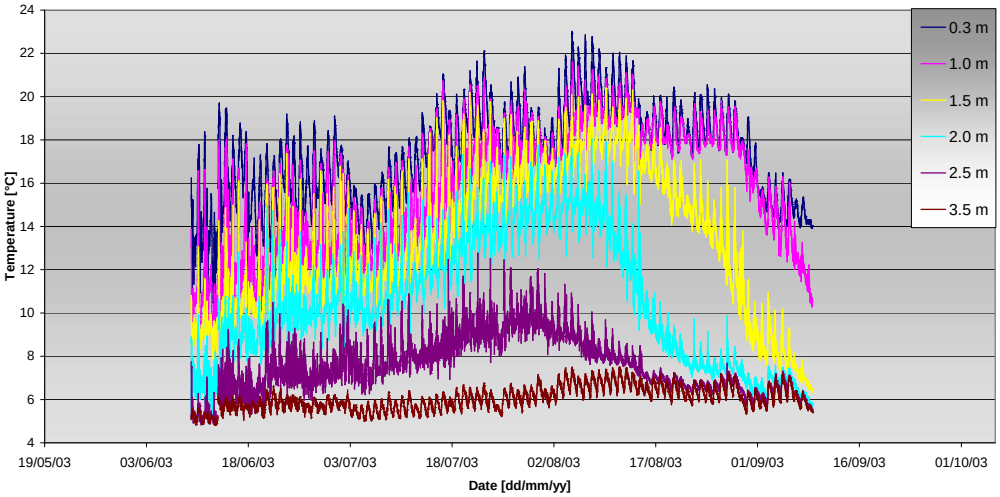

Figure 5.3.: Temperature data collected through chain A.

diate depth because the strong lowering of water level has driven some probe out of right arrangement (for instance, for probes placed at 1.5 m and 2 m, the temperature decrease which started on August 7th and finished in September is due to the downward shifting of sensors and not to a real cooling of water column).

Chain B

After July 25th a chain has been positioned in the near gulf SW, with the aim of better understanding the dynamics of exchange between the Red bay and the bulk of the lake. Probes were arranged at nearly similar depths in both chain A and B in order to perform a close comparison.

The behaviour of these data is clearly different from that in chain A: the most relevant difference is the greater value of temperature measured near the bottom where temperatures don't decrease below $11°C$, while in the first 2 meters close to the surface the temperature keeps steadily over $14°C$, which is the value corresponding to the homogenization of waters during September. The maximum value of temperature is $22.8°C$, measured on August 4th, at 19:30. Hence, data corroborate the assumption that the Red Bay has a peculiar behaviour which differs completely from the rest of the lake.

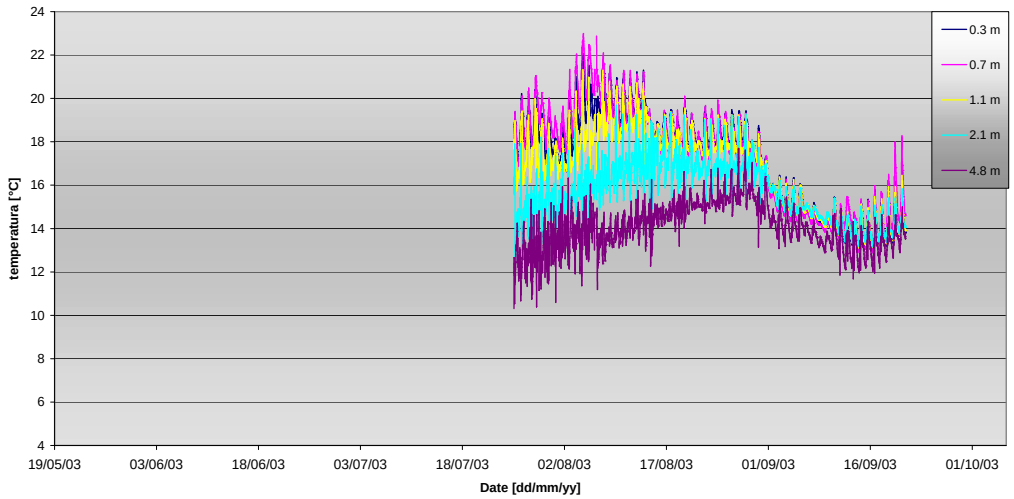

Figure 5.4.: Temperature data collected through chain B.

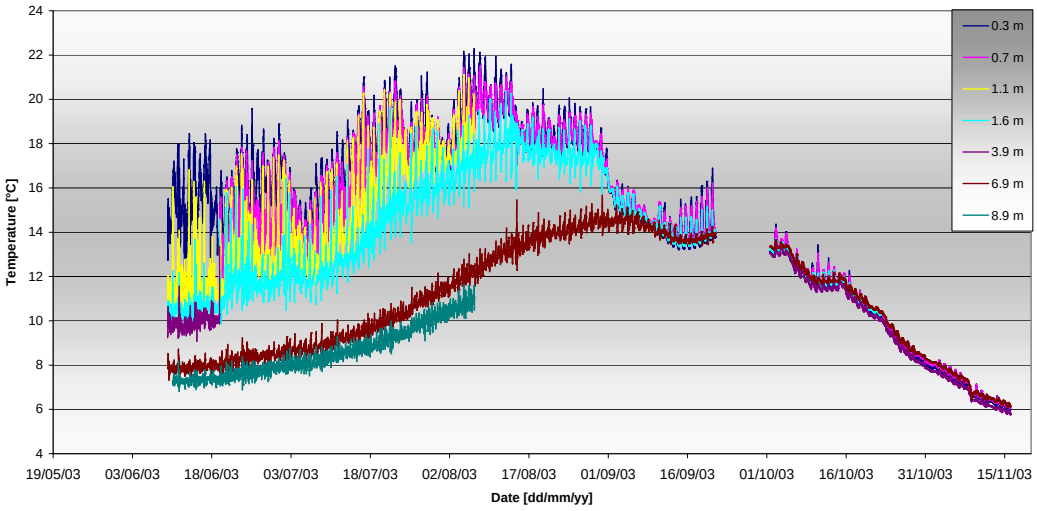

Figure 5.5.: Temperature data collected through chain C.

Chain C

This chain has been placed in the joining slope and reached a maximum depth of about 9 m. Data collected by these probes have been influenced both from the processes of heating

and cooling and by flow exchanges between shallow and deep parts of the lake.

The largest temperature measured in 2003 is 22.17°C (at 16:30 on July 4th); the probe laying on the bottom shows small oscillations around a mean value ranging between 7.2. and 12°C.

Water near the bottom undergoes the influence of daily and periodic meteorological changes, depending up on the variable water transparence, and displays a gradual heating which terminates with the homogenization of the water column, between 13°C and 15°C, in September, after a rainy event on August 30th. The mixing is completely reached in October, when temperature profile shows variations lower than 1°C along the water column.

In Autumn the temperature of the water column decreases progressively until November 15th, reaching a minimum value of 6°C at the end of the record.

Chain D

This chain, located in centre lake, reaches the maximum depth of the lake. The large depth allows one to reconstruct the vertical gradient of temperature and, consequently, to single out the different layers characterizing the stratified lake: the hypolimnion, from bottom (39 m) to roughly 5 m below the free surface and the metalimnion showing a remarkable temperature gradient; however, it's difficult to recognize the presence of the epilimnion, rather a surface mixed layer $0.5 \div 1$ m thick. In summer 2003 the largest temperature measured is 21.46°C, on August 4th, in the evening (19:00) at the surface: it is important to note that, though sun rays reaches the centre lake earlier than Red Bay, the former zone exhibits lower values of temperature because of larger thermal inertia and sensible heat flux exchanged, due to stronger wind blowing on the centre lake.

The process of temperature increase is clear for the deeper zones, where the heating process begins at the middle of June and keeps on until September (for layers between 4 and 8 m of depth) and until October (for layers deeper than 10 m). Unfortunately, due to the wrong setting of the logger, the temperature data in deep zones after September is not available, we can only suppose that the temperature at 20 m remains quite constant, around 8°C, until the end of October, where the lake can mix and gradually cool down.

Temperature at the bottom changes very little, from 4.75 to 5.05°C; the observed levelling of temperature between 38 and 28 m of depth seems to suggest the occurrence of a "monimolimnion" layer.

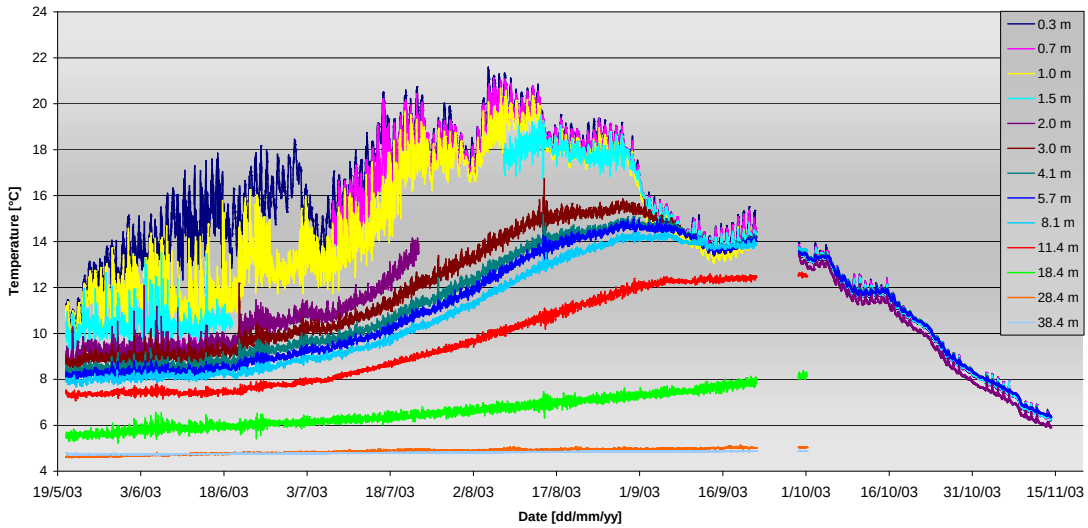

Figure 5.6.: Temperature data collected through chain D.

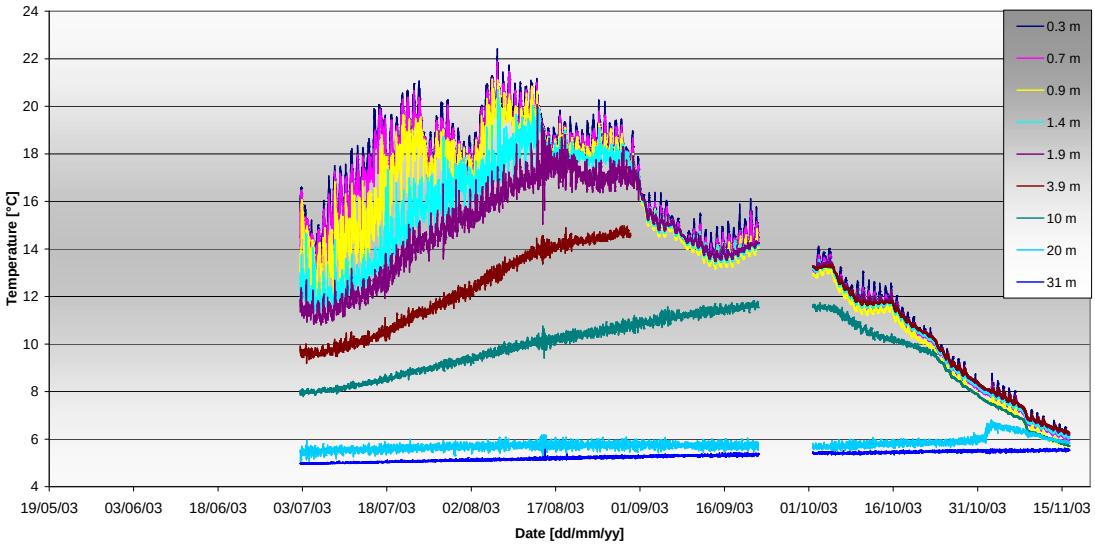

Figure 5.7.: Temperature data collected through chain E

Chain E

Chain E, positioned near the Tresenga outlet of the lake, shows a behaviour similar to the chain located in centre lake.

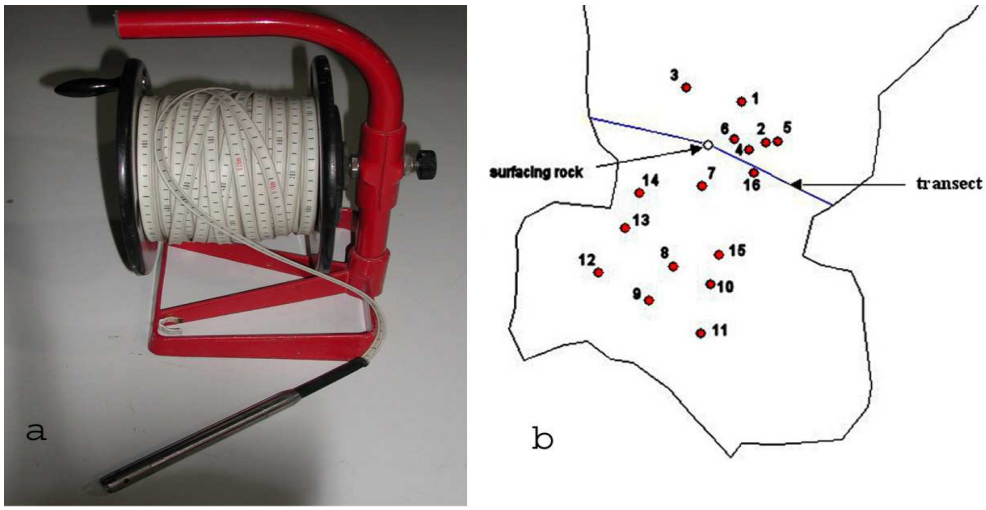

Figure 5.8.: a) Portable temperature sensor; b) sampling points in the South zone of Lake Tovel.

The largest temperature ($22.4°C$) is measured on 6th August at 15:40 in the surface layer.

An interesting behaviour is displayed by the temperature measured at a depth of 10 m: mixing with the above layers doesn't occur in October, such that the temperature remains $1 \div 2°C$ lower until November when the progressive cooling of the lake waters reaches $10°C$. During the cooling period the water in this zone (NO) displays a slightly larger value of temperature than those collected by probes on chain D; however, the discrepancy is always lower than $0.5°C$.

Temperature at the bottom increases extremely slowly, from 4.96 to $5.53°C$, while temperature at a depth of 20 m shows an abnormal increase of $0.5°C$ from November 1st to 3rd.

5.2.4. Local data and instantaneous profiles

Several instantaneous profiles have been measured using the portable probe, in particular within the Red Bay.

The measures have been arranged within a network of points; they provide everywhere similar results. Inside the Red Bay temperature is near $19°C$ in the first meter below water surface; an abrupt decrease occurs within 50 cm, such that from 1,5 m to the bottom the temperature is roughly equal to $6°C$ (see the behaviour of sampling point $7 \div 16$ in figure

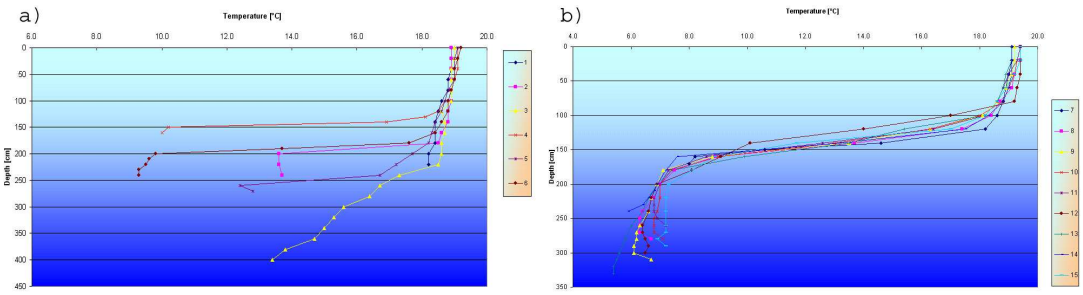

Figure 5.9.: Temperature profiles measured on August 27th and 28th in: a) the mouth of Red Bay; b) inside the Red Bay.

5.9 b). Outside, in the mouth of the bay, we observe different behaviours depending on the sampling point (see figure 5.9 a): generally, the temperature profiles don't show similar gradient except for points 4 and 6, near the surfacing rock called "sasso Tomasi", where we may argue the presence of an underflow channel.

In order to locate the channel a whole vertical lake section has been checked, through temperature collecting. On September 10th, a transect has been measured by pulling a rope from the West to the East end and measuring temperature profile each meter of length. This observations allows us to recognize the presence of 3 channels supplying the main part of the lake from Red Bay, where underground springs converge.

The figure 5.10 shows measures carried out along the transect, dividing the Red Bay from the remaining main part of the lake. The top view helps in recognition of underflow dark blue zones (figure 5.10 b).

The results are summarized in figure 5.11. It is worth noticing that the channels (identified through cold water) not always flow in the deepest parts; furthermore, on the boundary slopes the so-called "thermal obstacle" occurs: since the depth of water column is lower, the heating of this part is greater because thermal inertia is lower and therefore the stratification is mainly horizontal.

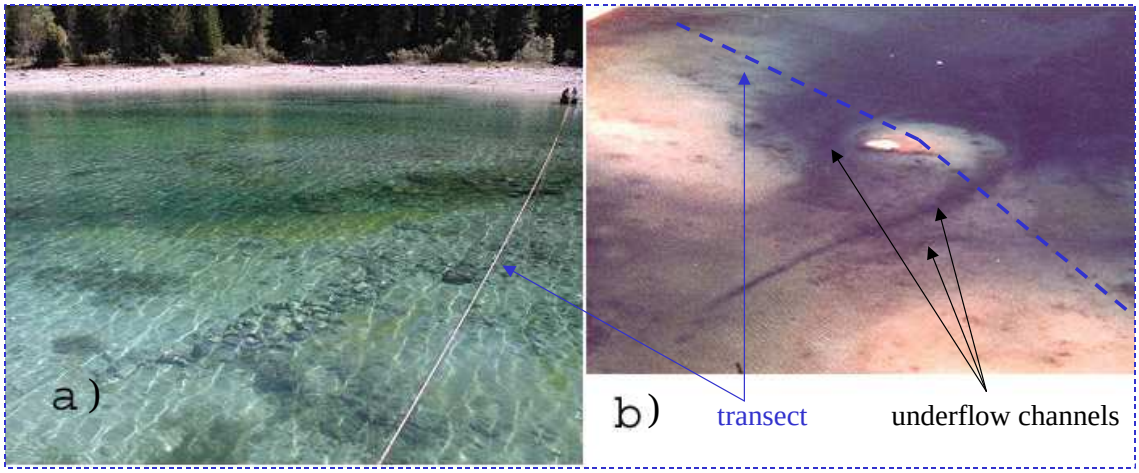

Figure 5.10.: Transect temperature measurements: a) field measurements; b) channels individuation.

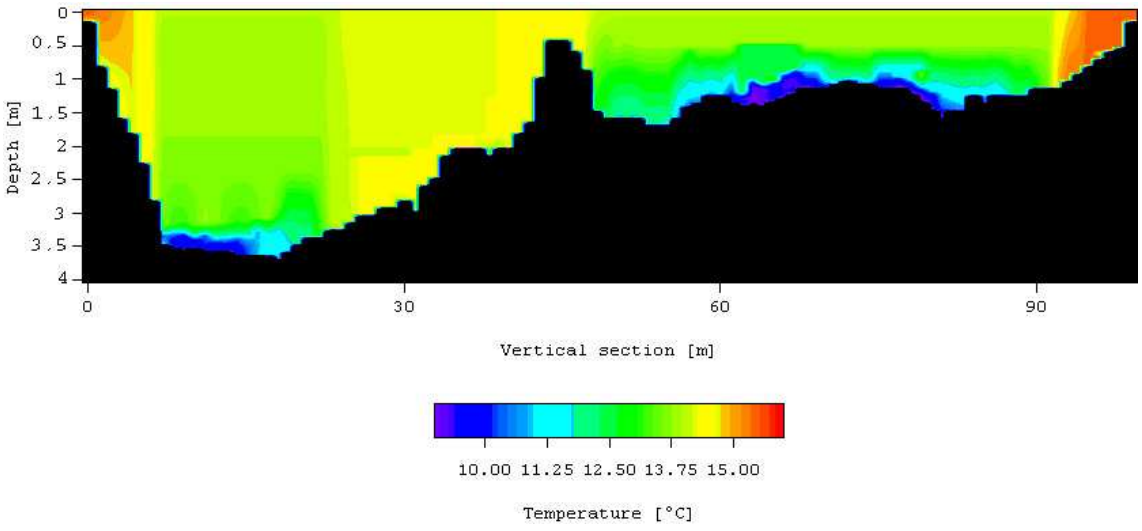

Figure 5.11.: Temperature transect at the mouth of the Red Bay.

5.3. Velocity data

In summer 2003 measurements of velocity field have been conducted with the help of an Acoustic Doppler instruments and a fluxmeter.

5.3.1. Flux meter

A flux meter is a current meter that measures velocity in single points by using Faraday principle. The model is SEBA Hydrometric 801 and can reach a precision of 0.5 cm. Therefore this device is not accurate for lake velocities, which are usually very small, but can provide additional informations. In particular, we have measured the underflow currents that display a relatively high speed, in some cases larger than 10 cm/s. The device comprises a cylindrical sensor with electrodes positioned on the two sides. The volume of measurement has spherical shape with diameter equal to 12cm. This system samples velocity with 0.5 Hz and after averages data on time. The data are stored in a logger always connected to the instrument. For field operation, in order to orientate the device along the main current, a rudder has been arranged on the sensor.

Through the flux meter, an estimate of the flow rate of previous channels has been performed, and data, with due precautions, can be expressed by the following table:

Table 5.3.: Discharges of underflow channels.

channel 1	0.064 $m^3 s^{-1}$
channel 2	0.009 $m^3 s^{-1}$
channel 3	0.094 $m^3 s^{-1}$

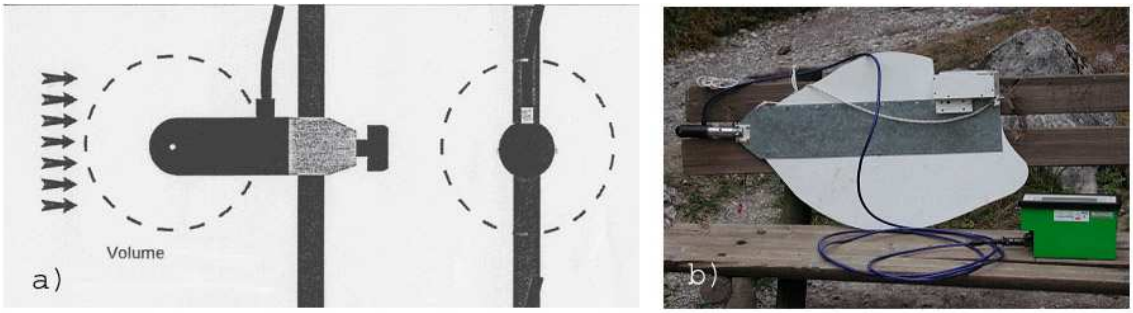

Figure 5.12.: Flux meter: a) scheme; b) device with logger and rudder.

The total supply recognized in a day, supposing constant the flow rates, is roughly 14400 m^3.

5.3.2. Acoustic instruments

All these instruments make use of Doppler effects to obtain velocity values.This well-known effect is due to shifting frequency of sound in case of motion of a wave source or receiver point. In fact, if a source of sound is moving relative to the receiver, the frequency of the sound at the receiver is shifted from the transmit frequency; the frequency received can be expressed as:

$$F_d = -2F_s\frac{V}{C}$$

where V is the relative velocity between source and receiver, C is the speed of sound, $F_{doppler}$ is the change in frequency at the receiver, and F_{source} is the transmitted frequency.

Both transmitter and receiver are constructed to generate very narrow beam patterns. The transmitter generates sound with the majority of the energy concentrated in a narrow cone, and the receiver is sensitive to sound coming from a narrow angular range. The transducers are mounted such that their beams intersect at a volume of water located some distance away. The beam intersection determines the location of the sampling volume (the volume of water in which measurements are made) (Son-Tek, 1996).

The transmitter generates a short pulse of sound at a known frequency, which propagates through the water along the axis of its beam. As the pulse passes through the sampling volume, the acoustic energy is reflected in all directions by particulate matter. Some portion of the reflected energy travels back along the receiver axis, where it is sampled by the Acoustic Doppler devices and processed by the electronics to measure the change in frequency. The Doppler shift measured by one receiver is proportional to the velocity of the particles along the axis of the receiver and transmitter. The axis is located halfway between the center axes of the transmit and receive beams (Son-Tek, 1996).

Each transmitter/receiver pair measures the projection of the water velocity onto its axis. The receivers are aligned to intersect with the transmit beam pattern at a common sampling volume. The velocity measured by each receiver is referred to as the velocity, and is the projection of the 3D velocity vector onto the axis of the acoustic receiver. Velocities are converted by devices to XYZ (Cartesian) velocities using the probe geometry. XYZ velocities give the 3D velocity field relative to the orientation of the probe. These instruments generally are equipped with an internal compass and tilt sensor. The compass/tilt sensor allows to report velocity data in an Earth (East-North-Up) coordinate system, independent

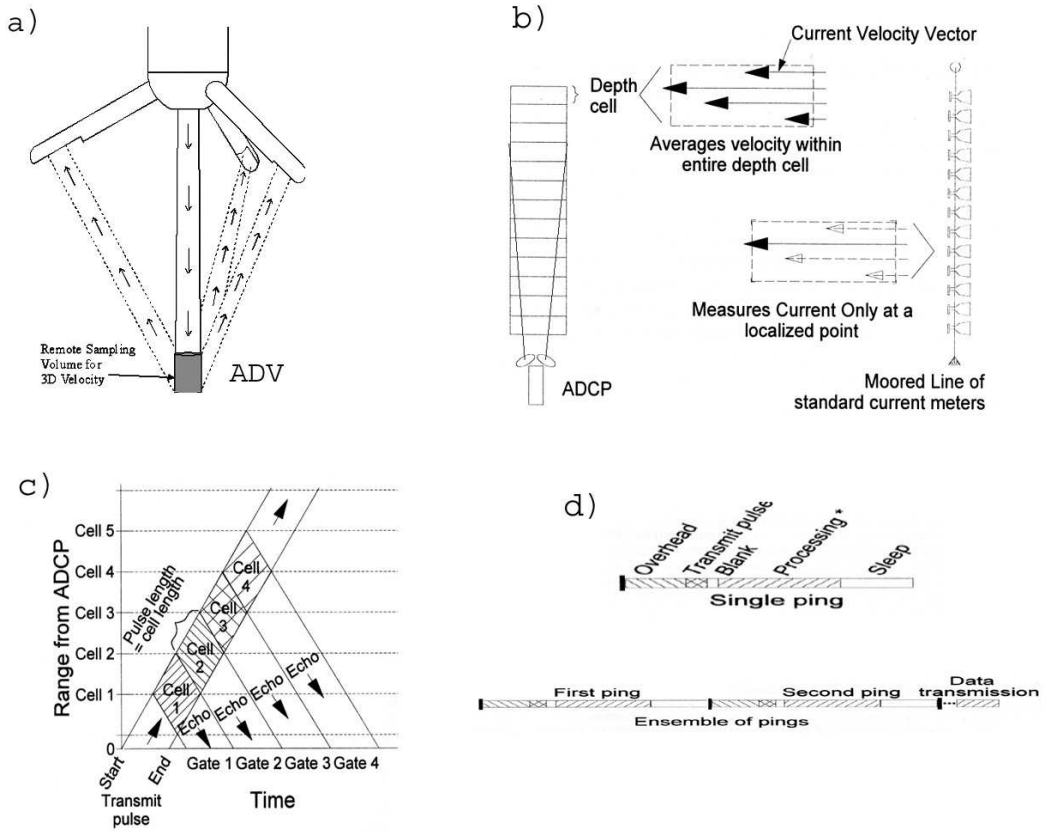

Figure 5.13.: Acoustic instruments principles of operation: a) ADV; b) ADCP; c) range-time plots about transmission and echoes travel d) ping processing cycle.

of probe orientation (Son-Tek, 1996).

ADV

The ADVOcean uses acoustic Doppler technology to measure 3D flow in a small sampling volume located a fixed distance (18 cm) from the probe (figure 5.13 a). The velocity range is programmable from ± 5 to ± 500 cm/s. Data can be acquired at sampling rates up to 25 Hz. The device can be used to measure flow velocities from less than 1 mm/s to over 5 m/s. The standard sampling volume is a cylinder of water with a diameter of 12 mm and a height of 18 mm.

The ADVOcean consists of two elements: probe and processor. The probe includes the acoustic sensors (one transmitter and three acoustic receivers), pressure and temperature sensors. It is connected to the processor using a custom shielded cable. The ADVOcean

processor operates from external DC power and outputs data using serial communication or a set of analog voltages. The processor can be operated from any PC-compatible computer or can be integrated with a variety of data acquisition systems (Son-Tek, 1996).

The ADVOcean records nine values with each sample: three velocity values (one for each component), three signal strength values (one for each receiver), and three correlation values (one for each receiver). Signal strength and correlation are index of data quality: if the intensity of the reflected acoustic signal is wak, because of insufficient particulate matter in the water, than the ambient noise level of the electronics can lead to erroneus data processing as well as the correlation is lower 70%.

The user should select the lowest velocity range setting that will cover the maximum velocity expected in a given experiment (Son-Tek, 1996). Instrument noise in velocity data is proportional to the velocity range setting; higher velocity ranges have higher noise levels. The ADVOcean pings 150-300 times per second. The noise in a single ping is too high for practical use, so the ADVOcean averages a number of pings before outputting a velocity sample. The number of pings averaged is set to meet the user specified sampling rate within the range of 0.1 to 25 Hz.

ADCP

ADCP is a current profiling device which employs acoustic beams inclined typically by 20-30 degrees with respect to the vertical direction. The sonar measures the instantaneous velocity component projected along each beam, averaged over a range cell (RDI, 1996).

Since the "mean" current is typically horizontally uniform over the beams, its components can be recovered as linear combinations of the measured along-beam velocities.

The main difference with respect to ADV consists in making use of Doppler effect on all water column and not just in a single point. Moreover, since the ADCP has four acoustic beams, it can performe the error velocity on the data redondancy.

This device divides the velocity profile into uniform segments called depth cells (or bins). Each depth cell is comparable to a single current meter and therefore an ADCP is like a string of current meters uniformly spaced on a mooring with the difference that the instrument averages velocity over the depth range of each bin while ADV measures current only at one discrete point in space (figure 5.13 b). This averaging reduces the effects of spatial aliasing.

As the time increases, the transmit pulse propagates away from transducer face. Immediately after the transmit pulse is complete, the ADCP turns off the transducer and waits for a short time called "blank period" to allow the transducer to ring down. Velocity

profiles are produced by range-gating the echo signal (RDI, 1996).

Range-gating breaks the received signal into successive segments for indipendent processing. In fact, echoes from far ranges take longer to return to the ADCP than do echoes from close ranges (figure 5.13 c). Thus successive range gates correspond to echoes from increasingly distant depth cells.

Single pulse is not sufficient in order to get good velocity data: single-ping velocity errors are too large. Therefore, data are averaged to reduce the measurement uncertainity to acceptable levels. The averaging is limited by the ping rate, dependent on how fast the ADCP can collect, process and transmit data. Each ping has five phases: overhead, transmit pulse, blank period, processing and sleeping period (figure 5.13 d). After all pings are collected, the ADCP computes an ensemble average and transmits the data to the internal data recorder (RDI, 1996).

The maximum resolution can be achieved by using Mode 5, that is ideal in shallow water (7 m and less for the 600 kHz, 3.5 m and less for the 1200 kHz) with water speeds less than 1-2 m/s. The standard deviation for Mode 5 is very low because there is a relatively long lag between the two pulses (in our case the standard deviation is lower.than 0.2 mm/s).

Measurements

Extensive measurements have been conducted for several weeks, locating the instrument in different parts of the shallow zone, with the aim of understanding the main circulations and flow exchange between the littoral and the interior lake. Moreover a transect has been measured as shown in figure 5.14.

The ADCP has been positioned during the first period, from July 10th to July 17th, at site 1, on the Western part, in order to understand the structure of currents entering in the gulf joining the Red Bay with the interior lake.

The same measurements have been repeated in the period from July 18th to July 24th: both data set display the same behaviour (see figure 5.15)

Then the ADCP has been moved to the opposite side of the joining slope, at site 2, for two weeks (from July 25th to August 8th). The measured data are shown in figure 5.16.

In both cases a periodic behaviour can be identified. We note that in Eastern part, where the slope is mild and the water column is shallower than in the Western part, the dominant color is blue and the corresponding dominant direction is North East, that is outgoing from the Red Bay, while at site 1 the dominant direction, probably the direction entering in Red Bay, cannot be easily identified.

It is worth noticing that the flows don't seem to be affected by wind direction, since they

Figure 5.14.: ADCP measurement positions

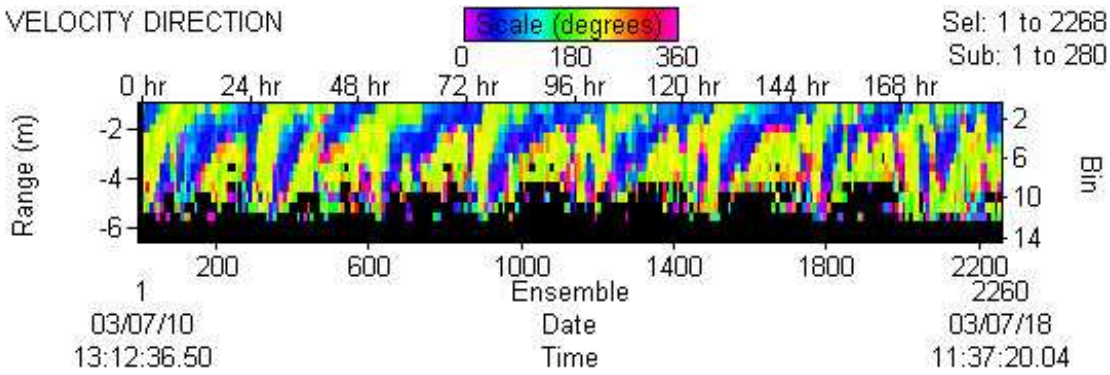

Figure 5.15.: Velocity Direction measured by ADCP on the water column in place 1.

move "countercurrent" in both cases. In fact, during the day, when the wind is blowing toward the Red Bay, water moves to NE direction, while only in evening, when the wind blows in SW direction, the flow direction looks at the bay.

From August 8th to 20th the device has been placed in Red Bay, at site 4. In this case the flow pattern is dominated by NE direction due to the flow released in the lake by underground springs. From figure 5.17 it appears that only at the surface some color changes are distinguishables which implies the rotation of velocity vector: every day in the afternoon (and until midnight) the velocity is directed toward South (even in this case the

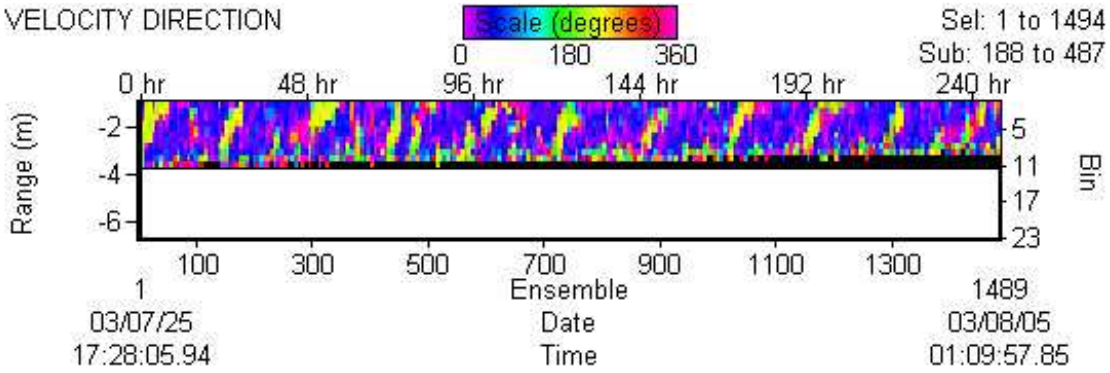

Figure 5.16.: Velocity direction measured by ADCP on the water column at site 2.

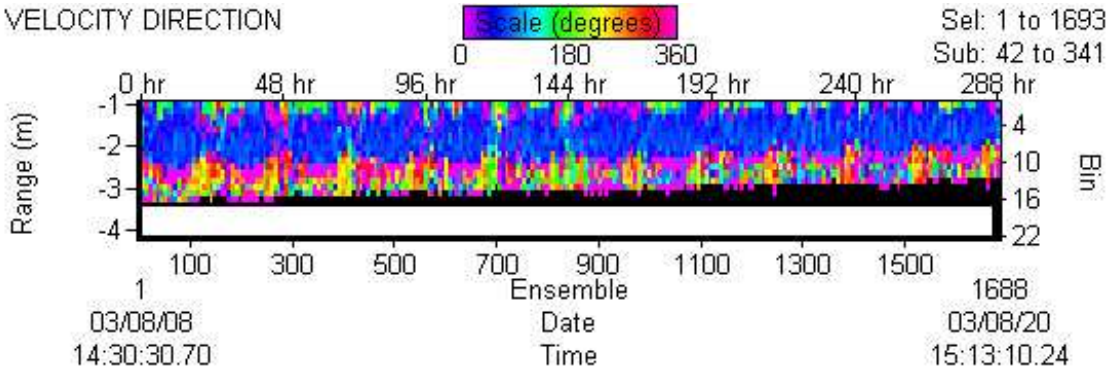

Figure 5.17.: Velocity direction measured by ADCP on the water column at site 4.

water flows "countercurrent"). Unfortunately, the ADCP cannot measure within the first and the last meter on the water column; hence, information on the actual motion occurring in surface layer is not available.

Notice that the number of missing data at the bottom increases a lake level lowers.

In the end of August the ADCP has been moved to site 3, just above the underflow discovered through intensive temperature measurements.

The data collected (see figure 5.18) show the presence of a current at the bottom, whose direction is always North, while flow direction changes above; the intensity of bottom current is very high and exceeds 10 cm/s. Peaks of velocity repeat each day at midday, while velocity is always vanishingly small in the upper layer.

On September 4th some measurements at sites I, II and III (figure 5.19) have been

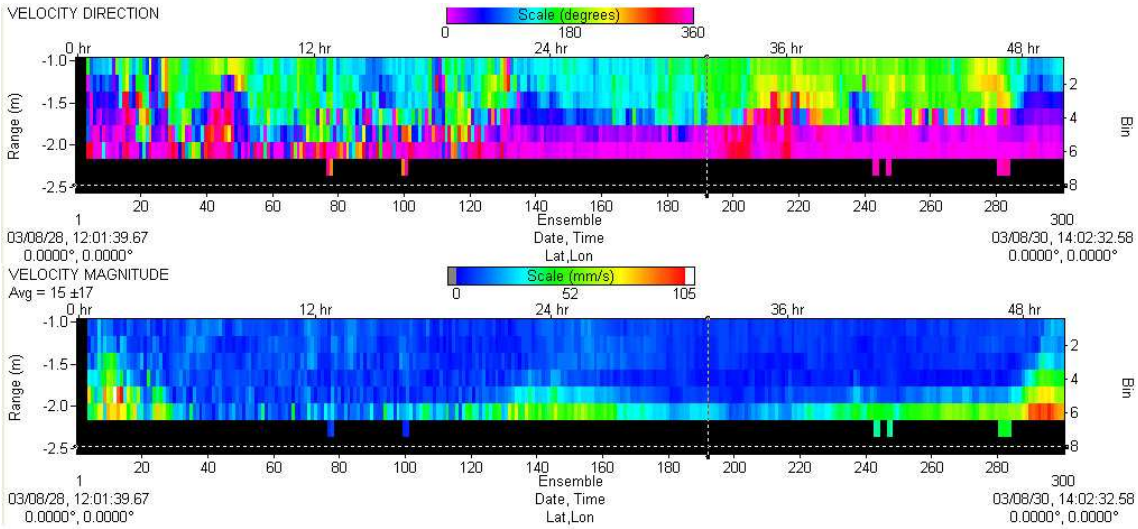

Figure 5.18.: Velocity direction measured by ADCP on the water column at site 3.

performed with ADV, along a transect in the gulf near Red Bay from the Eastern to the Western part.

Figure 5.19.: ADV measurements position.

The results are shown in figure 5.20. Unfortunately, in order to move up and down the device with sufficient precision from the rubber dinghy, we were not able to measure velocity near the water surface.

In the morning, in the Eastern shallow zone the currents move in SW direction on the entire water column (only 2.5 m of depth). In central zone the current moves again in the same direction, entering in Red Bay, only within the first 1.5 m; below, an inversion occurs

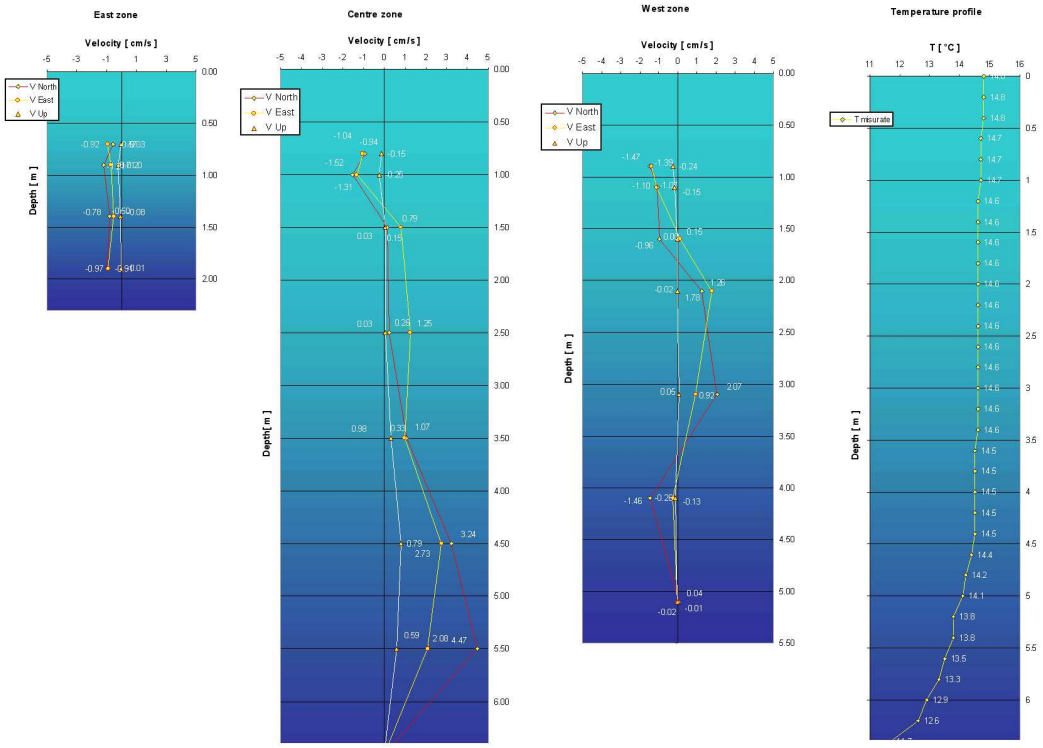

Figure 5.20.: Measurements of velocity field carried out through ADV in place I, II and III in the morning of September 4th.

and flow is outgoing from the bay, whose intensity increases as the depth increases. In the West side, current shows different behaviour: in the upper part flow moves always toward the bay, at 1.80 m of depth it turns toward the centre lake and below 3.80 m of depth it turns again in opposite direction.

We must note that the temperature profile changes slightly from the central part to West side: in the centre, it keeps homogenous until 5 m of depth, while in Western part it starts decreasing after 4 m of depth, as shown in figure 5.20.

In the late afternoon the same measurements have been repeated (see figure 5.21).

The circulation now is outgoing from Red Bay at the sides of the transect, within the first 3.5 m of depth, while in central part the dominant direction is opposite, even if intensity is low. Below the depth of 4 m the velocity is directed toward the Red Bay even in the West side. In this case, since measurements have been performed after 17:00, the wind is blowing toward NE direction.

This set of data seems to confirm that currents follow, on the average, the wind direction

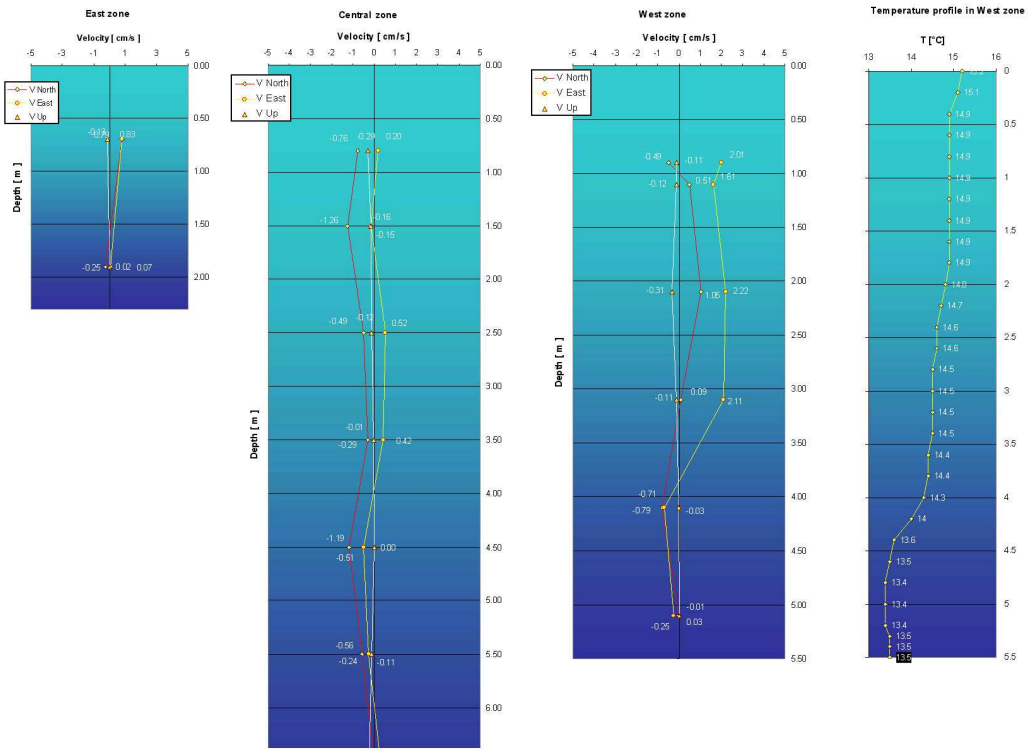

Figure 5.21.: Measurements of velocity field carried out through ADV in place I, II and III in the afternoon of September 4th.

near the shores and go countercurrent in the middle.

On September 16th some transects have been performed; in the afternoon an interesting phenomenon is observed: in fact, because of the presence of sheltered zones in Red Bay and the deviation of wind direction, the currents show a different behaviour in the West side with respect to the East side of the lake.

Directions are not always clearly distinguishable (see figure 5.22) but it seems that flow moves toward Red Bay (200°) on West side and comes back on the other side (80°). Measurements give the same result even when carried out along two parallel transects near the mouth of the bay.

The first transect (a) is the further to Red Bay: the flow is outgoing from the bay only in the superficial part; in second transect, closer to the bay, the circulation is clearly detectable. To confirm these data some additional measurements have been performed with ADV at two sites in the morning and in the afternoon of September 16th and 17th.

The measurements show that at site IV (figure 5.23) in the morning (a) and in the

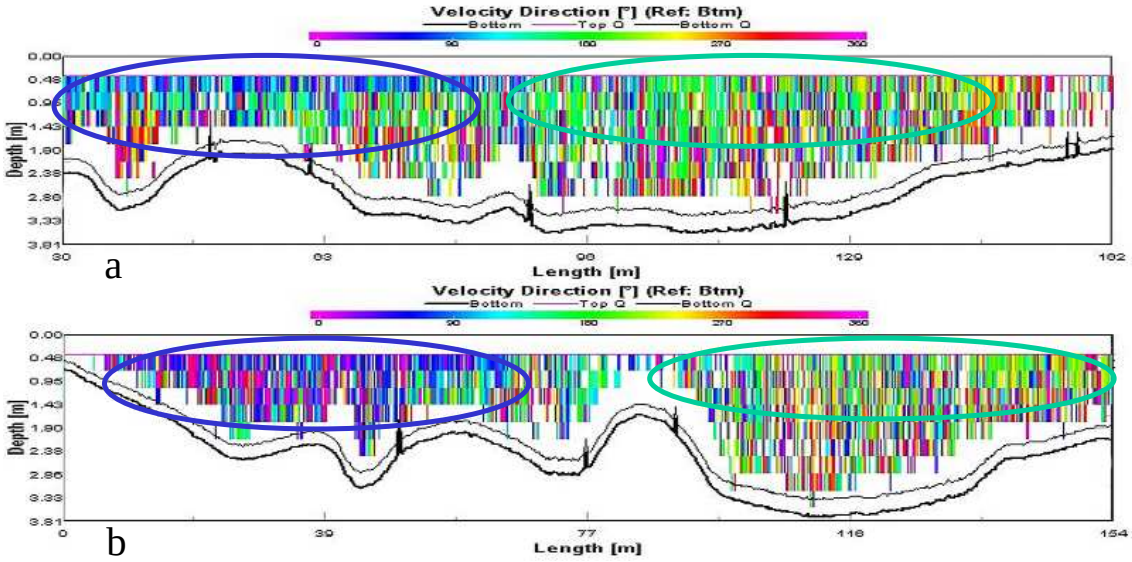

Figure 5.22.: Transects carried out trough ADCP in front of Red Bay on September 16th.

afternoon (b) the flow is directed to the Red Bay: in fact, North velocity is negative in both cases, while the East component is negative or slightly positive. As the depth increases, the velocity shows an inversion and the water is outgoing from the bay.

At site V the East velocity is positive at the surface and changes direction below 30 cm; the North velocity is in turn positive in the surface layer and negative below. Therefore the circulation displays a East direction near the surface (d), while below a North North-West component seems to predominate (c).

Finally, the ADCP has been positioned again at site 1 in October: the circulation shows an unespected total different dynamics (see figure 5.24).

In this period the lake can be considered unstratified and the circulation is not influenced by internal wave. The flow on the water column, with the exception of bottom part, is directed to South for the whole period, while in the deep zones a current with opposite direction establishes. Again the first meter is not measured; however, the remaining part of the water column doesn't respond to change of wind direction; the circulation is probably connected to differential cooling between shallow and deep zones of the lake.

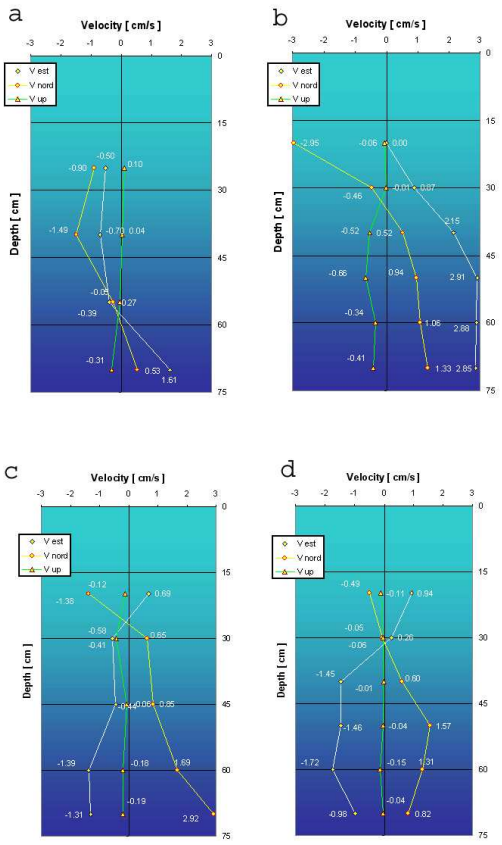

Figure 5.23.: Currents measured by ADV on September 16th at site IV and V in the morning and afternoon.

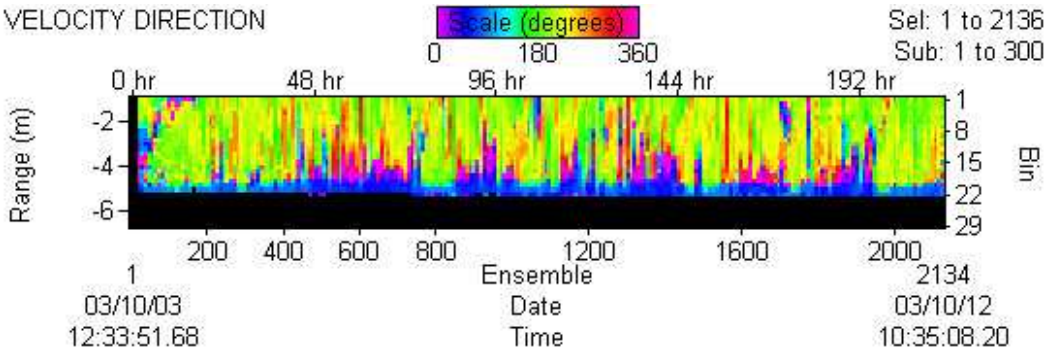

Figure 5.24.: Velocity direction measured by ADCP at site 1 from October 3rd to October 12th.

5.4. Lagrangian path data

5.4.1. Drifters

Lagrangian techniques have been widely used in the study of oceans and large lakes, both for fundamental fluid dynamics as well as for environmental problems. The data provided by 'drifters' following currents are particularly valuable to determine the spatial structure of the flow field and provide a complementary understanding of the flow dynamics with respect to that which is obtainable from Eulerian data. Lagrangian data also allow diffusion coefficients to be estimated more realistically than with fixed current-meters (Stocker and Imberger, 2002).

The recent advent of the Global Positioning System (GPS) has made possible the collection of good data through Lagrangian drifters. GPS is a worldwide radio-navigation system which employs a constellation of 24 satellites; up to eight are used at any time to determine the position of a receiver. Until May 2000, Selective Availability (SA) deliberately degraded the publicly available signal for military purposes and limited the accuracy to approximately 100 m. This effectively restricted the scales of motions that could be resolved, though improved position fixing was possible with differential correction through a fixed base station and additional signal processing. Now, with the removal of SA, data with less than10 m order can be resolved with non-differential GPS (Johnson et al., 2001).

5.4.2. Design

The GPS receiver units have four primary components: an instrument floater casing, a receiver/antenna system, a datalogger and a power source.

The main casing is a 17 cm PVC pipe with standard end fittings from a hardware store (Johnson et al., 2001). The GPS receiver and the datalogger are mounted on an internal instrument frame, while a battery pack is arranged on the other side of the same frame. A LED on the logger indicates the status of the device, indicating power on/off, whether good data are being received. Data are stored in a memory card of 128 Mb and downloaded through a special reader connected to PC by COM port. Output data also include a status code marking the start of each data sequence, such that the logger can be used for multiple deployments without downloading operations. The data include day, month, year, hour, minutes and seconds of measurements, latitude and longitude expressed in WGS84 coordinates system.

The GPS is a Novatel Superstar receiver, with declared position accuracy lower than 1,5m. Maximum verified displacements from the mean position is 4.2 m and 5.2 m, time

to acquisition is approximately 45 s.

Since the GPS signal cannot travel through water, the antenna lies on the water surface.

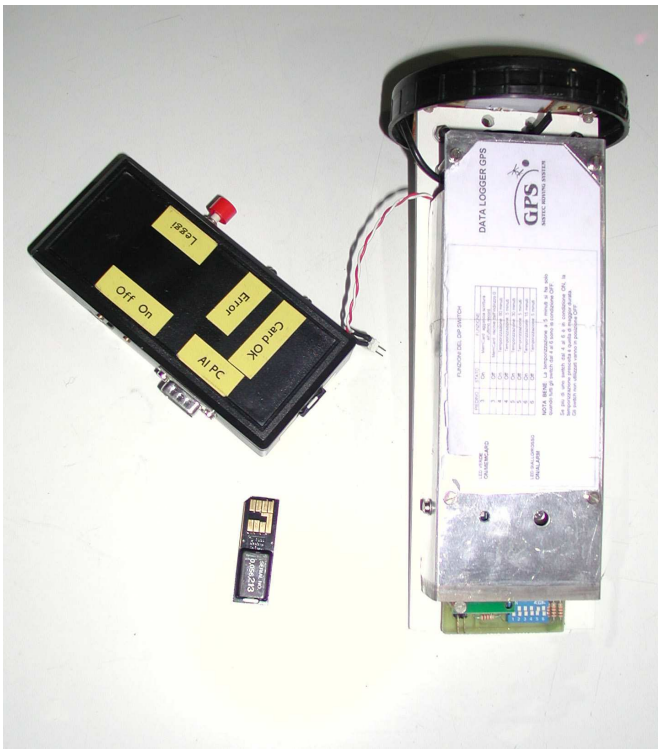

Figure 5.25.: GPS used in the buoy, memory card and card reader.

For subsurface applications, the factors which influence the performance of a drifter as a Lagrangian current follower are wind-induced slippage and wave drag on the surface float due to the finite size of the drogue (Johnson et al., 2001). In particular, it is very important to respect the ratio between the drag area of the drogue and that surface float area, where the drag area of a component is defined as its area times its drag coefficient. For an area ratio larger than 40 it has been demonstrated that wind-induced slippage is less than 1 cm/s when the wind is strong and blow with 10 m/s speed.

In our experiments the floater casing containing the GPS system has a volume of 2,3 liters: the area that the wind can influence is 150 cm^2, while the area of the submerged flat boards is about 6400 cm^2; hence the minimum volume of the area ratio is respected.

5.4.3. Measurement

In Lake Tovel 22 experiments have been carried out, mainly at the surface; the last experiments have been performed at 5 m and 10 m depth.

The drifters have been deployed at different locations in the lake, with two aims: the first was to understand the superficial currents entering in Red Bay, the second was to characterize the general circulation in centre lake.

Experiments a and b (figure 5.26) have been performed in the morning; they give a qualitative idea of the oppositing currents developing in the gulf and in the main water body. In particular, experiments a and f highlight the importance of passive transport that could accumulate red algae from roughly "an half lake" to Red Bay. In the experiment e, the drifter runs aground and stops before the bay because of scarce depth (in September the water level was 2 m lower than in July!). Experiment d, which lasted 3 days, displays big vortex occurrence, depending on wind direction reversal.

Several other experiments have been carried out with more drifters: figure 5.27 shows the results of experiments with drifters positioned just 75 cm below the water surface, while in figure 5.28 the trajectories of drifters positioned at a depth of 5 m or 10 m of depth are reported.

Experiments A and H (figure 5.27 and 5.28) show the occurrence of large eddies due to the effect of boundaries in the NE part, while the experiments D, F2, K2 reveal a circulation in the opposite direction in NW zone. Experiments C and J show the influence of boundaries in the joining gulf, where drifters can move countercurrent.

It is worth noting that drifters located at a depth of 10 m run more slowly than those at 5 m, which, in turn, are slower than drifters positioned in the surface layer (experiment F1 and G); furthermore, they often follow an out of phase direction or respond with a time lag with respect to superficial drifters.

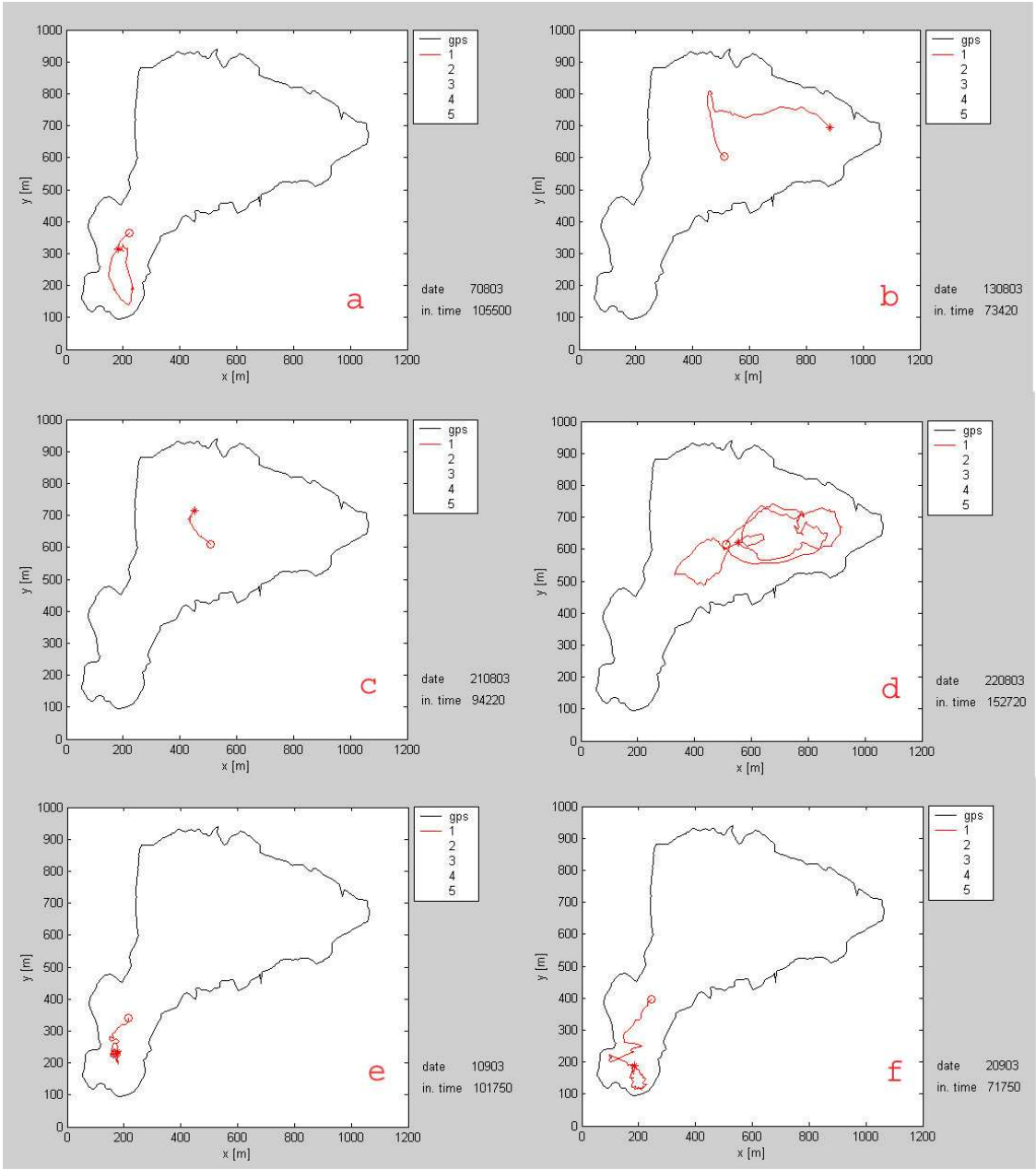

Figure 5.26.: Single drifter experiments.

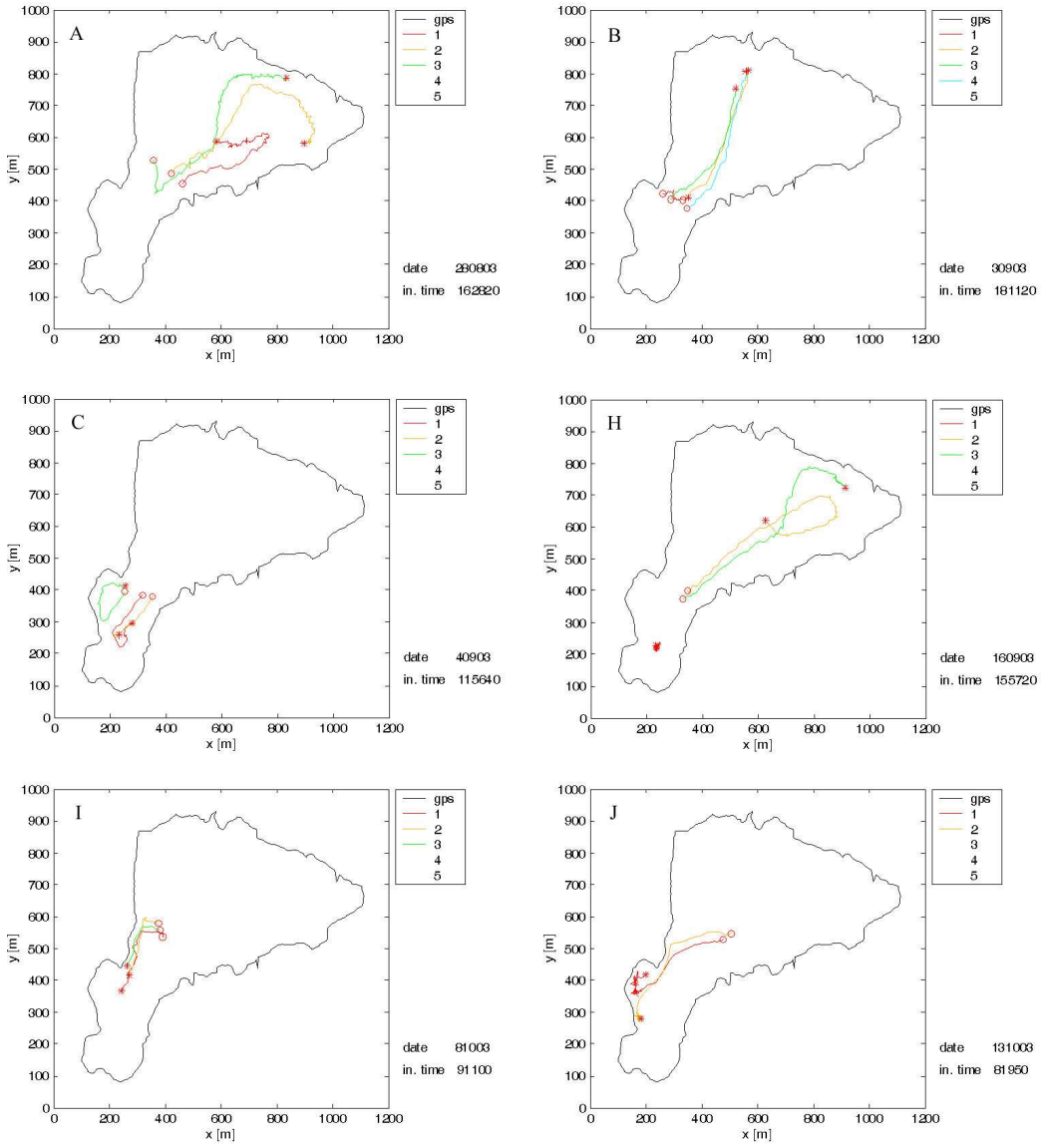

Figure 5.27.: Experiments with drifters positioned in superficial layer.

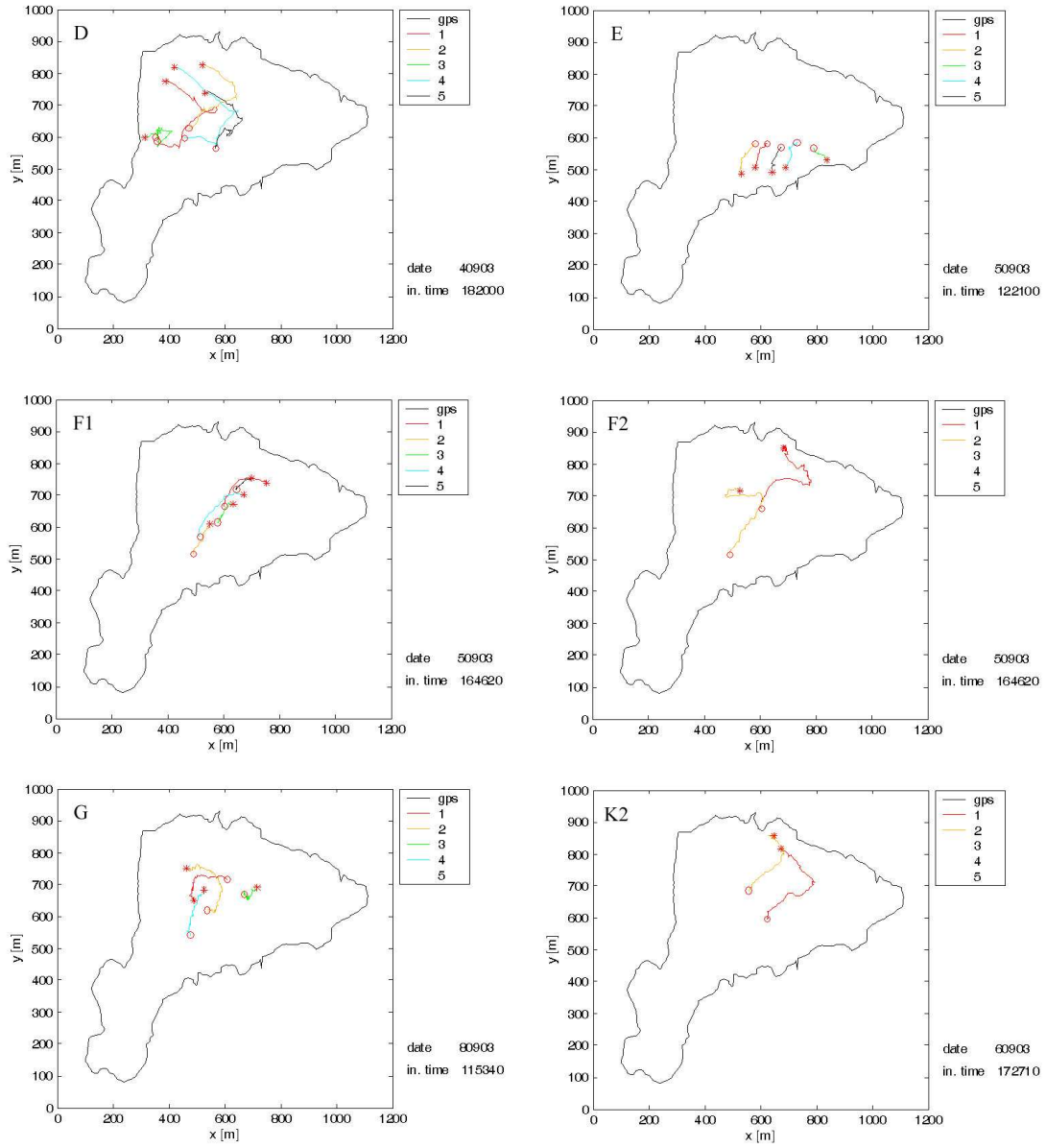

Figure 5.28.: Experiments with drifters located at a depth of 5 m or 10 m.

6. Data analysis

6.1. Temperature

As a first step in the postprocessing of collected data the measured values of temperature have been used to reconstruct the isotherms. Isotherm lines provide an overall view of the distribution of input heat energy in the lake, enable us to understand whether the solar penetrative radiation can reach a certain region of the lake and provide further information about internal motions. Hence, their knowledge is extremely important to determine the internal dynamics: temperature, in some cases, can be treated as a passive tracer and the movements of the lake can be traced looking at the displacements of isotherms.

As pointed out before the zone of Centre lake, where the chain D was positioned, is representative of the main dynamics occurring in lake Tovel.

In figure 6.1 the euphotic layer can be clearly distinguished from the deeper zone where the light can't seep. The centre lake, unlike the Red Bay, is lighted up in the first morning and the direct solar radiation ceases in the afternoon, later than in Red Bay.

The diurnal heating cycle manifests itself only in first 3 meters from surface. Below, isotherm lines keep nearly horizontal from May to July; after that period it is possible to distinguish a gradual deepening due to seasonal heating: the isotherm corresponding to $6°C$ moves from 20 m to 25 m deep in two months, the line corresponding to $8°C$ deepens slowly from 8 m to 20 m during the summer, while the $10°C$ isotherm displays a sudden deepening in July (from 3 m to 14 m) and changes mildly in August. Bottom temperature changes from $4.75°C$ to $5.05°C$.

The diurnal weather changes influence only the first 3 m of depth and even during the rainy event occurred in the middle of July we can only appreciate a surface cooling while the isotherm corresponding to $14°C$ keeps stable.

At the beginning of October the stratification is weak: the isotherm corresponding to $10°C$ reaches the surface; in November, due to heat loss, the water column shows a good uniformity, with a vertical gradient lower than $2°C$.

Cooling processes are evident and influence the isotherms behaviour: all lines corre-

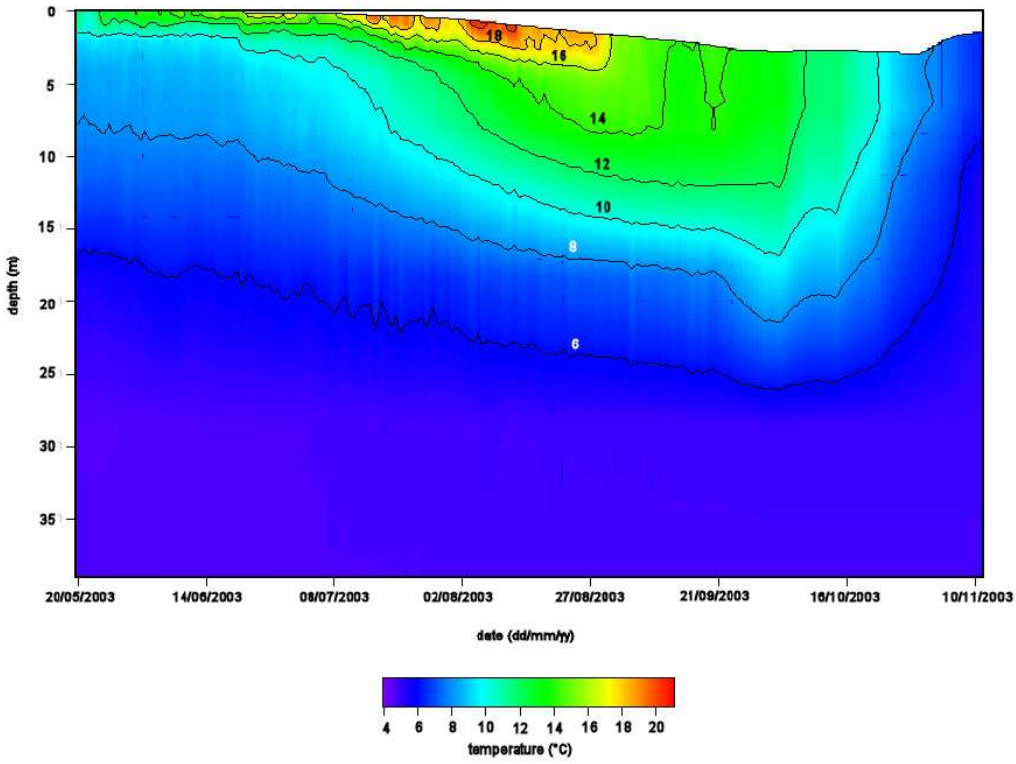

Figure 6.1.: Isotherms behaviour in Centre Lake.

sponding to $14°C$, $12°C$, $10°C$, $8°C$ reach the surface quickly because the heavy cold water at surface fall down in gravitational plumes able to mix the water column.

The temperature profiles show the presence of a deep zone which remains unchanged for all the period of observations. This fact suggests the establishment in the lake of a separate layer where the vertical transport is negligible and the diffusivity roughly molecular. Limnologists call this zone "Monimolimnion".

Above this layer the mixolimnion develops, where the mixing processes occur: here, temperatures change but slowly. In fact, the temperature gradient remains for the main part lower than the conventional thermocline gradient (indicated by a dot line in figure 6.2). All this zone belongs to the hypolimnion, that in May arrive until 2 m of depth. With the Summer advancing the thermocline erosion increase and the limit between hypolimnion and surface mixed layer moves from 3 m in June to 5 m in July, 8 m in August and 10 m in September.

We may observe that an epilimnion, as conventionally defined, doesn't establish: the

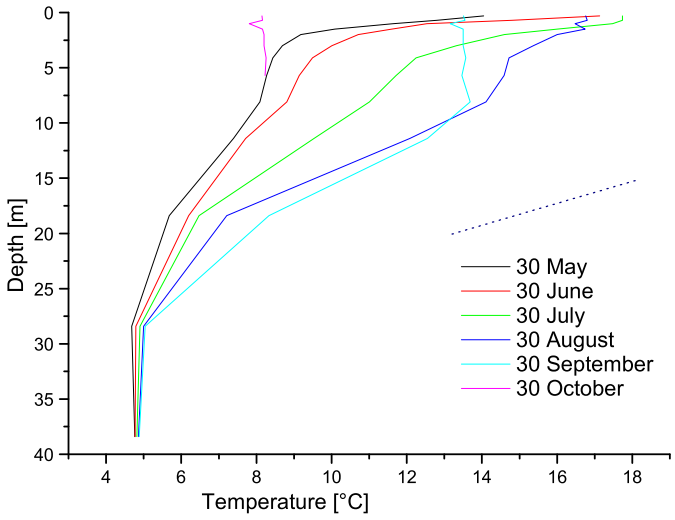

Figure 6.2.: Temperature profiles in Centre Lake.

wind is to weak to form a well mixed layer at the surface and cooling process is needed to cause an homogenous layer of sufficient thickness.

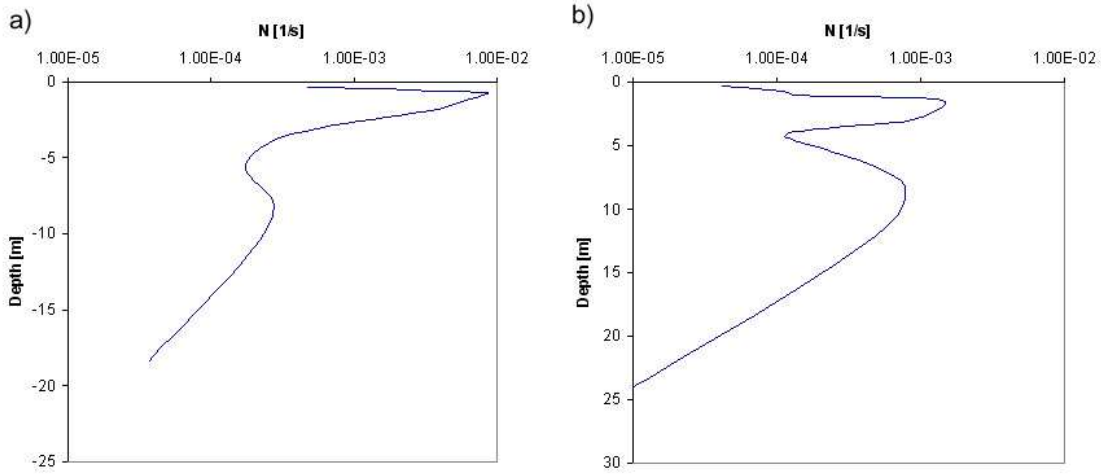

Figure 6.3.: Buoyancy frequency: a) July 30th; b) August 30th.

The figure 6.3 shows the Brunt-Vaisala frequency (N) behaviour for two different periods in the summer season.

The periods of the seiche modes calculated for rectangular basins is:

$$T_{n,m} = \frac{2\ L}{\sqrt{g\lambda_n}m}, \tag{6.1}$$

where n stands for the vertical mode and m for the horizontal mode, λ is the eigenvalue of multi-layered linearized momentum equation (Munnich, 1992).

For the case of July, we can estimate the seiche periods reported in table table 6.1 for the horizontal mode 1° and the vertical modes 1° and 2° at different depths :

Table 6.1.: Estimated period of seiche vertical mode.

Depth [m]	Period [h] of 1° mode	Period [h] of 2° mode
1	8	8.3
1.5	10	4.5
3	16	3.1
4	24	2.7
6	19	2.1
8	10	1.7
11	7.5	1.3
18	10	1

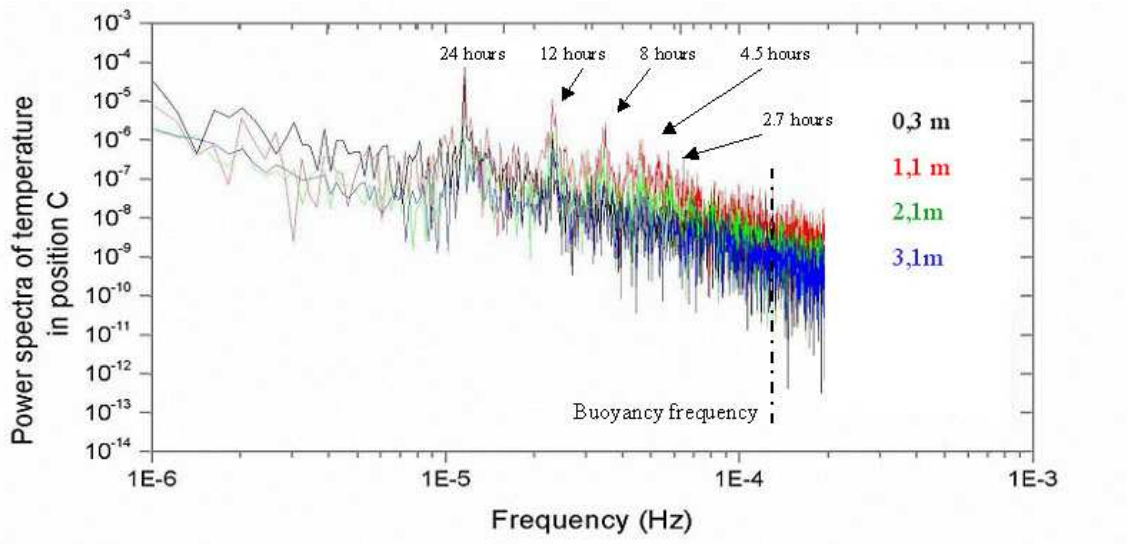

Figure 6.4.: Power spectra of temperature for the superficial sensors in chain C.

All this periodicities within the zone of highest buoyancy frequency (from 1m to 6m

below the water surface) are observed in the real context with small differences due to theoretical approximations (see figure 6.4).

Data collected by thermistors arranged on the chain D in the Northern part of the lake display a similar behaviour.

Measured data only suggest a larger deepening of the $14°C$ isotherm. Summer stratification is clear until September and the diurnal heating is well recognizable, with a deepening of isotherms around midday, that is before the occurrence in the Red bay because sun rays can reach this zone some hours early. During September heat supply by solar radiation decreases and the isotherm line corresponding to $14°C$ deepens and vanishes quickly within in the first meter of depth. The stratification becomes weaker and water column can be considered as homogenous in November

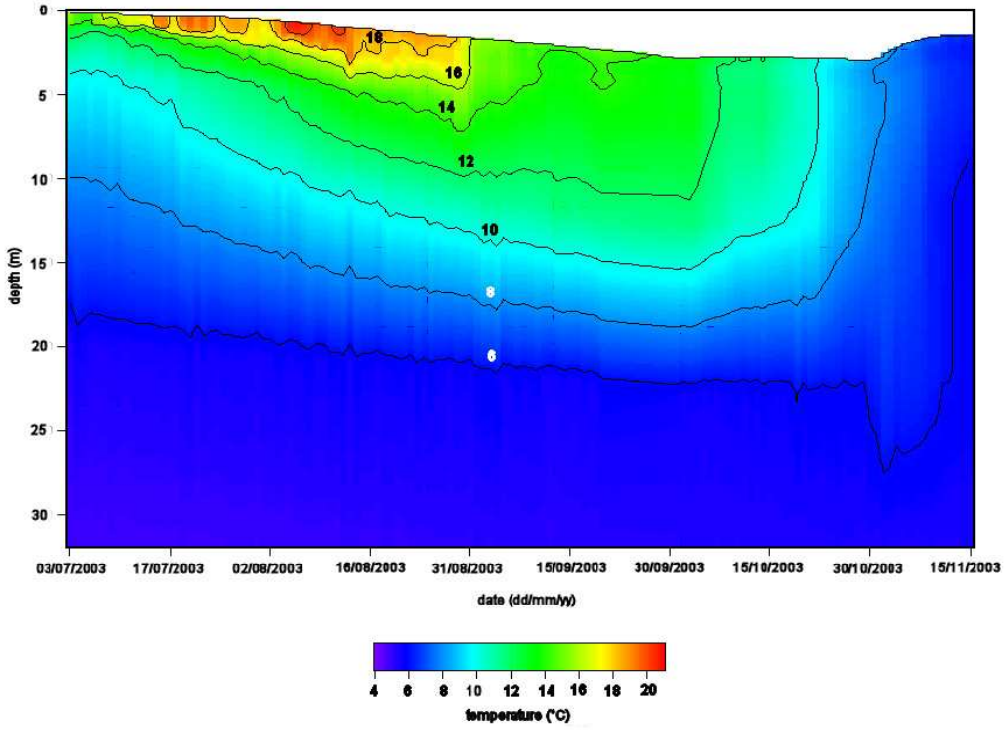

Figure 6.5.: The pattern of isotherms near the outlet zone.

The period between August 2nd and 13th is characterized by a strong insolation; hence, the lake reaches the highest value of temperature. In these days, in the gulf near Red Bay, where chain B is positioned, the heating is strong, as shown by the structure of isotherms close to the surface, and the cooling starts at about 18:00, at the sunset, and continues

during the night until 8:00 in the morning, without going below $12°C$.

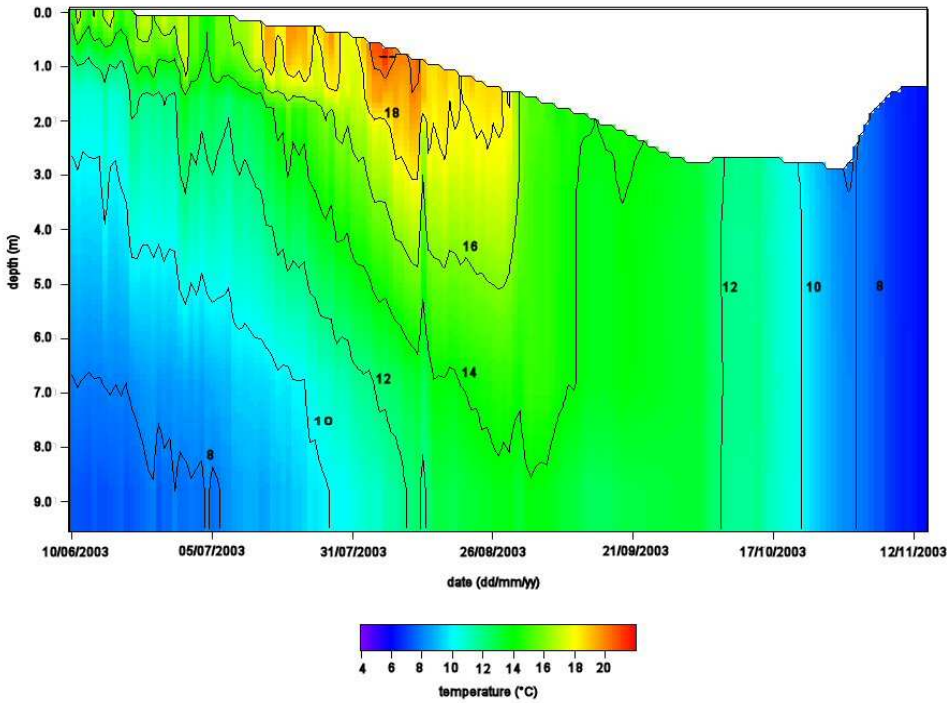

Figure 6.6.: Isotherms structure in the joining part (chain C).

In the part joining the gulf to the deep interior the effect of the strong wind which occurred on August 14th and influenced the whole water column, is clearly visible.

The maximum deepening of the $14°C$ isotherm reaches 8,5 m nearly at the middle of September and slightly later the water column becomes homogenous.

In Red bay the behaviour is different from the other parts because the underground springs supply cold water that remains confined in this zone and slides down toward the deep interior lake by a thin underflow. The highest diurnal temperature is reached at $16{:}00 \div 17{:}00$ and the isotherms deepen just after midday, when the bay is directly irradiated by the sun.

In the first week of August the Red Bay reaches the maximum temperature and the bay keeps a temperature $1 \div 2°C$ higher than the centre lake (see figure 6.8), essentially because of the lower thermal inertia. In fact during the night, for the same reason, we observe a greater cooling and the bay keeps a temperature $0.5°C$ smaller than in central zone of lake Tovel.

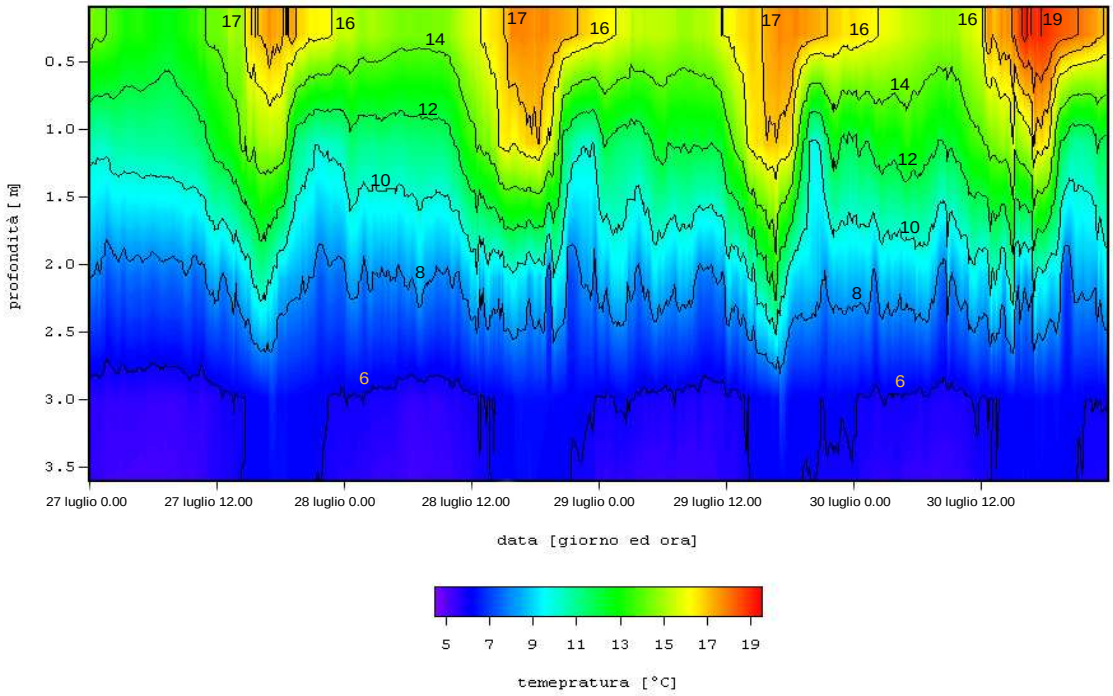

Figure 6.7.: Isotherms structure in SO gulf near Red Bay from July 27th to November 4th 2002.

The greatest temperatures are reached generally between 16:00÷18:00, before the solar incident radiation decreases quickly and sun disappears behind mountains. Later, heat is lost gradually until 8:00÷9:00 in the morning, when the radiation feeds again energy to the lake. The trend is positive and reflects the summer' heating cycle: each day seems to bring an energetic contribution to the lake and superficial temperature keeps on increasing.

From figure 6.8 it also appears that while the superficial temperatures show an intuitive behaviour, data referring to the adjacent layer display a peculiar trend: in particular, in Red Bay we observe an abnormal temperature increase during the night, while chains C and D interesting fluctuations occurring at a depth of 0.7 m. This peculiar behaviour can't be related to heat fluxes, but it is due to internal motion.

To understand it in detail, let us focus our attention on what has occurred in the lake during some typical days, like July 21st or 22nd.

The first day is characterized by a disturbance, which it is clearly recognizable by the behaviour of solar radiation that shows narrow peaks, indicating cloud formation (see figure 6.9). Moreover the wind speed is strong and exceeds 4 m/s.

When the wind changes direction, at first the intensity keeps relatively high values.

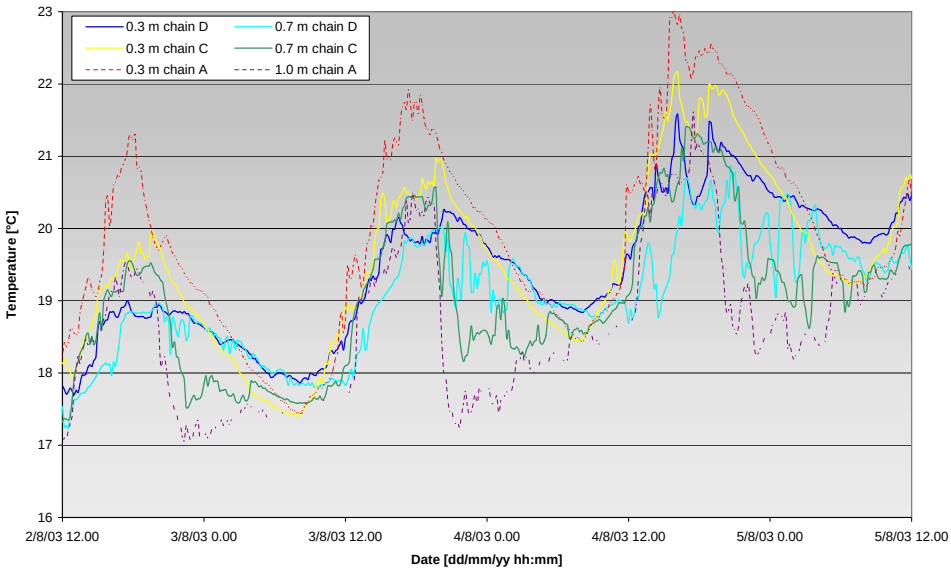

Figure 6.8.: Comparison between temperature measured in Red Bay (chain A), Joining Slope (chian C) and Centre lake (chain D).

This fact causes a succession of thermal stresses within the intermediate layers of the lake: in fact, internal waves move up and down and thermistors located at a depth of 1 m exhibit oscillation falling within the range $3 \div 4°C$. In particular, the thermistor of chain D, in centre lake, shows a strong oscillation around his equilibrium position (around $16.8°C$), with a period of roughly 1.5 hour and an amplitude decreasing gradually from $1°C$ because of internal dissipation.

Similar fluctuations are distinguishable for chain C and A, superimposed on an increasing trend. In these cases, sensors positioned 1 m below water surface show this kind of movements in phase opposition: it physically means that a seiche motion is occurring with an isopycnal surface moving up in Southern part and down in the central zone and viceversa. In the North end of the lake, data collected with chain E are out of phase and indicate the presence of other harmonics besides the horizontal mode 1.

At the surface, sensors are not influenced by these movements and temperatures decrease continuosly until 8:00 in the morning, when the heat loss is maximum. At this stage the radiation starts to supply the lake again. The second day is characterized, unlike the previous one, by calm wind and clear sky as shown in figure 6.9. We can distinguish clearly the time (14:00 hours) at which a sudden temperature reduction occurs in Red Bay

and a corresponding sudden increase occurs in chain E, on the opposite end of the lake.

A short change in wind direction is sufficient to allow the tilted isopycnal surface to move down in the Northern part (chain E), with a relevant temperature increase from 15.00 to 17:00 hours. In turn, sensors positioned on chain A and chain C, (Southern part) exhibit relatively strong changes: temperature decreases quickly from 17:30 to 20:00 of nearly $4°C$. Also the chain D, situated in centre lake, feels these changes and temperature starts to oscillate around its equilibrium value.

During the night, the two sensors in chain E display similar values of temperature which indicates the occurrence of a tilted internal surface that deepen in Northern part at a depth of 1 m: in fact, during the night, the wind blows in opposite direction with respect to diurnal direction and accumulates warm superficial water to the North end. However, even in the Red bay temperature increases at middle depth, probably because of seiche formation of horizontal mode higher than 1.

Hence, the structure of isotherms is also related to wind in addition to solar radiation. This fact finds clear evidence in figure 6.10 where deepening is greater when the wind is stronger.

6.1.1. Calculation of basin-wide diffusivity

Basin-wide diapycnal eddy diffusivity coefficient can be calculated over time by measuring the hypolimnetic heating rate and vertical temperature gradients from continuosly measured profile in Centre lake (chain D). This method, called "heat budget method", is based on the assumption that, at depth z, the vertical turbulent transport of heat balances the rate of change of heat content below z (Goudsmit et al., 1997). Hence, the eddy diffusivity is given by:

$$\overline{k_z}(z) = \frac{\int_0^z A(z') \frac{\partial T(z')}{\partial t}\, dz'}{A(z) \frac{\partial T(z)}{\partial z}}, \tag{6.2}$$

where $A(z)$ is the cross-sectional lake area and $T(z)$ is the water temperature at depth z.

The application of this method involves the removal of temperature oscillation due to seiche motion, using linear regression. The results, shown in figure 6.11, suggest a relatively large value of turbulent diffusion given the small size of the lake.

It is worth noticing that in the deep part the eddy coefficient remains small due to the establishment of "monimolimnion" layer.

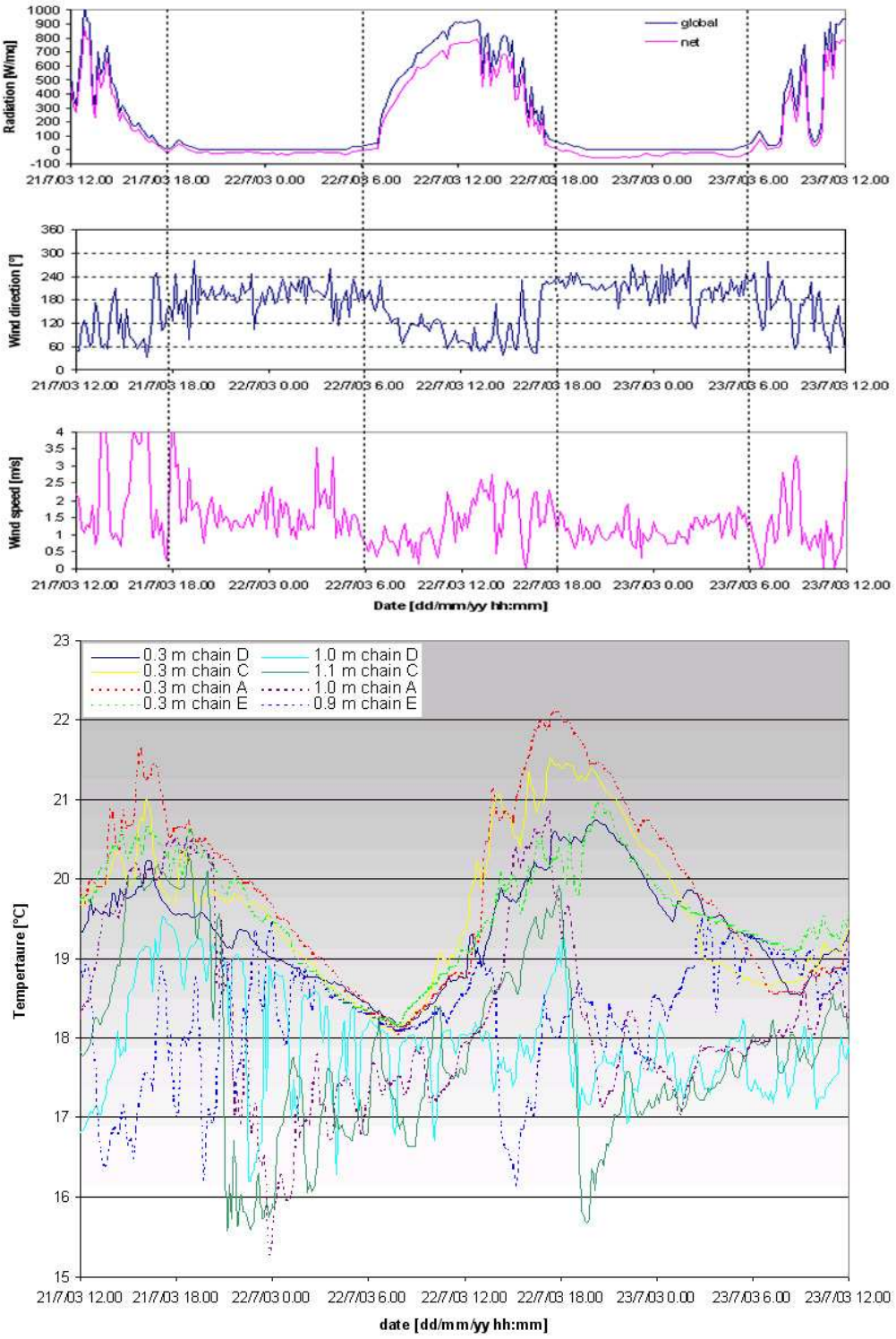

Figure 6.9.: Radiation, wind direction and intensity, and water temperature measured at the surface and 1 m below from July 21st to July 23rd 2003.

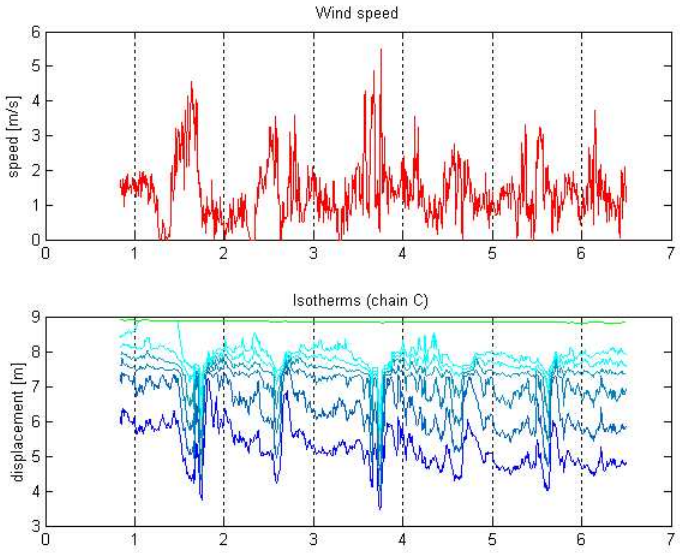

Figure 6.10.: Isotherms pattern for chain D July 18th to 25th and corresponding wind forcing.

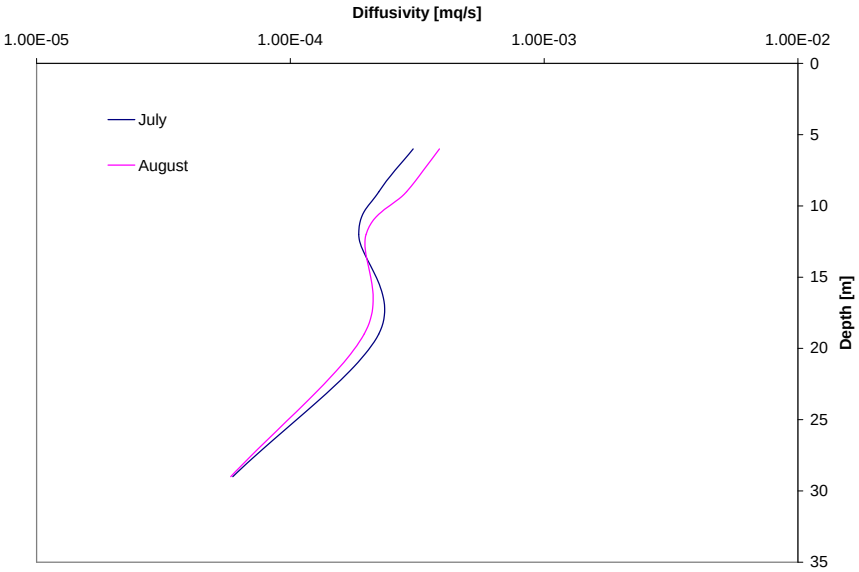

Figure 6.11.: Eddy diffusivity coefficient versus depth.

6.2. Velocity field

6.2.1. ADCP and ADV summer data

From the first two sets of data it is possible to obtain a clear picture of circulation at site 1, located 20 m offshore the cost West in the gulf joining the Red Bay to the Centre Lake. This place can be considered as rapresentative of the region of interaction between the bay and the main lake, which may play a crucial role in determining the transfer of tracers to the bay.

The most apparent characteristic of these data sets is the repetitive behaviour: the similar structure repeats nearly every day.

Data clearly show a diurnal phenomenon of velocity inversion, which in turn doesn't seem to be accompanied by evident changes of magnitude.

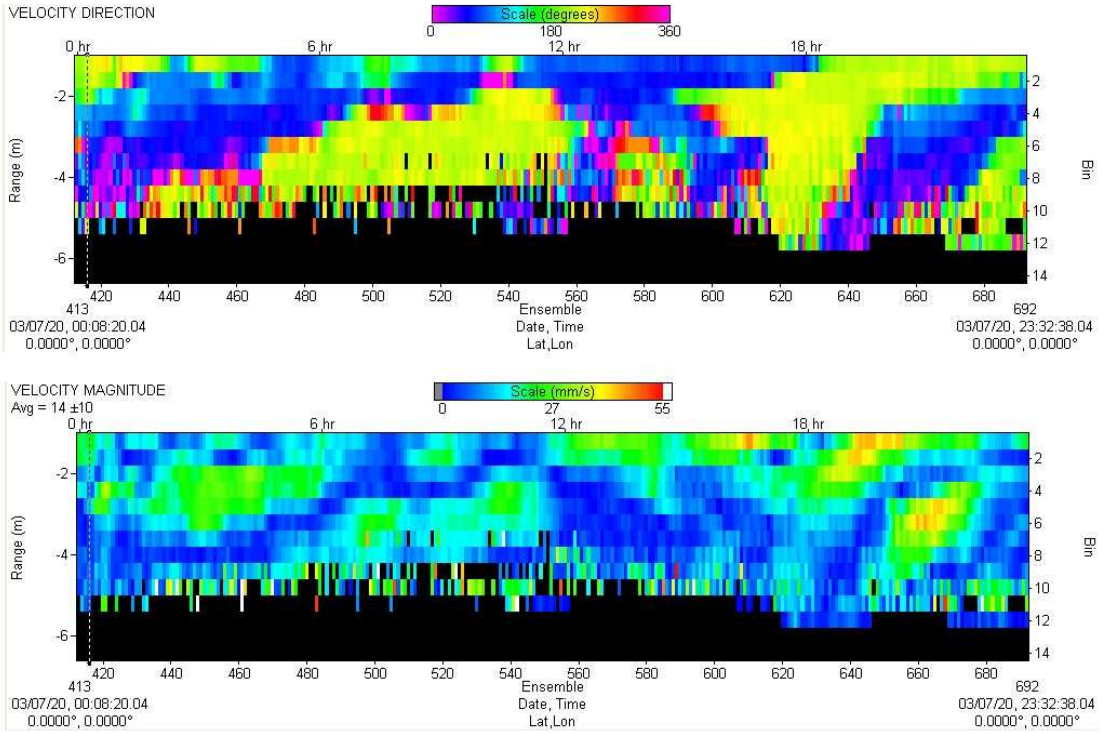

Figure 6.12.: Velocity direction and magnitude in a typical day with stratified conditions, at site 1.

Surprisingly enough, during the night the first layer measured moves in direction SW,

opposite to the wind that blows toward NE. This fact can be due to the particular temperature profile observed in the lake, whereby the surface mixed layer is so thin to force the circulation to invert its direction close to the surface (maybe in the first meter).

Below there is a zone were flow goes in NE direction, while near the bottom another inversion occurs that reflects another circulation possibly induced by the superficial flow. However, the situation is quite complex and seems originated from the bottom.

During the day, when the wind changes direction, also the currents change their direction.

Let us consider three days, for example July 11th, 12th and 13th; they display a similar behaviour. The weather is sunny and windy on July 11th and 13th, while during the July 12th there is a small precipitation.

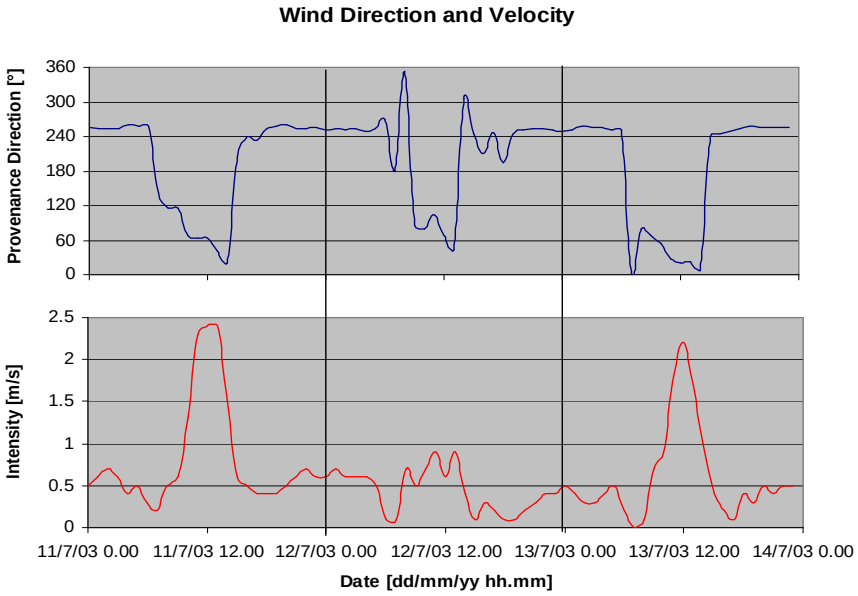

Figure 6.13.: Wind data of July 11th, 12th and 13th 2003.

The observed velocity profiles are summarized in figure 6.14.

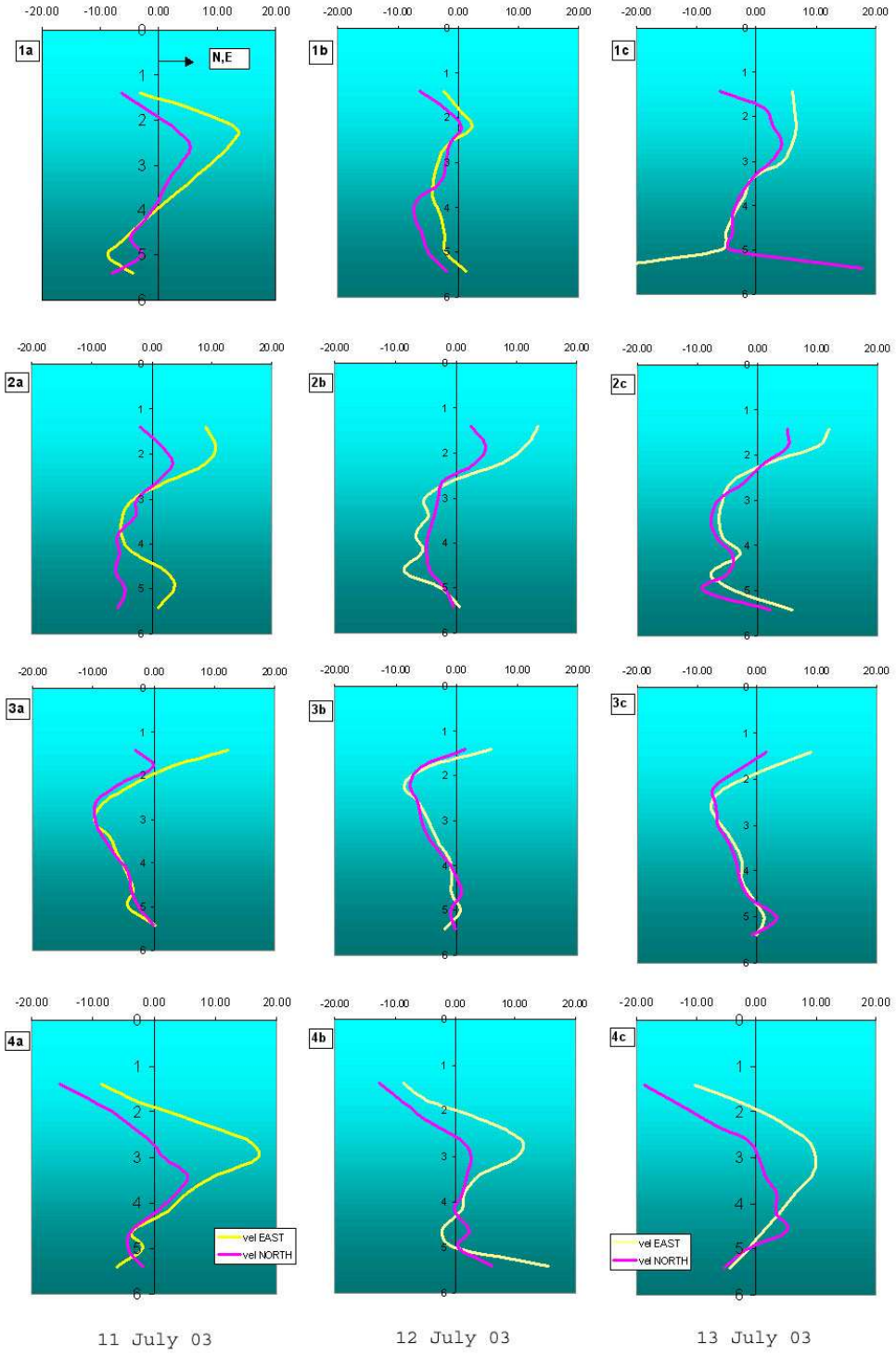

Figure 6.14.: Vertical velocity profiles [mm/s] for 4 different periods during the day: 11(a), 12(b), 13(c) July; [1= night 0-6 ; 2= morning 7-12; 3= afternoon 13-18; 4= evening 19-24 hours]

The measured circulation appears exactly the same during the afternoon of these days, being similar during the others period of the day.

In particular a layer can be identified between 1 and 2 m of depth where the flow moves in direction NE-E (unlike the wind direction) and reaches an intensity greater than 10mm/s (figure 6.14 2a, 2b, 2c) during the morning and the afternoon, while during the evening and night the flow inverts its direction and reaches 20 mm/s toward S in the late evening (figure 6.14 4a, 4b, 4c).

An opposite behaviour is observed in the layer below between 2 m and 4 m of depth.

It is worth noticing that the different peaks of wind intensity observed during the day doesn't seem to influence the velocity field, except in the evening, when this zone displays higher velocities (figure 6.14 4a, 4c).

Measurements seem to suggest that another flow inversion may occur below the depth of 4 m, though the ADCP instrument is unable to provide reliable data due to high echo. The temperature profile measured in these days is reported in 6.15:

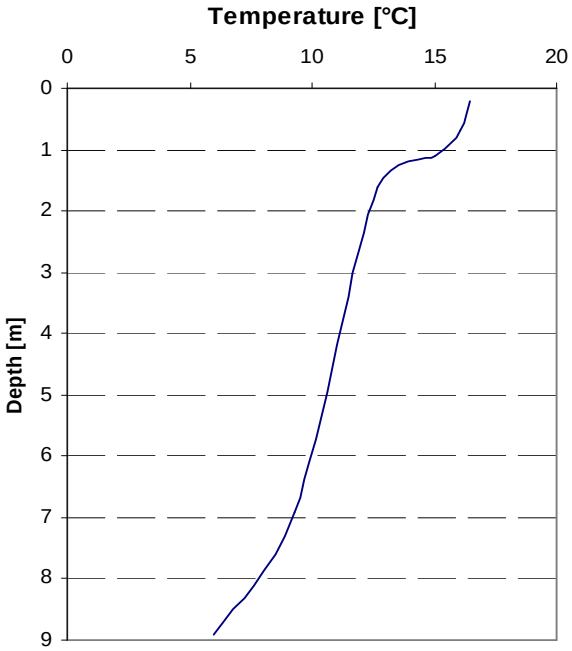

Figure 6.15.: Temperature profile measured with chain C (near ADCP position) on July 11th.

The quite low thickness of the mixed surface layer could explain the relatively fast

inversion of the surface flows observed in the layer between 1 and 2 m of depth.

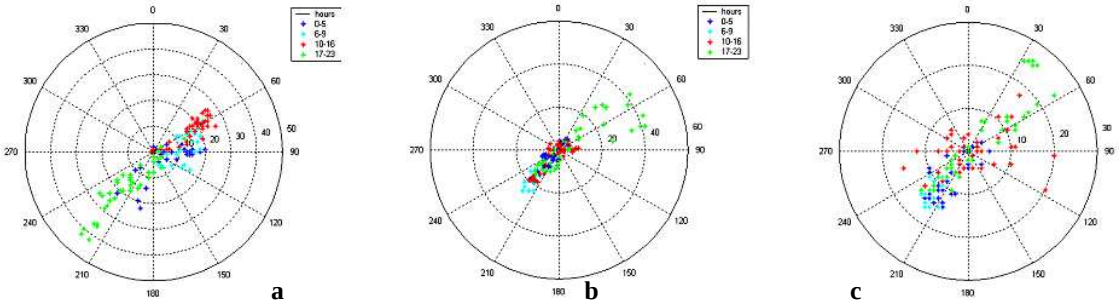

Figure 6.16.: Velocity measured with ADCP at site 1 on July 20th at different depths: a) 1.81 m ; b) 3.41 m; c) 4.21 m.

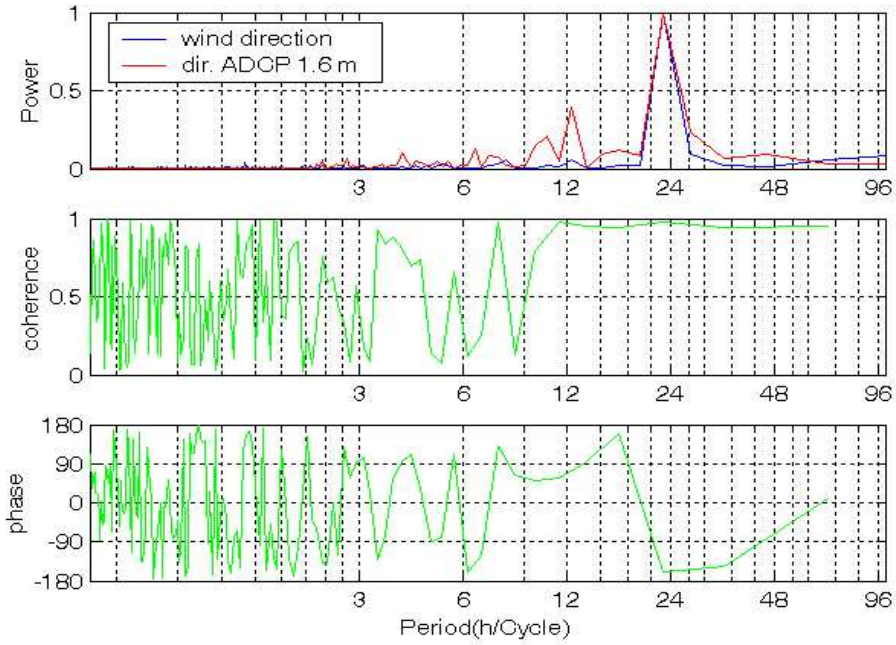

Figure 6.17.: Power, coherence and phase spectra of wind and current direction: measurements collected with chain C at a depth of 1.6 m from July 18th to July 25th.

Measurements performed at the same site indicate that the dominant direction is along the main axis of the lake: in fact, points representing the velocity direction fall on the axis

60°-240°, as shown in figure 6.16. Differences with respect to the above direction rarely exceed 30°, with the exception of some data referring to large depth. In the late evening velocities are greater (green points) and reach peak values of 40 mm/s at a depth of 2 m below the surface, while slightly smaller value (30mm/s) are observed near the bottom. The inversion of direction occurs between 2 and 3 m of depth; it is interesting to note that the velocity attains its maximum values at the same time, though in opposite directions at different depths. During the afternoon (red points) velocity seems to follow a NE-E direction near the surface, while at the bottom data scattering doesn't allow to determine flow direction. Finally, during the night and the morning (blue and cyan points) velocity is directed toward Red Bay near the bottom and in the opposite direction at the surface.

In the same period the flow at 1.6 m moves "countercurrent", as confirmed by spectra analysis. Wind and currents exhibit peak values roughly at 24 and 12 hours, while other periodicities can be identified from ADCP measurements. 24 hours peak is clearly in phase opposition, while 12 hours peak is 90° out of phase.

Near the bottom, currents display peak values with largest intensity corresponding to the 12 hours period, while the 24 hours peak is in phase with wind direction (figure 6.18).

The spectral analysis, whose results are summarized in figures 6.18 and 6.17 indicates the occurrence in the lake of events with different periodicity with respect to the wind forcing.

Repeating the same analysis for isotherms and current we may note the development of several movements with period ranging between 3 and 24 hours. The low value of coherence exhibited by peaks ranging from 8 to 12 hours results from the superimposition of different causes, like the heating and cooling processes, while the coherence is higher for peaks corresponding to 24, 7, 6.7, 5.5, 4, 3.5 hours. In these cases the observed events are often 90° out of phase; this finding reinforces the idea that these movements are related to internal seiches. In fact, when the displacement of the internal wave is maximum, the velocity is changing direction, while when the velocity reaches its maximum, the isopycnal surface is roughly at its equilibrium position.

The behaviour displayed by currents developing at the depth of 1.6 m, along with the corresponding isotherm, (figure 6.19) is similar to the one measured in the deeper part at the same site (figure 6.20). Once again the phase is opposite in the two zones, indicating the occurrence of velocity inversion between the upper and lower layer.

On the other shore of the lake, in the Eastern part, data has been collected with the ADCP at the end of July.

In this case the greatest velocities are measured during the afternoon: for the first 2.5

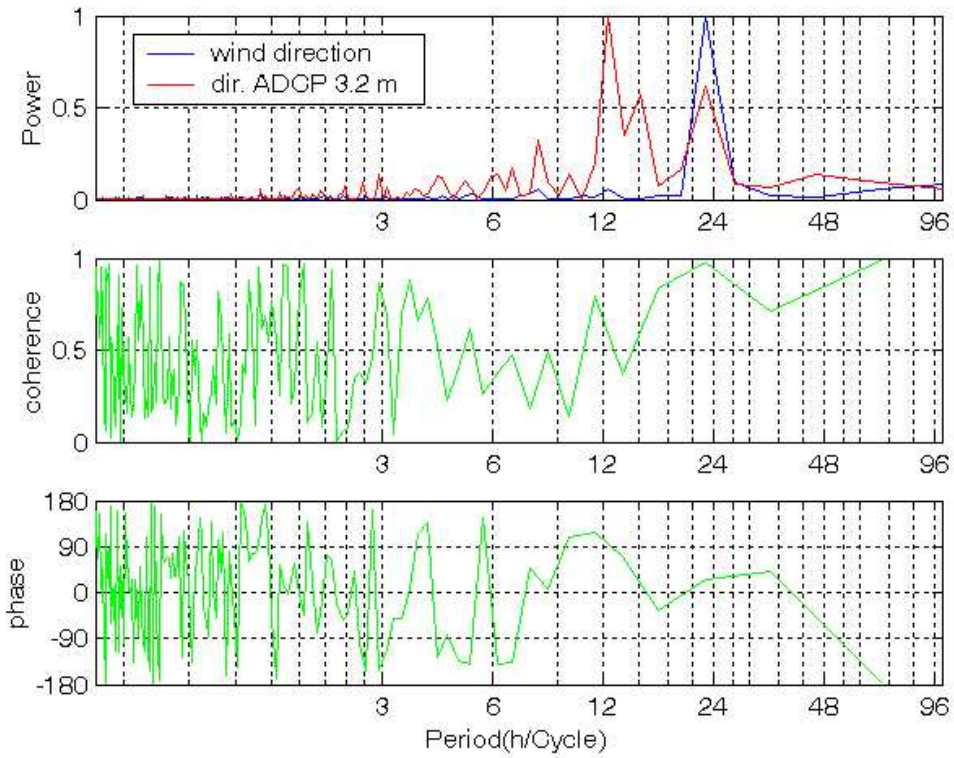

Figure 6.18.: Power, coherence and phase spectra of wind and current direction: measurements collected through ADCP at a depth of 3.2 m from July 18th to July 25th.

m of depth the current seems to leave from the Red Bay (see figure 6.21 a and b); only in the evening, nearly at 2 m of depth, it is possible to distinguish a weak motion toward SW direction. The vertical velocity profile doesn't exhibit any flow reversal at this site.

At the bottom measured data seem to be random distributed and in any case the velocity is very small.

At the end of August the ADV has been placed within the main underflow channel within the Red Bay, measurements confirm the occurrence of a flow with constant direction (25°), relatively high (up to 14 cm/s) and constant intensity during the night (see figure 6.22). In this case the data collected through the ADCP 1m above are comparable and display a small direction shifting and a slightly different intensity: the current seems to flow faster during the afternoon and slower in the evening. Moreover, since the flow is channellised at the bottom, the speed measured through the ADCP is in any case lower with respect to

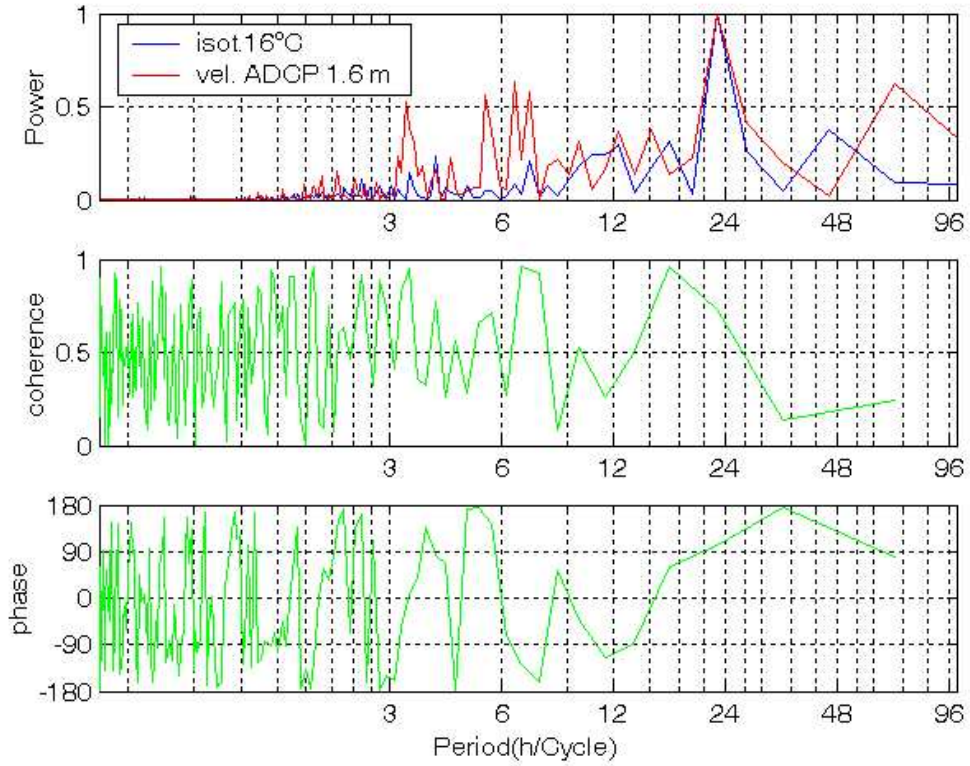

Figure 6.19.: Power, coherence and phase spectra of the 16°C isotherm and velocity: measurements collected with chain C and ADCP at a depth of 1.6 m of depth.

that measured through the ADV.

6.2.2. Velocity data in the cooling period

A week after the above measurements, namely in the second week of September, an abnormal night circulation has been detected through ADV measurements performed along the shore. Figure 6.23 shows the occurrence of a new circulation that develops from midnight to 9:00 in the morning (blue and cyan points), which displays a different direction with respect to the main direction followed by diurnal regular circulations (axis 40°-220°). Notice that in these days a strong cooling occurs and the temperature in the lake becomes rather uniform for roughly 10m below the water surface. The observed circulation is probably due to differential cooling, related to the different thermal inertia of shallow and deep parts: this phenomenon is well-known in the literature and typically develops when the

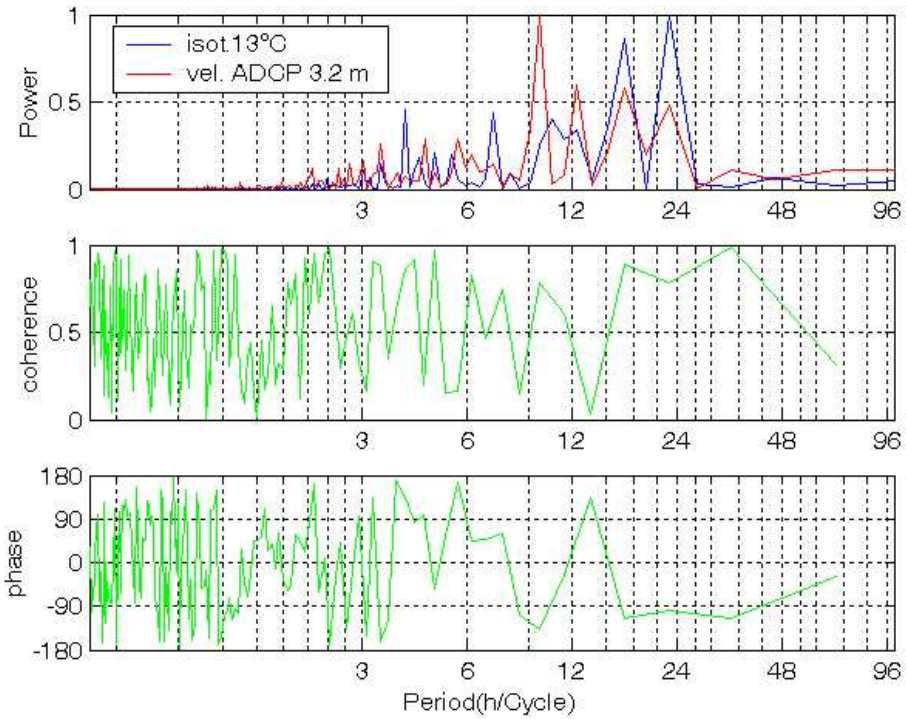

Figure 6.20.: Power, coherence and phase spectra of the 13°C isotherm and velocity: measurements collected with chain C and ADCP at a depth of 3.2 m.

heat fluxes outgoing from the lake surface are sufficiently strong to let the establishment of such a configuration.

Unfortunately, reliable radiation and heat fluxes data are not available for this period; hence, we can only try to provide an explanation comparing the air temperature above the surface and the water temperature. The above comparison, reported in figure 6.24, suggests that the sensible heat, which depends on temperature gradient, is greater during the nights of September 5th and 7th, when this abnormal bottom current develops.

The period of cooling continues from September until the ice formation on the superficial layer, in November.

In October, the ADCP measures realtively high values of vertical velocity while in Summer vertical velocities never reach 1 mm/s: during period of significant heat loss events, a speed greater than 5 mm/s can occur, originating a set of alternate vertical flow directions. These movements are caused by downward plumes of cold heavy water, originated by heat superficial loss, which for a short time span lay under instable equilibrium above slightly

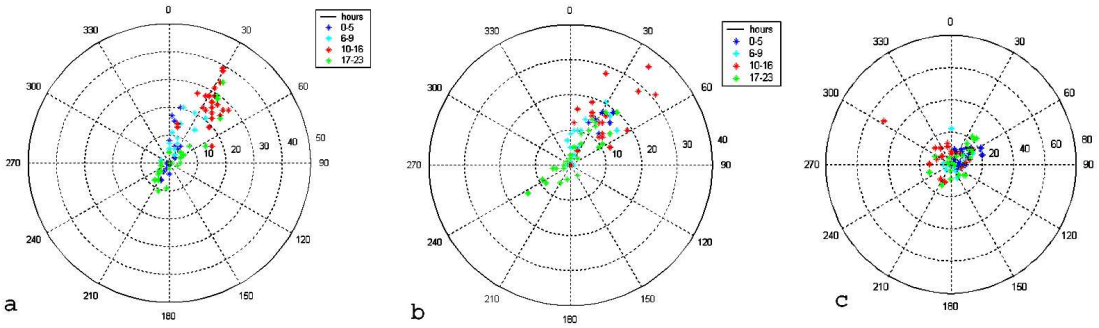

Figure 6.21.: Velocity measured at site 2, on July 30th through the ADCP at different depths: a) 1.51 m ; b) 2.25 m; c) 3.20 m.

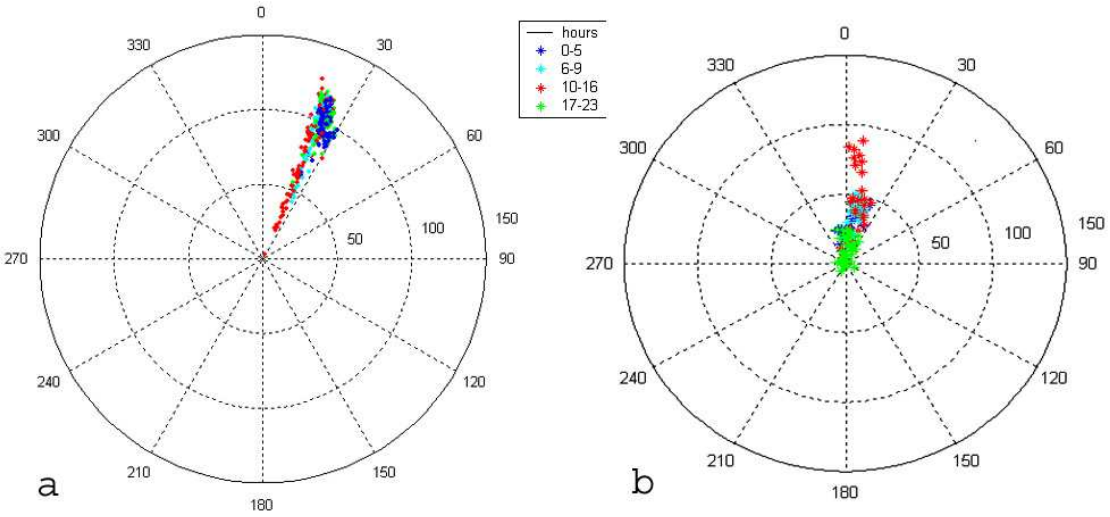

Figure 6.22.: Velocity field measured at the bottom at site 2 by the ADV (a) and the ADCP (b) 1 m above the main underwater channel.

warmer water. Generally the plumes fall down generally during the night, when the heat fluxes outgoing from lake are greatest.

Figure 6.25 shows that downward plumes exhibit higher velocities than upward plumes, as found in other field observations (Tobias et al., 2002).

The enhancement of the phenomenon occurring during the night and at midday of October 8th is related to a short rainy event and an abnormal wind speed, up to 2 m/s, with respect to the calm weather of the other days.

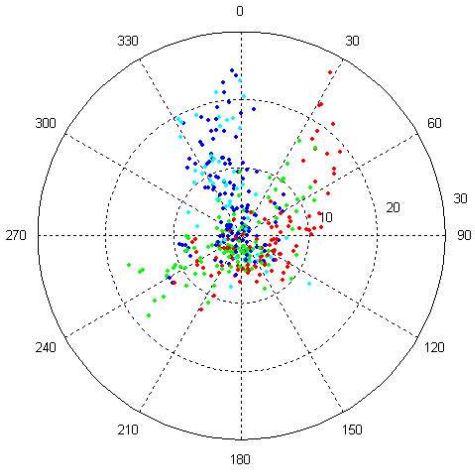

Figure 6.23.: Velocity measured by ADV along the Eastern shore during the second week of September.

The distribution of vertical velocity is asymmetric, as shown in the histogram of figure 6.26 a) in the superficial layer as well as in deeper zones. The mean value of upward velocity is 1.1÷1.15 mm/s while, in downward direction a greater value is observed, ranging about 1.7÷1.8 mm/s. Moreover, figure 6.26 b) displays decreasing values of plumes velocity as the depth increases.

The vertical convective plume velocity can be estimated through the following theorical formula:

$$w = \sqrt[1/3]{\frac{\alpha g h H}{c_p \rho}},$$

where

$$\begin{aligned} \alpha &= 2.57{\cdot}10^{-4\circ}C^{-1} \\ g &= 9.8\mathrm{m/s}^2 \\ h &= 6\mathrm{m} \\ H &= \text{-}170\ \mathrm{W/m}^2 \\ \mathrm{c}_p &= 4179\ \mathrm{J\ Kg}^{-1\circ}C^{-1} \\ \rho &= 998\ \mathrm{kg/m}^3 \end{aligned}$$

we obtain a maximum theoretical value equal to $w = 8mm/s$.

During the cooling period the ADCP measures a current directed to N E at the bottom,

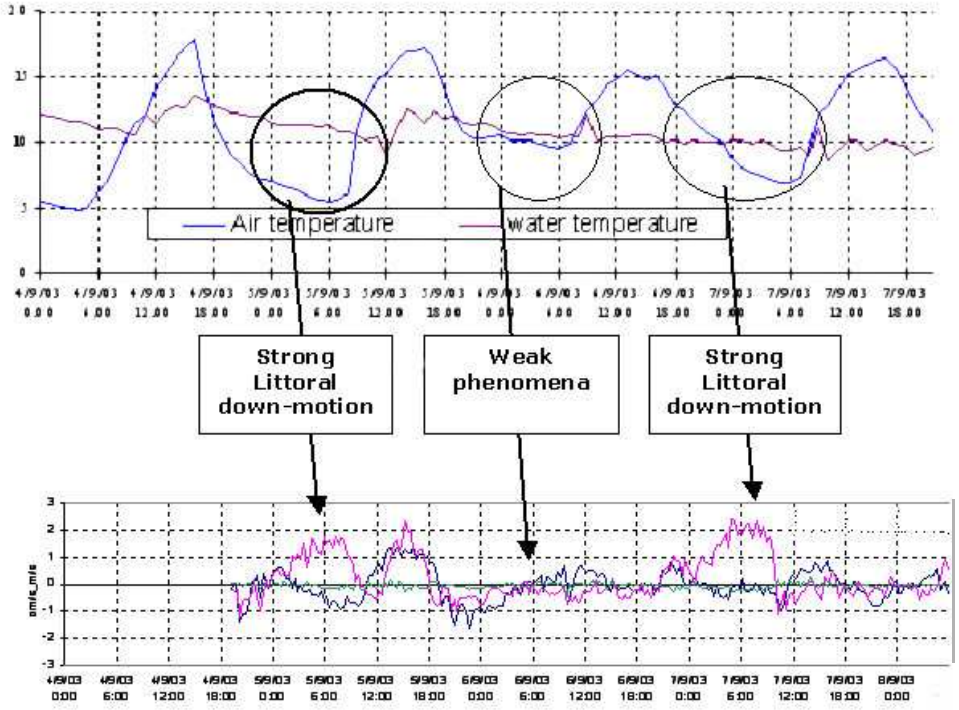

Figure 6.24.: Development of currents at the bottom of the Eastern slope and temperature behaviour from September 4th to September 8th.

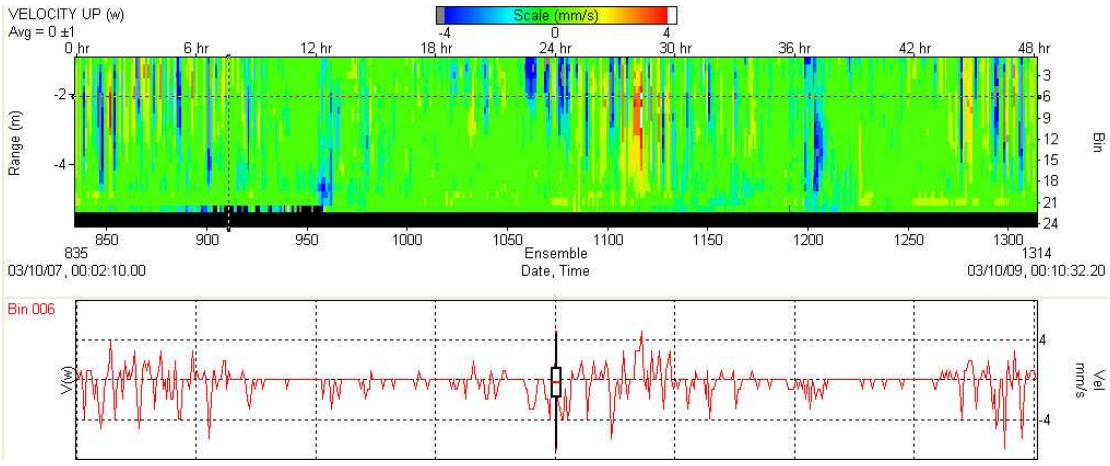

Figure 6.25.: Vertical velocity component measured by the ADCP on the full depth range and at a depth of 2 m from October 7th to October 9th.

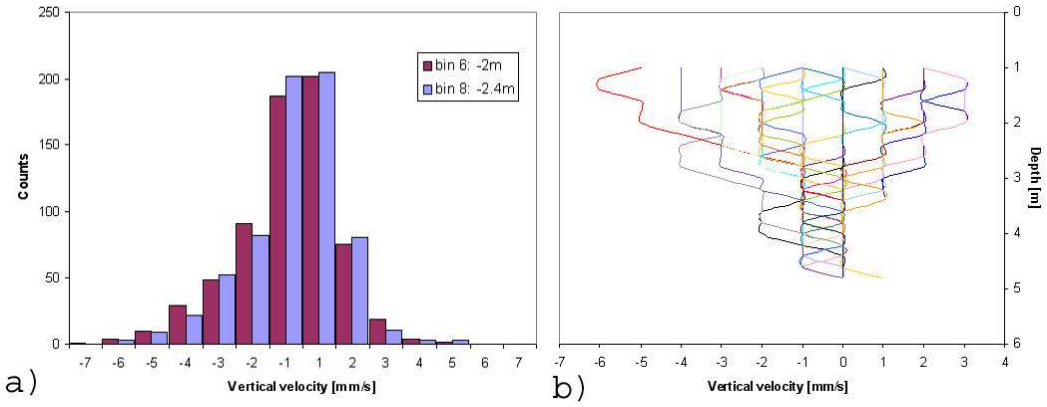

Figure 6.26.: Vertical velocity: a) distribution at the bin 6 and 8, corresponding to depth of 2 m and 2.4 m; b) vertical profiles representative of the core of convective plumes.

as also confirmed by the ADV positioned at the same location (site 1) in October.

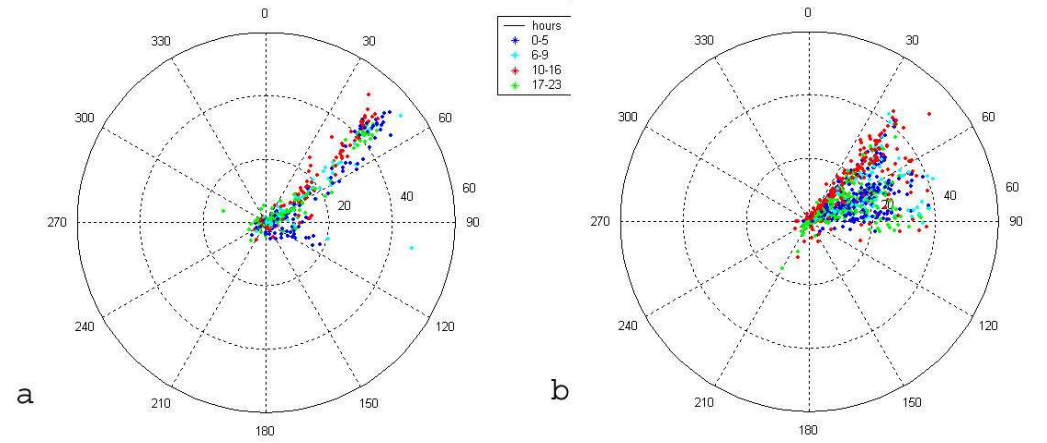

Figure 6.27.: Velocity field measured by the ADV at the beginning (a) and the end (b) of October.

The main flow direction is 60°; as the Autumn goes on the intensity of current decreases and the measure of direction exhibits a certain scatter (see figure 6.27). The flow doesn't seem to be influenced by the period of the day.

This current, which involves the entire lake, is probably a gravity adjustement due to differential cooling, which is stronger in the Bay than in Centre Lake.

In fact, the Littoral Current Number, based on the observations performed in October,

exhibits values always lower than the critical threshold 1, which implies that gravitational currents can occur (figure 6.28).

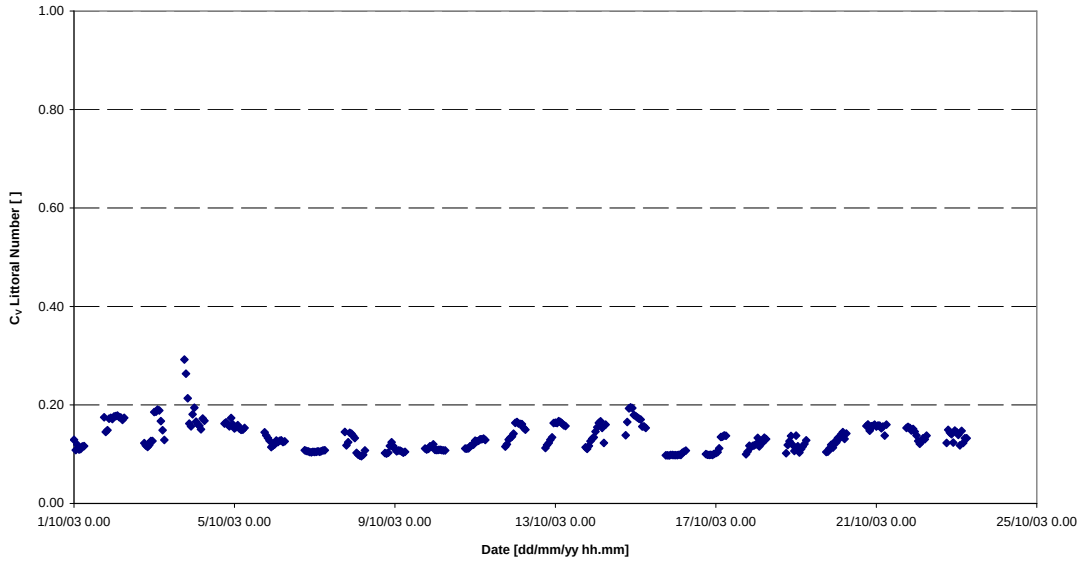

Figure 6.28.: The Littoral Number based on the observations performed in October, 2003

The velocity of this baroclinic current can be deduced equating the value of the potential energy losses and the kinetic energy gains of the mass flow (Roget and Colomer, 1996):

$$u = \sqrt{2\alpha\ \Delta T\ gh},$$

where ΔT is the difference of temperature between the two lobes and h is the vertical distance between the centre of mass of the cold part and the depth where the current has been measured.

The comparison between estimated and measured values of the velocity of gravity currents is reported in figure 6.29.

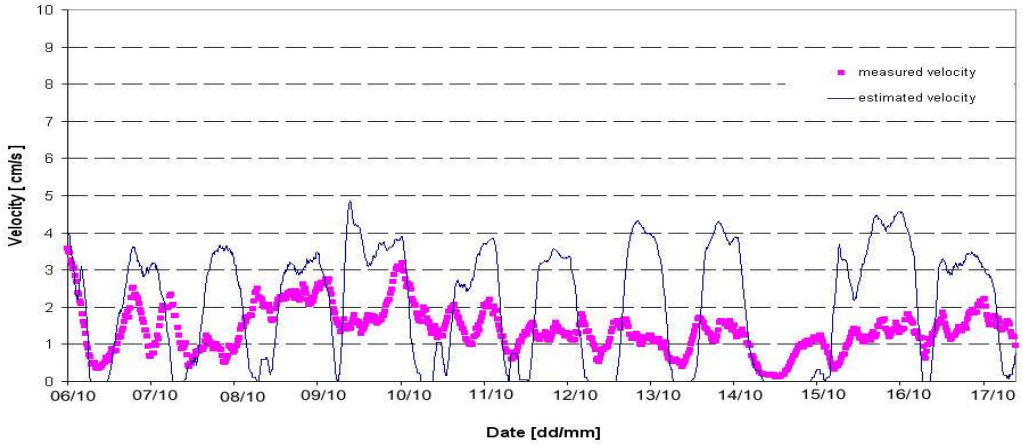

Figure 6.29.: Comparison between measured and estimated values of velocity of the gravity current at the neck between gulf and main basin.

6.3. Drifter data cluster analysis

The drifters are used to characterize the superficial circulations that develop in the lake. It's clear that during the day, with a certain lag, waters in the SW part, from the so-called "joining slope" zone are driven by currents toward Red Bay, unlike waters in the main part that never reach the SW zone and are called back from wind inversion and local vorticity.

In this analysis we mainly concentrate our attention on experiment A and, in particular, we focus on the growth and deformation of the surface of the horizontal convex hull (the smallest convex polygon) formed by drifters.

Dispersion coefficients can be estimated once two-dimensional standard deviations of the drifter's distribution are computed.

In fact, horizontal velocities of a drifter j can be expressed by a Taylor expansion with respect to the velocity and position of the centroid, at any time step t, in the following form:

$$u_j^t = \overline{u^t} + \frac{\partial \overline{u^t}}{\partial x}\left(x_j^t - \overline{x^t}\right) + \frac{\partial \overline{u^t}}{\partial y}\left(y_j^t - \overline{y^t}\right) + \frac{\partial \overline{u^t}}{\partial z}\left(z_j^t - \overline{z^t}\right) + R_1, \tag{6.3}$$

$$v_j^t = \overline{v^t} + \frac{\partial \overline{v^t}}{\partial x}\left(x_j^t - \overline{x^t}\right) + \frac{\partial \overline{v^t}}{\partial y}\left(y_j^t - \overline{y^t}\right) + \frac{\partial \overline{v^t}}{\partial z}\left(z_j^t - \overline{z^t}\right) + R_2,$$

where R are the residual velocities due to truncation error and $\left[\overline{x^t}, \overline{y^t}, \overline{z^t}\right]$ denote the average values of drifter's positions.

The standard deviations of drifter's displacements read:

$$\left[\sigma_x^2 \;;\; \sigma_y^2\right] = \frac{1}{n-1}\left[\sum_{j=1}^{n}\left(x_j^t - \overline{x^t}\right)^2 \quad ; \quad \sum_{j=1}^{n}\left(y_j^t - \overline{y^t}\right)^2\right], \tag{6.4}$$

while the velocity gradients, conveniently combined, provide differential kinematic properties, namely:

$$\begin{aligned}
\zeta &= \frac{\partial \overline{v^t}}{\partial x} - \frac{\partial \overline{u^t}}{\partial y} && \text{vorticity,} \\
\delta &= \frac{\partial \overline{u^t}}{\partial x} + \frac{\partial \overline{v^t}}{\partial y} && \text{divergence,} \\
a &= \frac{\partial \overline{u^t}}{\partial x} - \frac{\partial \overline{v^t}}{\partial y} && \text{stretching deformation,} \\
b &= \frac{\partial \overline{v^t}}{\partial x} - \frac{\partial \overline{u^t}}{\partial y} && \text{shearing deformation,}
\end{aligned} \tag{6.5}$$

The two-dimensional standard deviation takes the following form:

$$\sigma_{xy} = \left(\sigma_x^2 + \sigma_y^2\right)^{\frac{1}{2}}. \tag{6.6}$$

Hence, an overall dispersion coefficient can be defined in the following form:

$$k_{xy} = \frac{1}{2}\frac{d\sigma_{xy}^2}{dt}. \tag{6.7}$$

The resulting average value of K_{xy} is fairly small, as shown in 6.30. In fact, the analysis of the kinematic properties of the hull shows that the divergence is positive (on the average), but the vorticity is dominant. Notice that indicator of the relative importance of the vorticity with respect to the strain field (stretching and shearing deformations) is the kinematical vorticity number, defined by Truesdell, as:

$$T_k = \left[\frac{\zeta^2}{a^2 + b^2}\right]^{\frac{1}{2}}. \tag{6.8}$$

When $T_k > 1$ the vorticity field is stronger than the strain field and eddy structures are present. In this case the dispersion is low because the growth of the cloud is due to vorticity

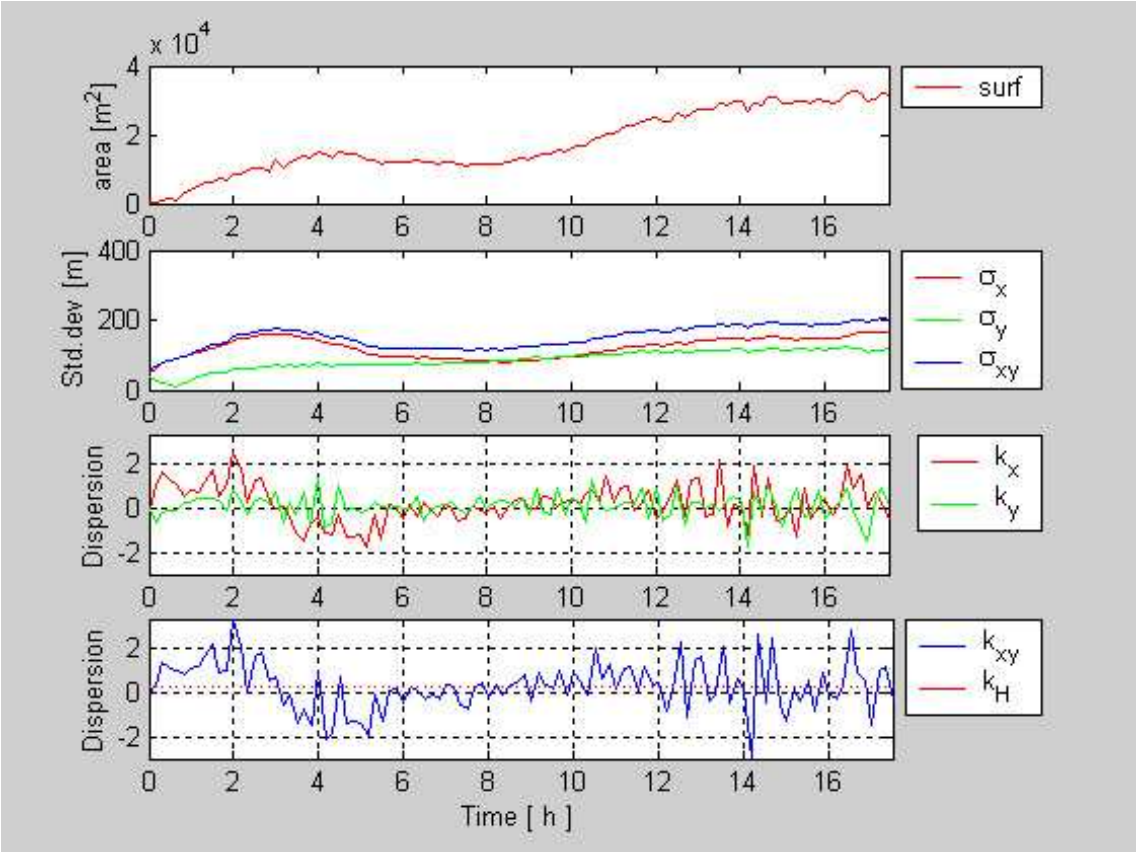

Figure 6.30.: Area, standard deviations and dispersion coefficients of the convex hull.

and not to the divergence of strain field. Estimated values from experiments performed with Lagrangian drifter in Tovel lake are reported in 6.31.

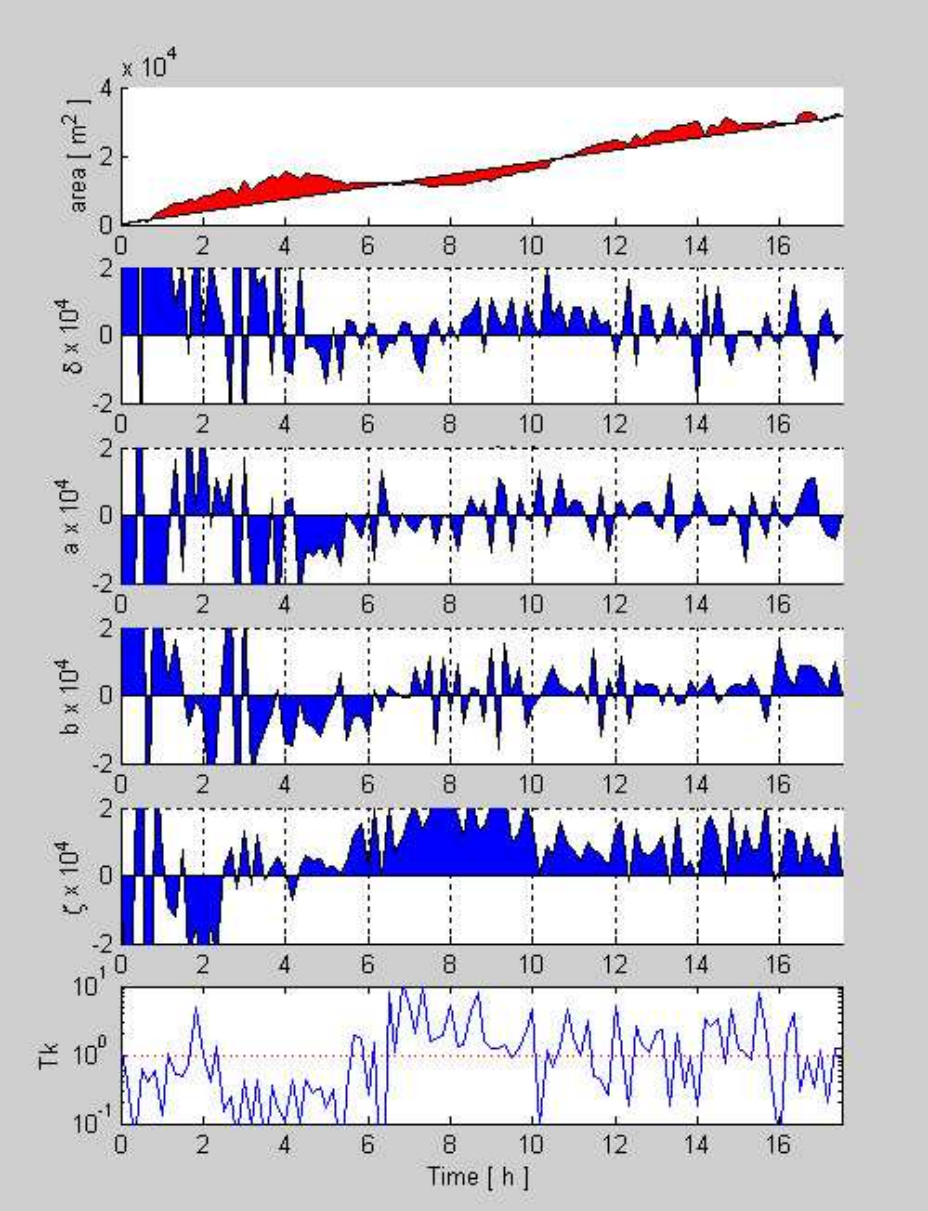

Figure 6.31.: Lagrangian drifters: area growth, differential kinematic properties and Truesdell number.

Part III.

Numerical Modelling

The aim of this section is that of ascertaining the suitability of numerical models to replicate observed phenomena. Since different phenomena require different numerical approaches, results of two models are discussed herein.

The long term thermodynamic behaviour of the lake is simulated using a well-known one-dimensional commercial model developed by the Centre for Water Researches (CWR) Australia, while the hydrodynamics is simulated through a three-dimensional model which has been developed within the framework of the present research.

Testing the results of numerical models against measured data is very important since field data are often not available; furthermore, field data are quite expensive, time consuming and cannot cover the full range of physical conditions.

7. Models

Modelling the physical processes is an obliged path to understand the biological phenomena occurring in lakes and to support management decisions: in fact assimilative capacity can be modified by load distribution, resuspension and transport effects on the biogeochemical cycle (Hodges et al., 2000).

Generally, transport processes are three-dimensional and are driven by a set of crossed interactions of wind, surface thermodynamics, topography and thermal seasonal history of the lake.

7.1. Criteria for model selection

Transport and water quality in lakes can be often affected by the peculiar behaviour of different regions or zones. Usually these zones are neither distinct nor continuous along the shoreline of the entire lake basin. The relative distribution of these different zones is fundamental for the modeling approach. For example, their presence or absence can affect model dimensionality, process descriptions for mixing, and therefore solution algorithms for water quality simulations.

Important zones are formed often by physical processes. The erosion due to wave action and ice formation often forms a terrace along the shores of lakes and reservoirs, the exposed portion of which is the beach. The Littoral zone, which lies between the beach and open waters, encompasses the region that may be exposed between high and low waters (the eulittoral region) as well as that relatively shallow, constantly inundated region in which aquatic vegetation may grow. Beyond the littoral zone, the exposed sediments free of vegetation make up the deep zone. The extent and impact of the littoral zone varies widely. In many small and shallow lakes and reservoirs the littoral zone represents a large fraction of their surface areas. Steep-sided lakes, like those formed in caldera or reservoirs created in steep valleys, may have no littoral zone. Littoral currents are usually parallel to the shoreline and strongly influenced by the shoreline shape (Martin and McCutcheon, 1999).

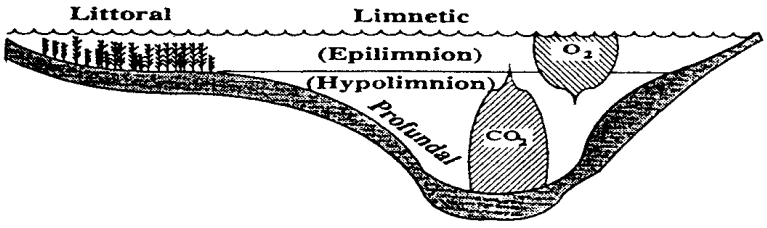

Figure 7.1.: Schematic view of main zones of a lake.

The shallow depth and wind mixing cause complete vertical mixing of the littoral zones. The littoral zone often provides essential habitat for several kinds of fishes. The open water portion of lakes, or Limnetic zone, is usually deeper than the maximum depth in which emergent vegetation can grow and displays different mixing and water quality connected to the greater depths. Light does not penetrate to the bottom of most limnetic zones.

In the zone through which light penetrates (the euphotic zone), the combination of internal production and surface gas exchange may maintain oxic conditions. In the aphotic zone, degradation processes dominate, resulting in oxygen depletion and production of reduced materials.

7.2. Models and balances

Any model, regardless its complexity, can be schematized essentially in two fundamental components:

- the water balance (mass, momentum)
- the mass balance (nutrients, pollutants..)

In any case a first level of understanding can be achieved through overall balances, which may disclose the main dynamics involved. The continuity equation can be expressed by:

$$\frac{dS}{dt} = \sum I - \sum O + (P - E)\ A_s\ \pm G, \tag{7.1}$$

where $\frac{dS}{dt}$ is the time variation of storage, I is the inflow rate, O is the outflow rate, P is the precipitation, E is the evaporation, A_s is the surface area and G the groundwater infiltration.

Along with (7.1), zero-dimensional models for water quality solve the mass conservation equation:

$$\frac{dM}{dt} = \frac{d(VC)}{dt} = \sum (C_I Q_I) - \sum (C_O Q_O) \pm \sum S \pm \sum R, \tag{7.2}$$

where M is the mass of a constituent, C is its concentration in the volume V, Q is the flow rate, S is the external supply and R represents internal reactions.

One-dimensional models can be applied in vertical or in longitudinal direction: the latter approach is generally employed to investigate run-of-the-river reservoirs while in lake water quality analysis and management 1-D vertically layered models are more common. In fact, the fairly large difference between vertical and horizontal transport and diffusion allows one to consider homogeneous horizontal properties with respect to vertical gradients.

Two-dimensional models comprise laterally and vertically averaged models.

Laterally averaged 2-D models simulate water quality in long and deep basins; these models are based on the solution of longitudinal and vertical momentum and continuity equations: quantities are averaged over the width.

When the lake is shallow and wide a vertically averaged model is preferable: in this case the vertical stratification is neglected and the effect of vertical velocity profile is not accounted for. Hence, the model only describes horizontal variations of variables and assumes that the mixing process along the water column is relatively fast compared with horizontal mixing.

Three-dimensional models enable one to compute velocity field and transport in all parts of the lake and can provide a better resolution of topographical effects, internal waves, mixing and spatial gradients lake properties.

Unfortunately, numerical models applied to fixed grids are influenced by numerical diffusion, in particular near the thermocline zones in stratified lakes (Hodges et al., 2000). This effect is negligible for simulations lasting few days or weeks, while is may become significant for longer simulations: in fact, over monthly or seasonal time scales the accumulation of numerical diffusion can change the response of the lake to wind, leading to an overestimate of the transfer of lake properties through different vertical zones, e.g. from epilimnion to metalimnion.

Moreover, several examples are given in the literature of wrong simulations of topographically-driven circulations when a spatially-uniform wind is used (Hodges et al., 2000).

For these reasons, long simulations with 3-D models are heedless; hence, when the seasonal or over-seasonal behaviour is the aim of research, it is better to focus on 1-D vertical models and use 3-D models only to investigate thoroughly the dynamics of currents in

specific situations on short time scale.

7.3. One-dimensional vertical model

During the period of great stratification, temperature is almost homogeneous over an horizontal plane parallel to the water surface.

In fact strong stratification inhibits vertical motions and reduces turbulence: under these conditions only the vertical variations play a significant role in mass, momentum, and energy balances (Imberger and Patterson, 1980).

One-dimensional models can use two completely different approaches.

Mixed layer models

This kind of models is based on the energy balance: in fact, the mixed layer depth is computed, at any time step, through the comparison between the kinetic energy due to external forces and the potential energy contained in a layer of a stratified lake (Martin and McCutcheon, 1999). A total energy balance for multilayered lakes can be written for each layer as:

$$\left(C_T\ q^2 + \alpha \Delta T\ gh\right) \frac{dh}{dt} = C_f\ u_f^3 + C_*\ u_*^3 + C_S\left(\Delta u\right)^2, \tag{7.3}$$

where the first term, which accounts for the rate of change of total kinetic energy q, is often negligible (Martin and McCutcheon, 1999). The following notations are used: $q = \left(\ u_f^3 + \ u_*^3\right)^{\frac{1}{3}}$, α is the thermal coefficient for water expansion ($\alpha = 2.57 \cdot 10^{-4 \circ} C^{-1}$), ΔT is the temperature difference between the upper layer and the given one, g is the gravitational acceleration, C_T , C_f , C_* , C_S are dimensionless efficiency coefficients, h is the thickness of layer, u_f is the free fall velocity of thermal plumes under cooling water surface, u_* is the wind friction velocity and Δu is the velocity gradient between layers.

The second term on the left hand side is the buoyancy term; the terms on the right hand side represent the available energy produced by penetrative convection, the wind (stirring energy) and the advective shear connected to mean velocity structure, respectively. Equating the required energy (first two terms) to the available energy it is possible to understand when the layer has to be mixed and the thickness h changed.

Vertical turbulent diffusion models

These models use the eddy diffusivity approach to quantify vertical transport and mixing. The solution is based on the one-dimensional transport equation in the vertical direction; since vertical velocities are often negligible, the time change of the concentration C can be given the following form:

$$\frac{\partial C}{\partial t} = \frac{1}{A}\frac{\partial}{\partial z}\left(E_z A \frac{\partial C}{\partial z}\right), \tag{7.4}$$

where A is the cross-sectional area of the horizontal plane, which changes as z changes, and E_z is the vertical eddy diffusivity coefficient. In this case the model works on a fixed grid: the main difficulty consists in the estimate of E_z.

7.3.1. Criteria for the correct use of 1D models

In order to establish the range of applicability of one-dimensional models, some criteria have been proposed: the most important rule to discern when it is possible to apply these models is based, for convenience, on several non-dimensional parameters like Froude number, Wedderburn number and Lake number.

The inflow Froude number can be defined as:

$$Fr_i = \frac{U}{\sqrt{g^* H}}, \tag{7.5}$$

where U is the inflow velocity, g* is the modified gravity acceleration $g^* = g\frac{\Delta\rho}{\rho_0}$ with $\Delta\rho$ density difference between the inflow water and the lake water and H is the lake mean depth. The one-dimensional assumption is valid when $Fr_i < 1$: physically, this condition means that the buoyancy force are able to damp any non-vertical motion in the density structure resulting from inflow disturbances.

In similar way the outflow Froude number can be defined as:

$$Fr_i = \frac{Q}{\sqrt{g^*} H^{3/2} L}, \tag{7.6}$$

where Q is the outflow discharge, L is a characteristic planimetric dimension of the basin and g^* is the reduced gravity between the surface and the bottom water. The hypothesis of one-dimensionality is correct when $Fr_o < 1$.

The Wedderburn number W represents the ratio of the buoyancy force acting on the surface layer to the shear stress due to the wind, and is defined as in equation (2.31).

When $W \gg 1$ the buoyancy force is greater than the applied wind stress: in this case only a small tilting of the isopycnal surfaces occurs, horizontal variations are negligible, such that the processes can be considered essentially one-dimensional. When $W \sim 1$ the effect of applied wind stress is comparable with buoyancy forces. This critical condition corresponds physically to the situation at which the base of the surface layer tilts and reaches the free surface at the upwind end (upwelling). When $W \ll 1$ upwelling occurs at the upwind end of the lake, vertical motions occur on smaller time scales and vertical one-dimensional models are not applicable.

The Lake number L_N is an index of the dynamic stability of the water column; it is defined as the ratio of the moments of the stabilizing force of gravity (resulting from the density stratification) and of the destabilizing forces with respect to the water body's centre of volume. If the wind is assumed to be the dominate mixing force, L_N can be defined in the following form (see Chapter 2)

$$L_N = \frac{S_t\,(H - h_t)}{u_*^2\ A_s^{3/2}\ \ (H - h_v)}, \tag{7.7}$$

where H is the maximum depth of the water body, h_t is the seasonal thermocline height from the bottom of the lake, h_v is height of the centre of volume of the lake, A_s is the lake surface area and St is the Schmidt stability index (1.14).

When $L_N \gg 1$ the stratification is strong and dominates the forces introduced by surface wind energy. Hence, isopycnal lines remain nearly horizontal; furthermore a negligible seiching of the seasonal thermocline and small turbulent mixing in the hypolimnion occur. When $\mathrm{L}_N \gg 1$ the stratification is too weak with respect to wind stress; hence, the seasonal thermocline can experience strong seiching and turbulent mixing due to internal shear occurs in the hypolimnion (Imberger, 2001).

Applicability of 1D model to Lake Tovel

With the aim of testing the applicability of a 1D models to lake Tovel the non-dimensional parameters mentioned above have been computed.

The effect of surface inflows and outflows in Lake Tovel is very small and the limited flows are not able to modify the vertical density stratification of the water column. The internal Froude number, computed both for inflows and outflows, attains values which are always much lower than the critical threshold of 1, as shown in figure 7.2.

This results suggest the absence of strong interaction between the water column and external flows, even underground flows, with the exception of specific zones and situations

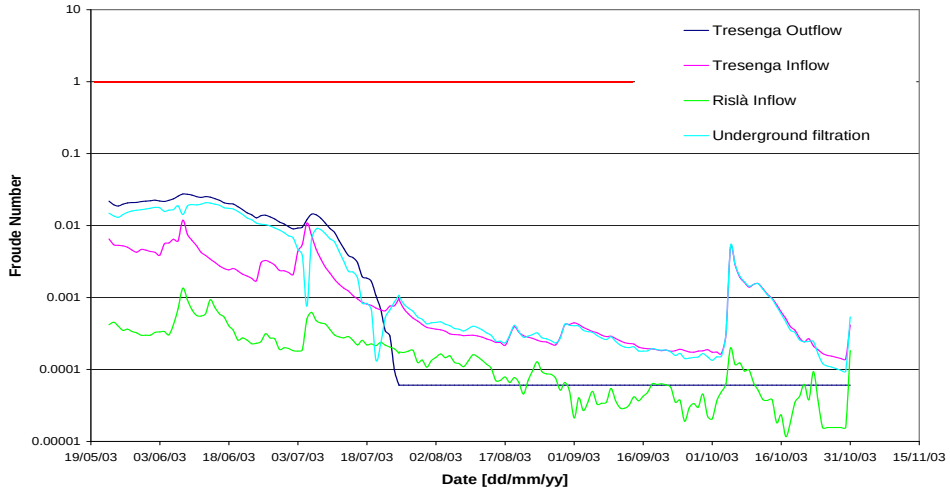

Figure 7.2.: Field estimate of the internal Froude number of lake Tovel.

for which the above criterion cannot be verified (i.e. the Red bay during periods of very shallow water).

Similarly, the Lake number provides information about the absence of hypolimnetic water upwelling, as it might be expected. In fact, winds over lake Tovel surface are very weak and we can suppose that they are unable to tilt the isopycnal deep surfaces. The measured values of Lake number are always greater than 10; this implies that even the cooling of the lake and the corresponding density difference reduction may be not sufficient to lead the destabilizing forces to overcome the stratification.

The above behaviour is also confirmed by temperature data collected by deployed chains. Furthermore it is possible to show that only a wind with 15 ms^{-1} intensity could induce hypolimnetic water intrusion in surface layers.

The Wedderburn number reaches several times values lower than the threshold 1, indicating that the metalimnetic water upwelling can occur easily. This phenomenon is clearly possible because of the extremely thin surface layer due both to the weakness of wind forcing and to spilling out by filtration of superficial warm water.

This process occurs generally in the afternoon (from 12:00 to 16:00), when the wind blowing toward the Red Bay reaches its maximum value and can tilt the isopycnal surface down in downwind position (Red Bay) and up in upwind place (NE part).

In fact, measured data show a temperature increase on one side of the lake which is often accompanied by an abnormal cooling on the other side, as shown in figure 7.5.

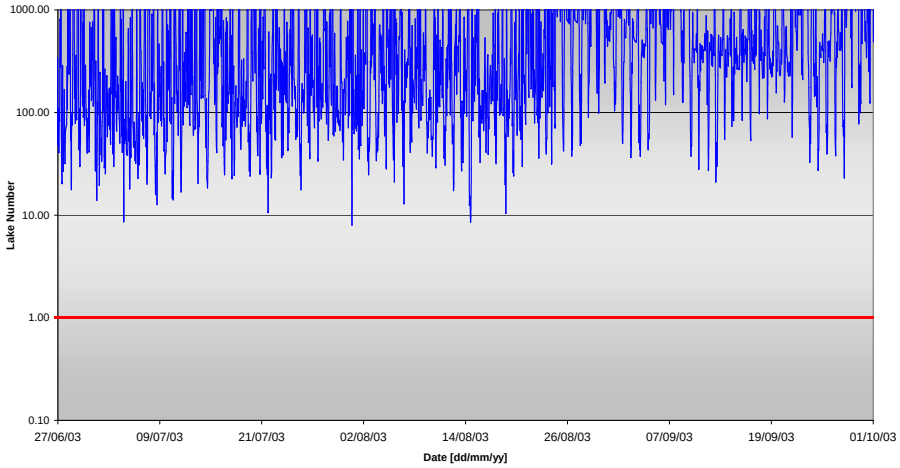

Figure 7.3.: Field estimate of the Lake Number of lake Tovel.

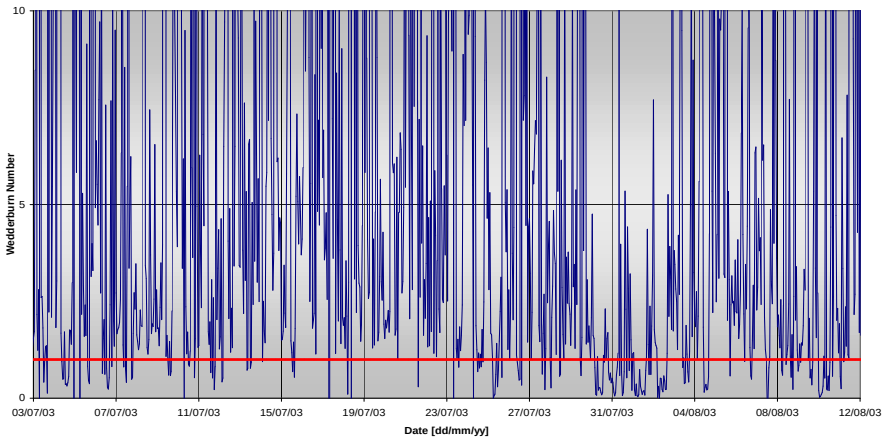

Figure 7.4.: Field estimate of the Wedderburn Number of lake Tovel.

When the wind changes direction and the intensity decreases, a wave starts suddenly and tends to move all isopycnal surfaces towards a new dynamical equilibrium state, with oscillation of small amplitude around a plane roughly horizontal. In the upwind position temperature sensors can measure a sudden heating: this temperature modification can not be driven by radiation changes, but it is connected to warm waters shifted from baroclinic motions, replacing upwelled cold water.

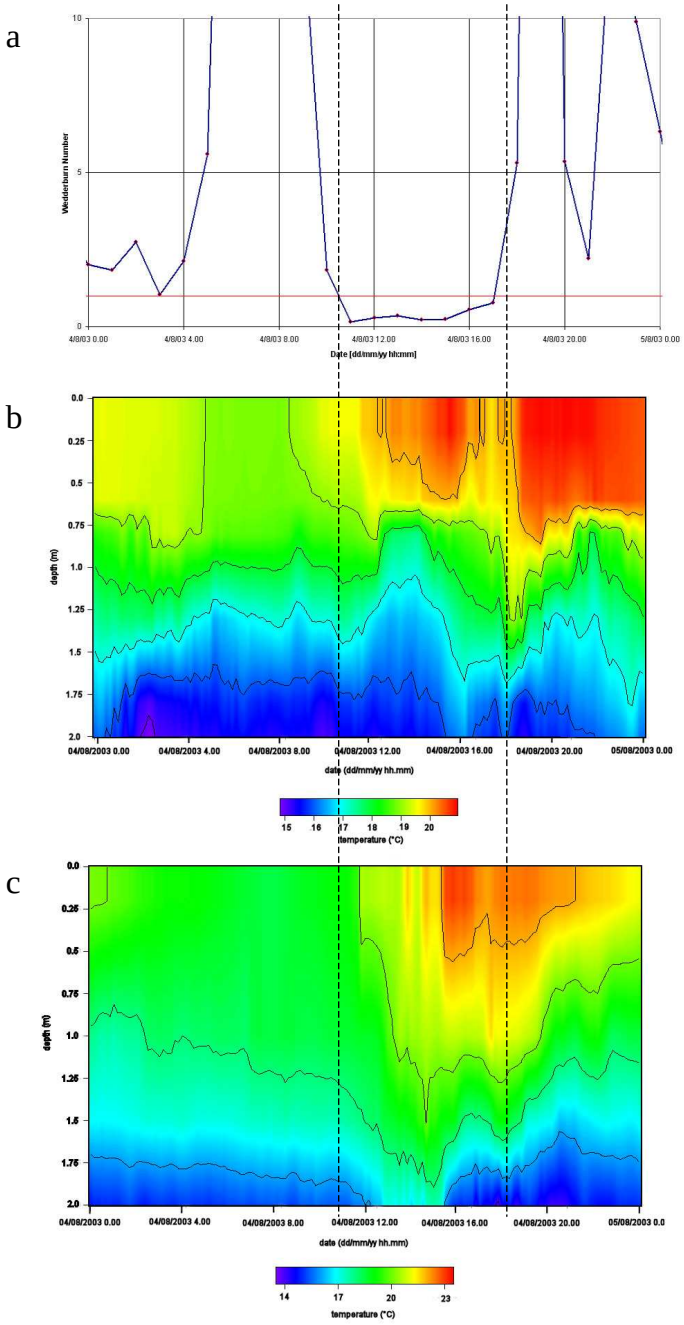

Figure 7.5.: a) Estimated values of Wedderburn Number (August 4th); b) upwelling of metalimnetic water in the Northern part; c) isopycnal surface deepening in Southern part.

8. 1-D Model

8.1. DYRESM model

DYRESM is a Fortran-based model of a support system for lake management, developed in the Centre for Water Research of Western Australia University. It is based on the assumption of one-dimensionality, which means that variations in the lateral directions are small with respect to variations in the vertical direction. In fact, the stratification usually found in lakes inhibits vertical motions, while horizontal variations in density are quickly reduced by horizontal advection and convection. Horizontal exchanges generated by weak temperature gradients are transmitted over several kilometres on time scales of less than a day, suggesting that a one-dimensional model such as DYRESM is applicable for simulations over daily time scales (Antenucci and Imerito, 2001).

The assumption of one-dimensionality motivates the use of a layer construction model, in which the lake is represented as a series of horizontal layers. Lateral or longitudinal variations in the layers are not considered, while vertical profiles are obtained from the values of variables corresponding to each layer.

The layers display different thickness dynamically: as inflows and outflows enter or leave the lake, the affected layers can expand or contract, and those adjacent move up or down to accommodate the volume change. The vertical movement of the layers is accompanied by a corresponding change in layer thickness as the area occupied by each layer varies according to its vertical position (Cacciatori, 2000). The phenomenon of mixing is modelled by an amalgamation of adjacent layers: each layer thickness is dynamically set by the model to ensure an adequate resolution for each process.

In case of upwelling, the flow field is highly complicated, with horizontal motions becoming important. For lakes and reservoirs of "small to medium size" the end result of upwelling is to mix thoroughly the water body. Although DYRESM does not explicitly model the upwelling process, its mixed layer algorithm predicts a mixing efficiency very similar to the real one; this allow one to apply the model even if the Wedderburn number criteria is violated.

8.1.1. The Layer Structure

Introduction

DYRESM is based on a Lagrangian layer scheme in which the lake is modelled by a series of horizontal layers of uniform properties but variable thickness. The layer positions change as inflow, outflow, evaporation and rainfall affect the stored volume. The layer thickness changes as the layers are moved vertically to accommodate volume changes, unlike the Eulerian scheme that needs fixed grids.

This layer scheme adapts itself to the vertical structure of the lake: the mixed layer in which the properties of the species can be considered mostly constant over depth can be modelled as a single layer, while zones of large vertical gradients of properties (i.e. the thermocline) can be expressed through several narrow adjacent layers.

Layers properties: Volume, Area and Thickness

Volumes and surface areas corresponding to a given layer are calculated through a relationship expressed by a power law. The relationship is drawn from an interpolation on the given height-volume-area data for the lake. For example, at time t_{i-1} the layer has a certain thickness, area and volume, while at time t_i a process has changed the thickness or volume of the layer.

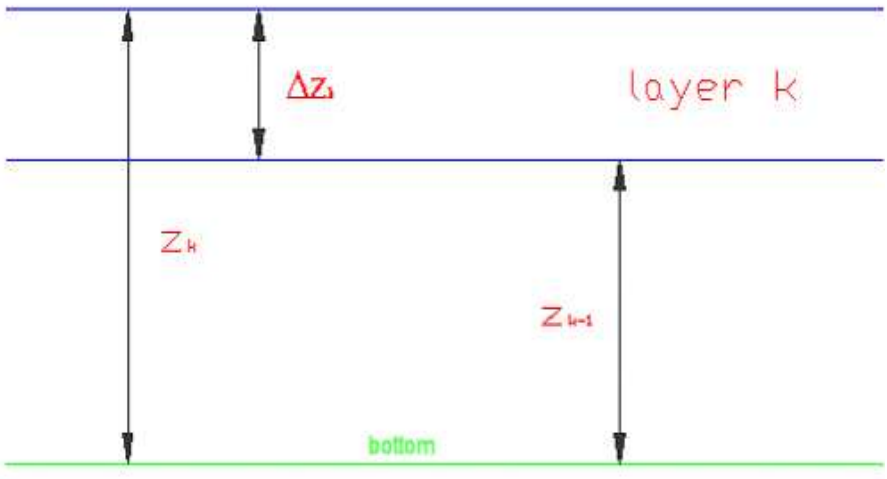

Figure 8.1.: Definition of the height and thickness of a layer.

The layer structure is based on layers having curved sides. Volume and area are calcu-

lated cumulatively from the base upwards, in this form:

$$V(z) = V_{k-1}\left(\frac{z}{z_{k-1}}\right)^{a_k}, \tag{8.1}$$

$$A(z) = A_{k-1}\left(\frac{z}{z_{k-1}}\right)^{b_k}, \tag{8.2}$$

with $0 < z_{k-1} < z_k \quad \vee \; k \in \{2, 3, ..., N\}$, where N is the number of layers.
The coefficients can be estimated as follows:

$$a_k = \frac{\log\left(\frac{V_k}{V_{k-1}}\right)}{\log\left(\frac{z_k}{z_{k-1}}\right)}, \tag{8.3}$$

$$b_k = \frac{\log\left(\frac{A_k}{A_{k-1}}\right)}{\log\left(\frac{z_k}{z_{k-1}}\right)}. \tag{8.4}$$

For the bottom layer, a conical section is used such that

$$A\,(z) = A_1\left(\frac{z}{z_1}\right)^2, \tag{8.5}$$

and hence

$$V\,(z) = V_1\left(\frac{z}{z_1}\right)^3. \tag{8.6}$$

The upper and lower limits of thickness and volume are set to ensure that adequate resolution is achieved and that an excessive number of layers is not used. In any case the limits must be small enough so that numerical diffusion problems do not arise through an excessive number of layer amalgamation. When there are some layers with volume in excess with respect to the allowable maximum one, they are split in the required portions, creating new layers with identical properties but with reduced volume. The layers are renumbered and the surface areas determined. Similarly for layers with a volume less than the allowable minimum, they are amalgamated with the neighbour layer of smallest volume, the layers renumbered and the surface area redetermined.

The density equation

The density of the water (kgm^{-3}) in a generic layer k depends on its temperature T ($^{\circ}C$), salinity S (psu), pressure P ($bars$); the UNESCO equation of state for the density of salt

water is used, which reads:

$$\rho(T,S,P) = \frac{\rho(T,S,0)}{1 - \frac{P}{K(T,S,P)}}, \tag{8.7}$$

where

$$\rho(T,S,0) = A + B\ S\ + C\ S^{3/2} + D\ S^2, \tag{8.8}$$

and

$$K(T,S,P) = E + F\ P + G\ P^2. \tag{8.9}$$

The coefficients are summarized in table 8.1.

Starting with the surface layer, the density of each layer is compared with the density of the layer directly below it. If the density of the overlying layer is larger than the density of the layer below, the layers are combined, the properties of the two layers are conserved, according to the conservation equation of the constituents, and the new density is determined from the new values of temperature and salinity. The density of this layer is then compared to the next layer below it and the process repeated until the lowest layer is reached such that the density profile keeps stable.

Conservation Laws

When two layers are joined, the conservation laws for temperature, salt, energy and momentum give the following weighted mean:

$$C_{i*}^{t+1} = \frac{C_i^t\ \Delta M_i^t + C_{i+1}^t\ \Delta M_{i+1}^t}{\Delta M_i^t + \Delta M_{i+1}^t}, \tag{8.10}$$

where the subscripts refer to layer indices, overscripts to time indices, and C is the property being conserved.

Surface Heat, Mass and Momentum Exchange

The surface heat, mass and momentum exchange are the primary driving mechanisms for DYRESM. These surface exchanges input the majority of the energy for heating, mixing and stratifying the lake. The surface exchanges include heating due to short wave radiation penetration into the lake and the fluxes at the surface due to evaporation, sensible heat

Table 8.1.: Coefficients of equations 8.8 and 8.9.

	A	B
T^0	999.8425	$+8.245\ x10^{-1}$
T^1	$+6.794\ x10^{-2}$	$-4.089\ x10^{-3}$
T^2	$-9.095\ x10^{-3}$	$+7.643\ x10^{-5}$
T^3	$+1.002\ x10^{-4}$	$-8.246\ x10^{-7}$
T^4	$-1.120x10^{-6}$	$+5.387x10^{-9}$
T^5	$+6.536x10^{-9}$	

	C	D
T^0	$-5.725\ x10^{-3}$	$+4.831x10^{-4}$
T^1	$+1.022\ x10^{-4}$	
T^2	$-1.654\ x10^{-6}$	

	E	F
T^0	$19652.21+54.675\ S+7.944\ x10^{-2}\ S^{3/2}$	$3.240+2.284\ x10^{-3}\ S+1.91075\ x10^{-4}\ S^{3/2}$
T^1	$148.421-0.604\ S+1.648\ x10^{-2}\ S^{3/2}$	$1.4317\ x10^{-3}\ -1.098\ x10^{-5}\ S$
T^2	$-2.327+1.1\ x10^{-2}\ S–5.301\ x10^{-4}\ S^{3/2}$	$1.161\ x10^{-4}\ -1.608\ x10^{-6}\ S$
T^3	$1.360\ x10^{-2}\ –6.167\ x10^{-5}\ S$	$-5.779x10^{-7}$
T^4	$-5.155x10^{-5}$	

	G
T^0	$8.510\ x10^{-5}\ -9.935x10^{-7}\ S$
T^1	$-6.123\ x10^{-6}\ +2.081\ x10^{-8}$
T^2	$5.279\ x10^{-8}\ +9.170\ x10^{-10}$

(i.e. convection of heat from the water surface to the atmosphere), long wave in- and back-radiation and wind stress.

The meteorological data used by DYRESM can be either daily or sub-daily. If daily data are entered, all data except shortwave and wind speed are assumed to be uniformly distributed throughout the day. The shortwave energy distribution throughout the day is computed based on the lake latitude and the time of the year. The wind speed can be either uniformly distributed, or have a behaviour like a hump.

If sub-daily data are entered, all data are uniformly distributed within the input timestep. The program requires a sub-daily timestep greater than 10 minutes (600 seconds), and less than 3 hours (10800 seconds).

The data required are schematized in table 8.2:

Table 8.2.: Data required in DYRESM.

variable	*type*	*unit*
short wave radiation	timestep/average	Wm^{-2}
long wave radiation	timestep/average	Wm^{-2}
air vapour pressure	timestep/average	hPa
wind speed	timestep/average	ms^{-1}
air temperature	timestep/average	$^{\circ}C$
rainfall	timestep	m

When these input data are not measured directly, it is possible to rebuild vacancy data using simple formula. In case of long wave radiation (emitted from clouds and atmospheric water vapour), for instance, these data can be calculated from cloud cover, air temperature and humidity even in DYRESM subroutines. In the same way, the reflection coefficient, or albedo, of short wave radiation varies from lake to lake and depends on the angle of the sun, the lake color and the surface wave state (Imberger and Patterson, 1980).

The method consists in calculating the surface energy fluxes and then the surface mass fluxes.

Inflow Dynamics

DYRESM could compute two kinds of inflows: surface flow, due to a river or stream, and subsurface flow, due to groundwater or pipe inflow. Inflows can be either buoyant or dense compared to the ambient fluid at the level of inflow, and so different algorithms are used for these two cases.

1. When a stream (*surface flow*) enters into a lake, it pushes the stagnant water ahead until buoyancy forces, which are due to the density differences become sufficient to halt the flow. At this point the flow can float over the reservoir surface; when the inflow is lighter than the lake water, or it plunges beneath the reservoir water, when it is heavier.

2. The *subsurface inflow* process is modelled in a different way depending on whether the inflow is lighter or denser than the ambient water at the depth of the inflow. For a dense inflow, the model outlined above for surface inflows is followed. For a buoyant subsurface inflow, the flow is modelled as a simple, single-phase plume with circular cross-section. When the upward buoyancy flux driven by density anomaly becomes zero due to the entrained ambient water, the plume stops.

Outflow Dynamics

DYRESM has been developed with the aim of supporting lake management; for this reason the compartment "outflows" comprises two main categories: withdrawal and overflow.

1. In case of *withdrawal*, for each outlet at a given level the required quantity Q is extracted from the adjacent layer. If Q exceeds the volume of this layer then water is taken from successive layers above the outlet until the required volume is removed from the water column. The layer structure is redetermined after each layer has been altered.

2. All water above the crest height is removed from the top of the water body by *overflows*. If there is initially more than one layer above the crest height, then all layers above crest height are removed and a proportion of the remaining layer is removed such that the surface height of the resulting water body is equal to the crest height.

   In lake modelling user can handle, with the greatest care, withdrawals as underground outflows and overflows as surface outlets.

8.1.2. The mixing model

Surface mixing

Three mechanisms of mixing are considered in the model: stirring, when energy from the wind stress is applied to the surface layer, convective overturn, when energy is drawn from

a decrease of potential energy due to dense water falling to a lower level and shear, when kinetic energy is transferred from the upper to the lower layers.

In the surface mixed layer, mixing is performed by conserving mass and momentum on a layer-by-layer basis, starting from the free surface. The method consists in computing the energy available for mixing two layers and in comparing it with the energy required to mix the two layers. If there is sufficient energy, the layers are mixed and the energy in excess is then available for mixing subsequent deeper layers. When there is not enough energy available to mix further layers mixing stops. Any remaining mixing energy is carried over for mixing in the next time step.

Hypolimnion Mixing

The mixed layer algorithm allows the depth of the thermocline to be calculated. The density gradient in the hypolimnion, although weak, has a stabilizing effect; as a result the vertical mixing in the hypolimnion is small.

The mixing mechanisms that occur in the hypolimnion of lakes are very complicated and mainly due to internal wave interaction and breaking, local shear and gravitational overturning.

Hypolimnetic mixing is separated into two parts: internal and boundary mixing. Diffusion within the interior of the water column is modelled by mixing a certain percentage of a layer with the layer above, working from the base up to the surface layer. The user can specify the percentage of mixing and the boundary layer thickness. Aliquot from all hypolimnetic layers are then mixed into the thermocline region.

Benthic boundary pumping and internal mixing are done at the start of each day (and done only once a day), with the boundary layer calculated first. The user provides the boundary layer thickness and fraction of a layer to 'diffuse' into its neighbour per day. Naturally, all these algorithms are not invoked when the water column is fully mixed at the start of the day.

8.2. Simulation

8.2.1. Remarks and general data

As pointed out before, the model is suitable to investigate the evolution of physical properties of the lake, over long time scales (e.g. seasonal).

DYRESM can not simulate the different behaviour of red Bay, where underground

springs converge, supplying important quantity of cold water. Hence, we focus on the main part of Lake Tovel, neglecting gulfs, and we put in the model the cold inflow discharges at a suitable depth corresponding to the same temperature.

The simulation covers a period longer than 200 days: it starts from the middle of May (the first day of field data collection) and ends at the end of October, including the entire Summer 2003.

In order to better characterize heat fluxes and catch sudden changes, the timestep has been set equal to 1 hour (Tonetta, 2003), to avoid average measures of radiation, wind speed and flow rate entering or leaving the lake.

Upper and lower limits of layers have been chosen between $0.2 \div 0.4\ m$ in order to obtain careful resolution and avoid too heavy computations.

For simplicity, the thickness of Benthic Boundary Level has been set equal to zero, neglecting mixing at boundaries.

Input data require relative humidity, air temperature, wind velocity, precipitation, radiation, inflows and outflows; the light extinction and heat exchange coefficients have been chosen as calibration parameters.

With regard to radiation input, the model requires to distinguish between short-wave and long-wave solar radiation: during the night the lake ones receives long wave radiation, while during the day (roughly from 7:00 to 19:00) the incident radiation is characterized by the superimposition of long wave non-penetrative radiation emitted by clouds and short wave penetrative solar radiation. Due to some problem encountered in collecting radiation data, in the simulation of the seasonal period the long wave radiation has been set equal to 300 Wm^{-2} (see figure 8.2), which represents a mean value for long period (Tonetta, 2003).

Air temperature data are required in order to calculate sensible and latent fluxes. The observed seasonal behaviour is rather clear: mean values reach a maximum at the beginning of August ($20°C$) and then start to decrease until they reach $0°C$ at the end of October.

Available field data about inflows and outflows are not exhaustive, as explained above; hence, some assumptions have been made:

- 2 superficial inflows (characterized by known flow rates and temperature) supply the basin.
- 1 superficial outflow (characterized by known flow rates and temperature) withdraws water from the lake until the free surface level allows to spill out.

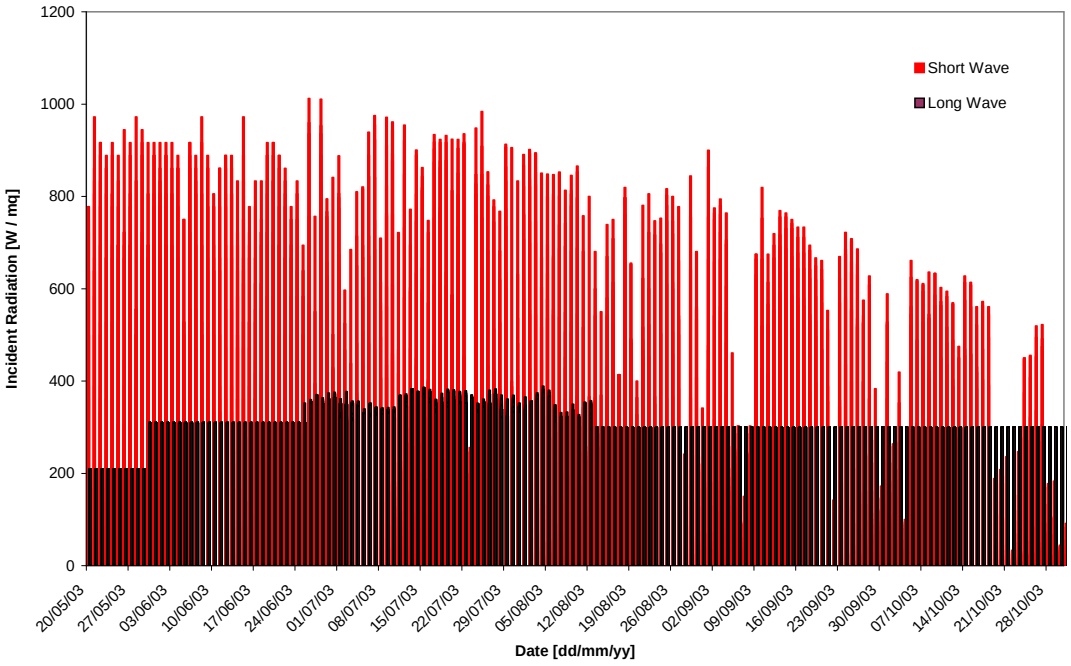

Figure 8.2.: Short Wave and Long Wave Radiation data used in the numerical simulation.

- 1 underground flow (summing the flow rates of all underground springs) always supplies the lake, with temperature set equal to $5{,}5°C$.
- 3 underground outflows spill water from the first 5 m below free surface, which simulate the seepage loss during the period of water level decreasing.

  A summary of the volumes introduced as input data in the model is given in figure 8.4.

8.2.2. Calibration Parameters

As discussed in chapter 1, the latent heat and sensible heat transfer can be expressed as:

$$Q_l = -\rho_a \, L_w \, C_L \, U_a \, \left(e_a - e_w\right), \tag{8.11}$$

$$Q_{sh} = C_s \rho_a \, C_p U_a \left(T_a - T_s\right) \Delta t. \tag{8.12}$$

To compute these fluxes, air and water temperature, vapor pressure and wind velocity

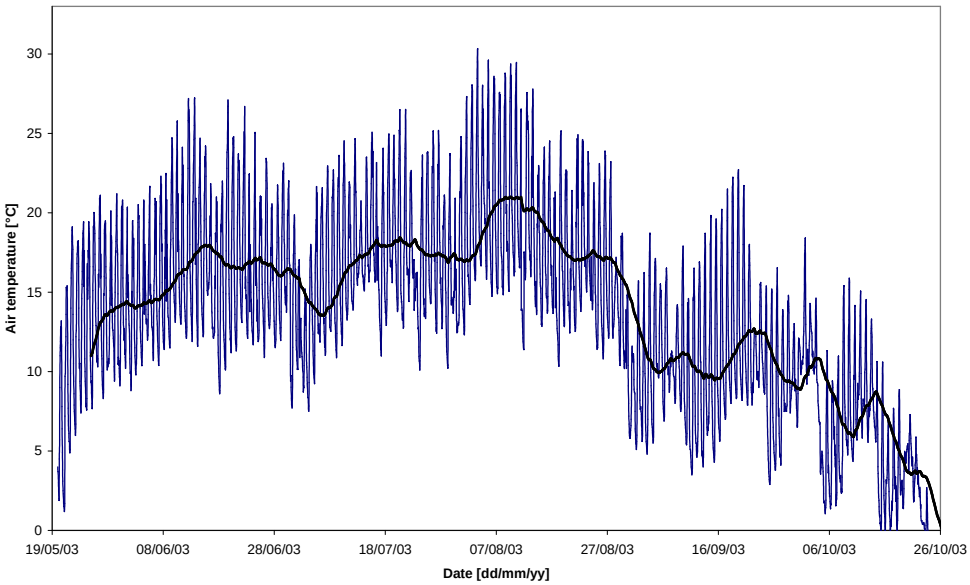

Figure 8.3.: The time variation of air temperature at Tovel lake observed during the field campaign (temperature diurnal range and mean data)

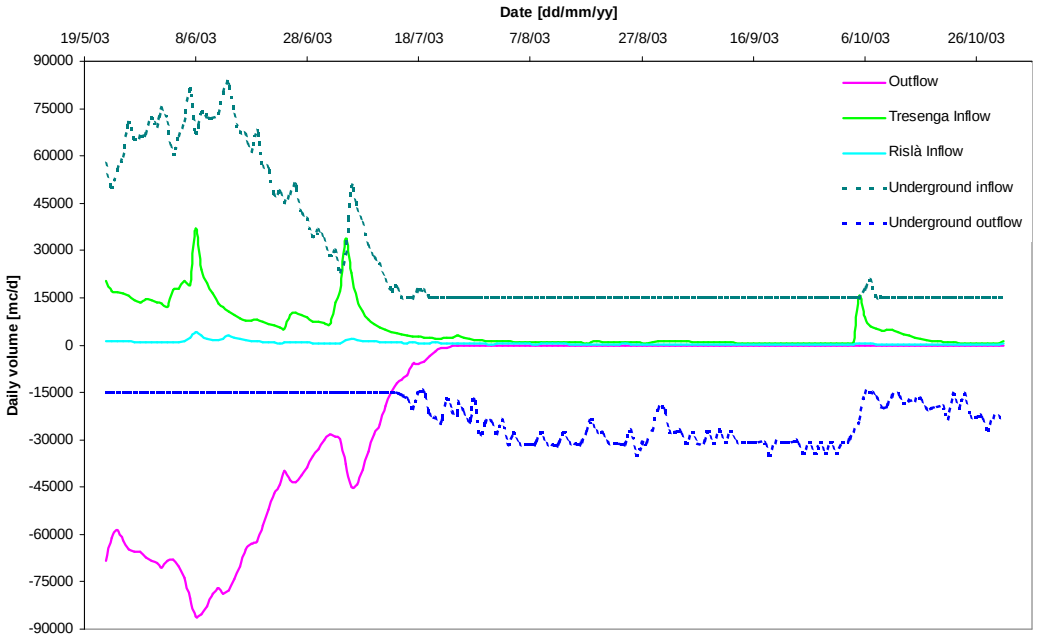

Figure 8.4.: Volume of water entering and leaving Lake Tovel, as considered in 1-D model.

must be known.

Evaporation and heat transfer are important sources of heat loss for lakes; therefore these parameters must be set accurately to control and quantify heat exchanges between lake surface and atmosphere.

In the model both C_s and C_L have been set equal to 0.0037 (Tonetta, 2003).

The resulting fluxes are shown in figure 8.5 and 8.6.

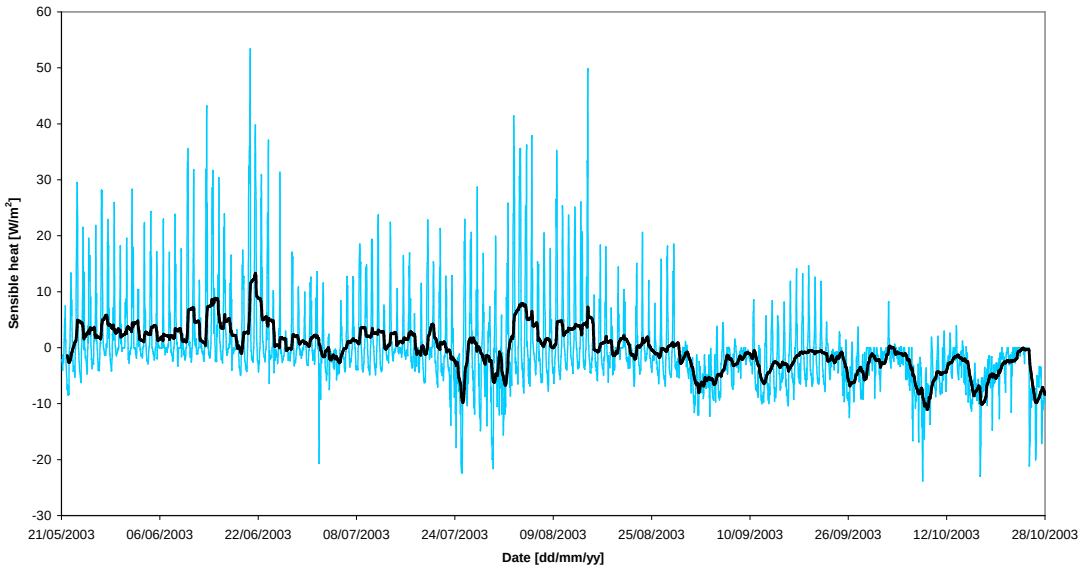

Figure 8.5.: Sensible heat flux at the surface lake.

The sensible heat displays a standard behaviour and moves from negative values during the night, when the lake loses heat because of greater temperature of the surface layer with respect to the air, to positive values during the day, when conduction and convection are directed from the air, which is warmer than the water surface. The peak values, roughly equal to 50 Wm^{-2}, are associated with periods of strong heating of the stretch of water. During cooling periods, like in Autumn, the sensible heat is always negative, showing a constant cooling of water even in afternoon.

Latent heat values have been calculated in similar way. The condensation effects can be neglected (hence positive values are not considered), while the evaporation phenomenon has been estimated with flux not greater than 130 Wm^{-2} (in absolute value). The mean values show their maximum in August, when the water surface has reached the largest temperature and evaporation could occur easily.

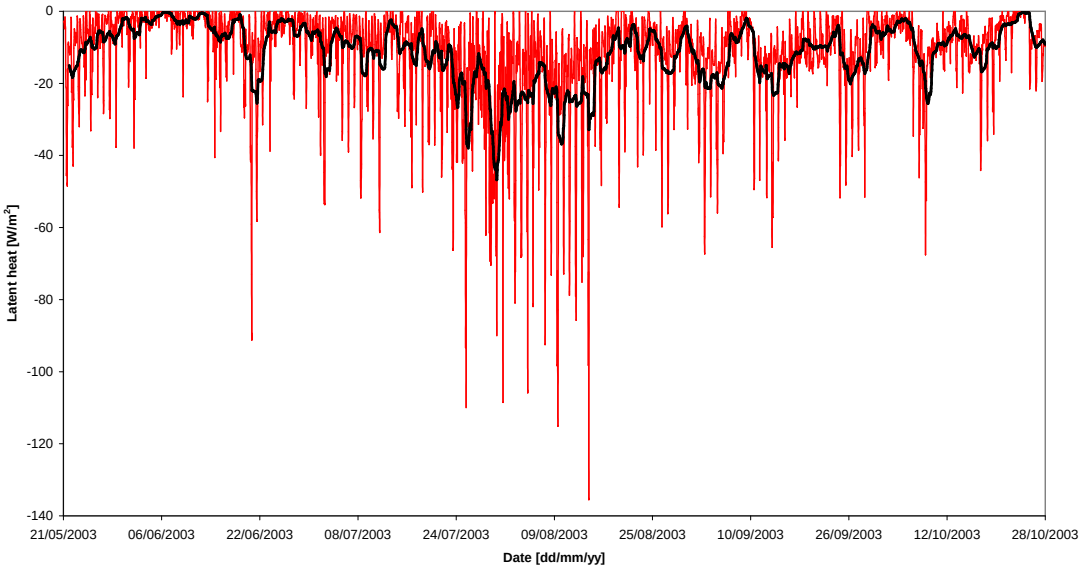

Figure 8.6.: Latent heat flux at the lake surface.

A typical daily portrait of heat fluxes, computed according to this calibration, is displayed in figure 8.7

Notice that the other calibration parameter, namely the extinction coefficient k, has been set equal to 0.13, in agreement with the results of depth measures performed with Secchi disk (depths estimated are always over 10 m) .

8.2.3. Results

The comparison between measured and simulated isotherms displays a good agreement both in surface layers and in deep zones (see figures 8.8 and 8.9).

The isotherm corresponding to $8°C$ displays the same behaviour: it deepens from 10 m to 15 m in July and moves upward toward the surface at the end of October. The behaviour of isotherms corresponding to $10°C$ and 12 $°C$ shows some differences: in fact, according to the results of simulation deepening starts from June and occurs more gradually with respect to field data, which exhibit a faster deepening mainly concentrated in July; moreover, the model reproduces reasonably well the upward movement of isotherms though field data show a much steep reascendings of isotherms $14°C$, $12°C$ and $10°C$. Finally, simulated and field data correspond quite well at the surface.

The model can capture the general thermodynamics of the lake, as shown in figure

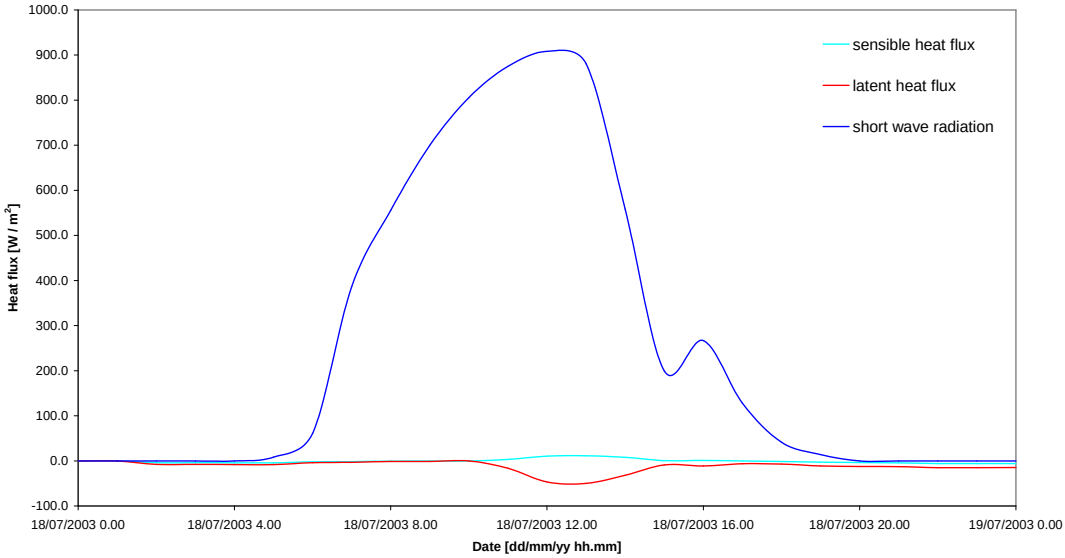

Figure 8.7.: Lake Tovel: heat fluxes in a typical summer day.

8.10. This comparison is performed each day, at 12:00, with temperature data collected by sensors moored on the chain D, which can be considered as representative of the entire lake. The heating process essentially develops in the first superficial 5 m, where temperature changes from $11°C$ in May to $20°C$ at the end of July. The mixed surface layer is very thin and the model seems able to replicate this behaviour: mixing doesn't occur in the first layers, while the wind action does not make significant effects until the seasonal weather conditions start to change, as Autumn is approaching.

In fact, after the month of August the temperature profile shows a sudden cooling at the surface, accompanied by a progressive heating of the central part of water column. In all cases the agreement between observations and simulation is satisfactory.

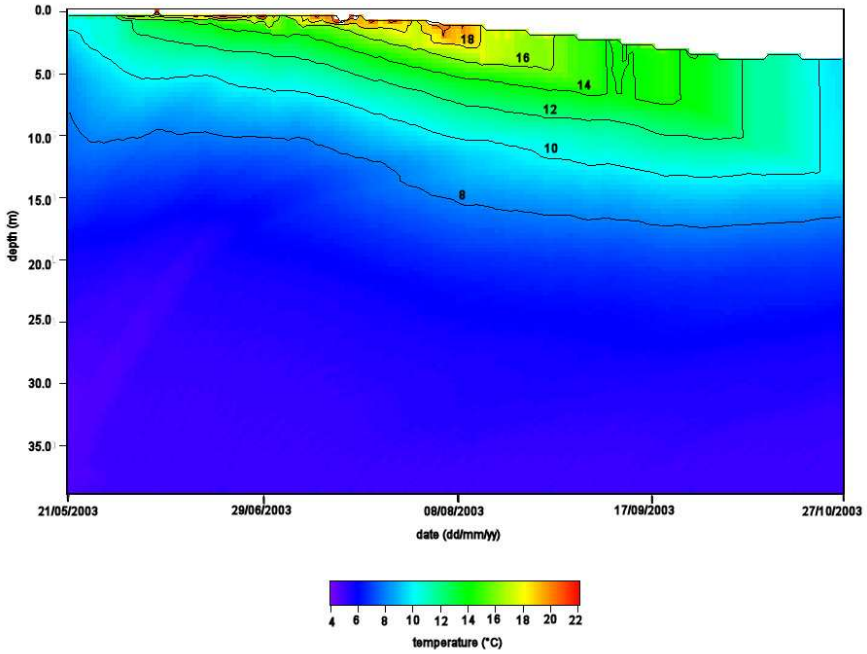

Figure 8.8.: Simulated temperature data during the Summer 2003.

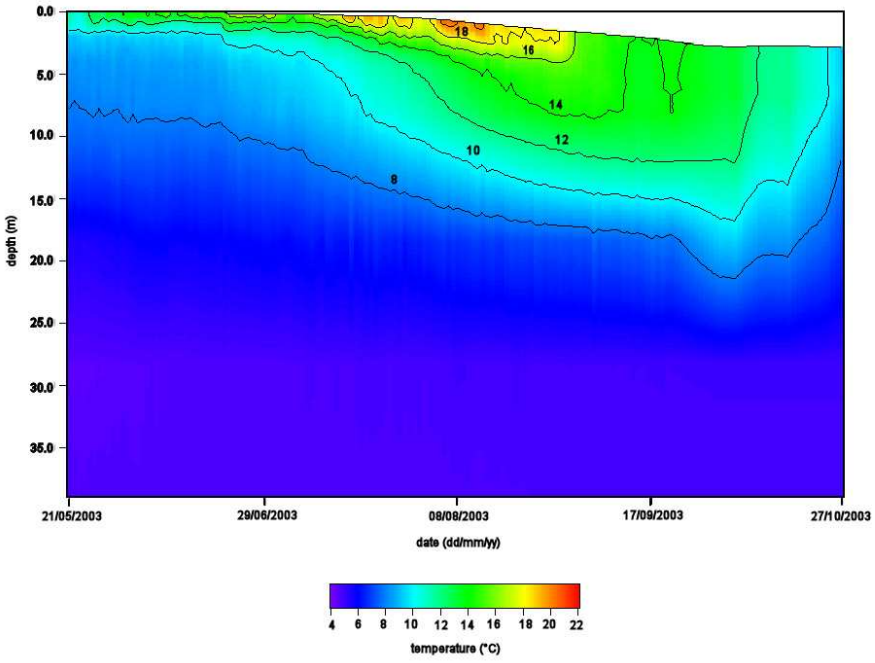

Figure 8.9.: Observed temperature data during the Summer 2003.

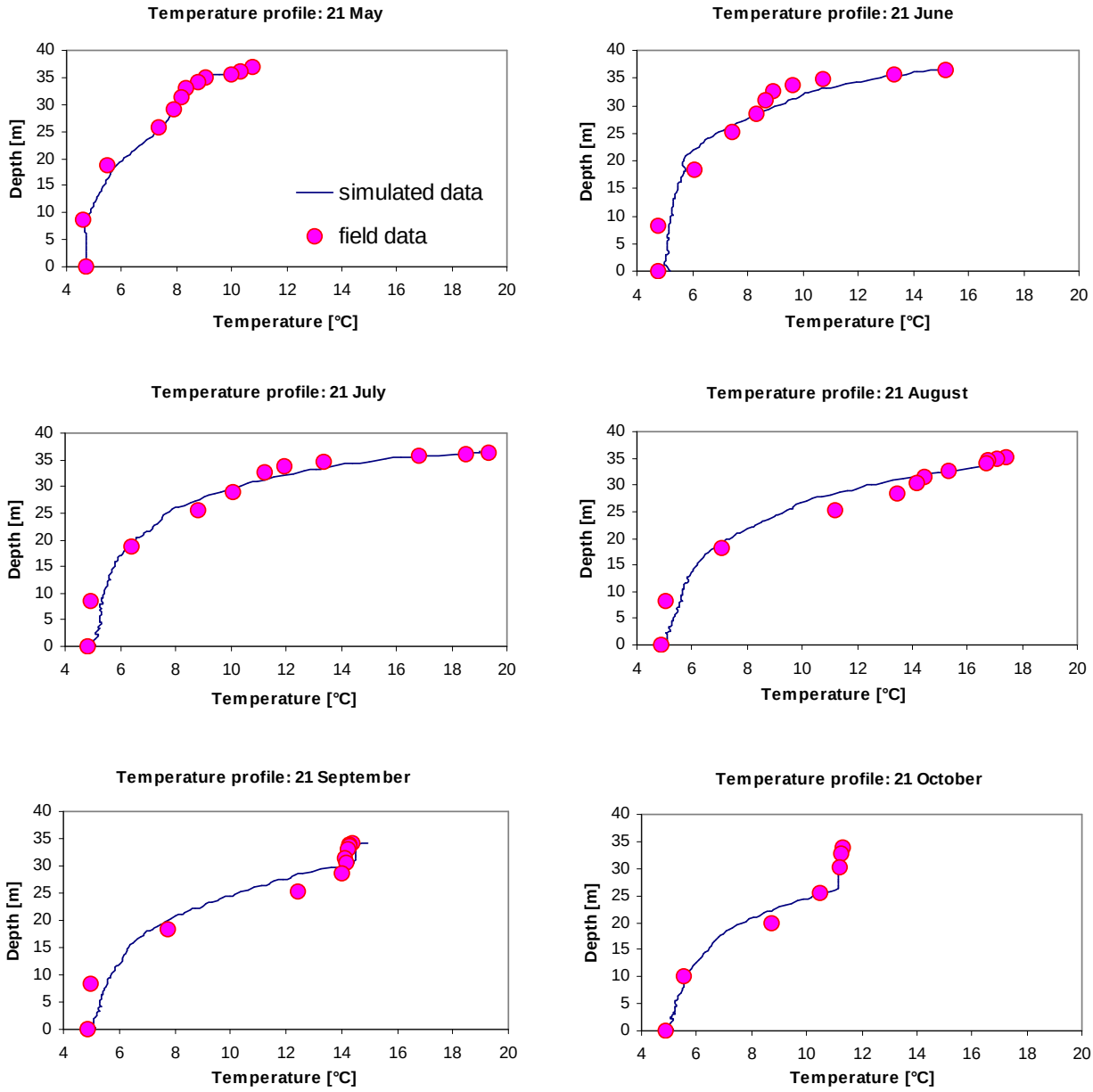

Figure 8.10.: Comparison between measured and simulated temperature profiles from May to October 2003.

9. 3-D Model

9.1. Quasi non-hydrostatic semi-implicit model

9.1.1. Introduction

In lakes, the majority of environmental problems can be solved analyzing the 3-D equations with the hydrostatic assumption, except in some cases where solitons are propagating with high velocity (high frequency waves) or at the boundary, where the vertical velocities assume non-negligible values. Problems where the hydrostatic approximation is no longer valid include flows over rapidly varying slopes and short waves where the ratio of the vertical to horizontal scales of motion is not sufficiently small (Casulli, 1999).

The governing equations are the Navier-Stokes equations, which have been discretized and solved through a semi-implicit technique, with fractional step method, whereby the hydrostatic pressure component is determined first and the non-hydrostatic component of the pressure is computed in a subsequent step, following the procedure proposed by Casulli and Stelling (1998). Convective and viscous terms are discretized in a Eulerian-Lagrangian method, while barotropic and vertical viscosity terms have been expressed implicitly in the horizontal equations (Casulli and Cheng, 1992). The exchanges of momentum between each layer have been expressed by tridiagonal matrix, relating the discrete horizontal velocities in each vertical level to the gradient of the water surface elevations (barotropic pressure gradient).

Substituting the solutions of horizontal velocities into the vertically integrated continuity equation we obtain a linear five-diagonal system. The only unknowns are the water surface elevations in the domain of interest. Once free surface has been determined using conjugate gradient method (because the system is symmetric and positive defined), the horizontal velocity can be calculated directly. The second step consists in adjusting each velocity through hydrodynamic pressure and imposing that the new velocity field is divergence free. Finally, having determined the pressure component for each cell, the velocity field is corrected.

This method is relatively simple, numerically stable even at large Courant numbers, and

is suitable for simulations of complex three-dimensional flows when a small deviation from hydrostatic pressure is allowed (Casulli, 1999).

9.1.2. Governing Equations

The momentum equations for an incompressible fluid take the following form

$$\frac{\partial u_i}{\partial t} + \frac{\partial \left(u_i u_j\right)}{\partial x_j} = -\frac{\partial}{\partial x_i}\left(\frac{p}{\rho_0} - g x_3\right) + \nu \frac{\partial^2 u_i}{\partial x_i x_j}, \tag{9.1}$$

where $u_1(x,y,z,t)$, $u_2(x,y,z,t)$ and $u_3(x,y,z,t)$ are the velocity components in the horizontal x_1-, x_2- and vertical x_3-direction (or $x-, y-, z-$direction), t is the time, $p(x,y,z,t)$ is the pressure, ρ_0 is the constant reference density, g is the gravitational acceleration and ν is the viscosity coefficient. Averaging over turbulence we obtain:

$$\frac{\partial \overline{u_i}}{\partial t} + \overline{u}_j \frac{\partial \overline{u_i}}{\partial x_j} = -\frac{\partial}{\partial x_i}\left[\frac{\overline{p}}{\rho_0} - g x_3\right] + \frac{\partial}{\partial x_j}\left[\nu_j^T \frac{\partial \overline{u_i}}{\partial x_j}\right], \tag{9.2}$$

where the overline means average and ν^T is the turbulent viscosity which arises from a Boussinesq type closure model:

$$-\overline{u_i' u_j'} = \nu_j^T \left(\frac{\partial \overline{u_i}}{\partial x_j}\right) \tag{9.3}$$

Notice that a complete model for field scale application should include the Coriolis acceleration and non-constant turbulent viscosity coefficients (Casulli and Stelling, 1998).

The mass conservation is expressed by the following incompressibility condition:

$$\frac{\partial \overline{u_i}}{\partial x_i} = 0, \tag{9.4}$$

while the scalar advection-diffusion equation is:

$$\frac{\partial \overline{S}}{\partial t} + \frac{\partial}{\partial x_i}\left(\overline{u}_i \overline{S}\right) = \frac{\partial}{\partial x_i}\left[\nu_i^T \frac{\partial \overline{S}}{\partial x_i}\right]. \tag{9.5}$$

The equations (9.2),(9.4) and (9.5) can be rewritten in a non-dimensional form, once the following scaling is introduced:

1.
   - $(x^+, y^+, z^+, h^+, \eta^+) = h_0^* \cdot (x, y, z, h, \eta)$, where h_0^* is the surface mixed layer depth, h and η denote the bottom and water surface elevation, respectively.
   - $(u^+, v^+, w^+) = U_0^* \cdot (\overline{u}, \overline{v}, \overline{w})$ where U_0^* is the friction velocity at the surface boundary

- $p^+ = \rho_0 U_0^{*2} \overline{p}$
- $\nu^{T+} = U_0^* H_0^* \cdot \nu^T$
- $t^+ = \frac{h_0^*}{U_0^*} t$

Momentum equations in dimensionless form read:

$$\frac{\partial u}{\partial t} + u\frac{\partial u}{\partial x} + v\frac{\partial u}{\partial y} + w\frac{\partial u}{\partial z} = -\frac{\partial p}{\partial x} + \frac{\partial}{\partial x}\left[\nu_x^T \frac{\partial u}{\partial x}\right] + \frac{\partial}{\partial y}\left[\nu_y^T \frac{\partial u}{\partial y}\right] + \frac{\partial}{\partial z}\left[\nu_z^T \frac{\partial u}{\partial z}\right], \tag{9.6}$$

$$\frac{\partial v}{\partial t} + u\frac{\partial v}{\partial x} + v\frac{\partial v}{\partial y} + w\frac{\partial v}{\partial z} = -\frac{\partial p}{\partial y} + \frac{\partial}{\partial x}\left[\nu_x^T \frac{\partial v}{\partial x}\right] + \frac{\partial}{\partial y}\left[\nu_y^T \frac{\partial v}{\partial y}\right] + \frac{\partial}{\partial z}\left[\nu_z^T \frac{\partial v}{\partial z}\right], \tag{9.7}$$

$$\frac{\partial w}{\partial t} + u\frac{\partial w}{\partial x} + v\frac{\partial w}{\partial y} + w\frac{\partial w}{\partial z} = -\frac{\partial p}{\partial z} - \frac{1}{Fr^2} + \frac{\partial}{\partial x}\left[\nu_x^T \frac{\partial w}{\partial x}\right] + \frac{\partial}{\partial y}\left[\nu_y^T \frac{\partial w}{\partial y}\right] + \frac{\partial}{\partial z}\left[\nu_z^T \frac{\partial w}{\partial z}\right], \tag{9.8}$$

where overlines have been omitted and $Fr^2 = \frac{U_0^{*2}}{g h_0^*}$ is the Froude number. Furthermore, the scalar transport equation is:

$$\frac{\partial S}{\partial t} + \frac{\partial (uS)}{\partial x} + \frac{\partial (vS)}{\partial y} + \frac{\partial (wS)}{\partial z} = \frac{\partial}{\partial x}\left[\nu_x^T \frac{\partial S}{\partial x}\right] + \frac{\partial}{\partial y}\left[\nu_y^T \frac{\partial S}{\partial y}\right] + \frac{\partial}{\partial z}\left[\nu_z^T \frac{\partial S}{\partial z}\right], \tag{9.9}$$

while the mass conservation equation (9.4) remains unchanged.

Integrating the continuity equation (9.4) over the depth $(h - \eta)$ and using the kinematic condition at the free-surface [10] leads to the following free-surface equation

$$\frac{\partial \eta}{\partial t} + \frac{\partial}{\partial x}\left[\int_h^\eta u dz\right] + \frac{\partial}{\partial y}\left[\int_h^\eta v dz\right] = 0, \tag{9.10}$$

where $h(x,y)$ is the bottom elevation measured from the undisturbed water surface and $\eta(x,y,t)$ is the free-surface elevation.

The normalized pressure $p(x,y,z,t)$ in equations (9.6), (9.7) and (9.8), can be decomposed into the sum of its hydrostatic and a non-hydrostatic component. Thus, the pressure at any point (x,y,z) can be rewritten as:

$$p(x,y,z,t) = p_h(x,y,z,t) + q(x,y,z,t), \tag{9.11}$$

where $q(x,y,z,t)$ denotes the hydrodynamic pressure component, while the hydrostatic pressure component $p_h(x,y,z,t)$ is determined from the vertical momentum equation (9.8) by neglecting the convective and the viscous acceleration terms. In turn, p_h can be split into a barotropic part and a baroclinic component which accounts for density variations:

$$p_h(x,y,z,t) = p_a\,(x,y,t) + \frac{\eta\,(x,y,t) - z}{Fr^2} + \frac{1}{\rho_0}\int_z^\eta \rho' dz, \tag{9.12}$$

where p_a is the atmospheric pressure.

Neglecting the gradient of p_a, the momentum equations can be written as:

$$\begin{aligned}\frac{\partial u}{\partial t} + u\frac{\partial u}{\partial x} + v\frac{\partial u}{\partial y} + w\frac{\partial u}{\partial z} = -\frac{1}{Fr^2}\left(\frac{\partial h}{\partial x} + \frac{\partial}{\partial x}\int_z^\eta \frac{\rho'}{\rho_0}dz\right) - \frac{\partial q}{\partial x} + \\ + \frac{\partial}{\partial x}\left[\nu_x^T\frac{\partial u}{\partial x}\right] + \frac{\partial}{\partial y}\left[\nu_y^T\frac{\partial u}{\partial y}\right] + \frac{\partial}{\partial z}\left[\nu_z^T\frac{\partial u}{\partial z}\right],\end{aligned} \tag{9.13}$$

$$\begin{aligned}\frac{\partial v}{\partial t} + u\frac{\partial v}{\partial x} + v\frac{\partial v}{\partial y} + w\frac{\partial v}{\partial z} = -\frac{1}{Fr^2}\left(\frac{\partial h}{\partial y} + \frac{\partial}{\partial y}\int_z^\eta \frac{\rho'}{\rho_0}dz\right) - \frac{\partial q}{\partial y} + \\ + \frac{\partial}{\partial x}\left[\nu_x^T\frac{\partial v}{\partial x}\right] + \frac{\partial}{\partial y}\left[\nu_y^T\frac{\partial v}{\partial y}\right] + \frac{\partial}{\partial z}\left[\nu_z^T\frac{\partial v}{\partial z}\right],\end{aligned} \tag{9.14}$$

$$\begin{aligned}\frac{\partial w}{\partial t} + u\frac{\partial w}{\partial x} + v\frac{\partial w}{\partial y} + w\frac{\partial w}{\partial z} = -\frac{\partial q}{\partial z} + \\ + \frac{\partial}{\partial x}\left[\nu_x^T\frac{\partial w}{\partial x}\right] + \frac{\partial}{\partial y}\left[\nu_y^T\frac{\partial w}{\partial y}\right] + \frac{\partial}{\partial z}\left[\nu_z^T\frac{\partial w}{\partial z}\right].\end{aligned} \tag{9.15}$$

At the free-surface the boundary conditions are given by

$$\nu^T \left(\frac{\partial u}{\partial z} - \frac{\partial u}{\partial x}\frac{\partial h}{\partial x} - \frac{\partial u}{\partial y}\frac{\partial h}{\partial y} \right) = \gamma_t \left(u_w - u^s \right), \tag{9.16}$$

$$\nu^T \left(\frac{\partial v}{\partial z} - \frac{\partial v}{\partial x}\frac{\partial h}{\partial x} - \frac{\partial v}{\partial y}\frac{\partial h}{\partial y} \right) = \gamma_t \left(v_w - v^s \right), \tag{9.17}$$

where γ_t is a non-negative wind stress coefficient (typically $\gamma_t = C_D \frac{\rho_a}{\rho} \sqrt{u_w^2 + v_w^2}$) and u_w and v_w are the wind velocity components in the x- and in the y-direction, respectively, u^s and v^s are the horizontal components of water velocity at the surface.

At the bed, the bottom friction is likewise expressed by:

$$\nu^T \frac{\partial u}{\partial z} = \gamma_b \; u, \tag{9.18}$$

$$\nu^T \frac{\partial v}{\partial z} = \gamma_b \; v, \tag{9.19}$$

where γ_b is a non-negative bottom friction coefficient.

9.1.3. Discretized equations

Momentum equations

In order to obtain an efficient numerical method whose stability is independent on the free-surface wave speed, wind stress, bottom friction and vertical viscosity, a semi-implicit fractional step scheme is derived. In the first step, the implicit contribution of the non-hydrostatic pressure is neglected and the gradient of surface elevation in the horizontal momentum equations and the velocity in the free-surface equation are discretized by the θ method (Casulli and Cattani, 1994). Moreover, for stability, the wind stress, the vertical viscosity and the bottom friction are discretized implicitly. In the second step the provisional velocity and surface elevation are corrected by including the non-hydrostatic pressure terms, which are calculated in such a fashion that the resulting velocity field is locally and globally mass conservative.

The physical domain is subdivided into $N_x N_y N_z$ rectangular cells of length Δx, width Δy and height $\Delta z_k = z_{k+1/2} - z_{k-1/2}$ respectively, where $z_{k\pm1/2}$ are given level surfaces. The cell is staggered, numbered at its center with indices i, j and k: the discrete u velocity is then defined at the est face ($u_{i+1/2,j,k}$), the v velocity at the north face ($v_{i,j+1/2,k}$) and the vertical velocity w at the up face ($w_{i,j,k+1/2}$), while the pressure q and other properties (e.g. temperature, density, etc.) are defined in centre cell (figure 9.1). In general, Δz

depends on the spatial location, and near the free-surface it also depends on the time, because the surface elevation, defined in centre column ($\eta^n_{i,j}$), can change at the time step n.

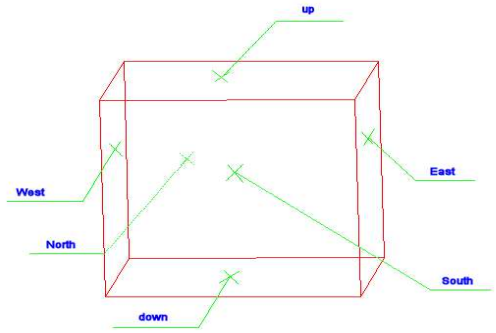

Figure 9.1.: Staggered cell.

A general semi-implicit discretization for the momentum equations, using an Eulerian-Lagrangian scheme and neglecting the hydrodynamic pressure, leads to the following expression:

$$\frac{\tilde{u}^{n+1}_{i+\frac{1}{2},j,k} - u^n_{i+\frac{1}{2}-a,j-b,k-d}}{\Delta t} = -\frac{1}{Fr^2}\theta\frac{\eta^{n+1}_{i+1,j} - \eta^{n+1}_{i,j}}{\Delta x} - \frac{1}{Fr^2}(1-\theta)\frac{\eta^n_{i+1,j} - \eta^n_{i,j}}{\Delta x} + \\ -\frac{1}{\Delta x \rho_0 Fr^2}\sum_k^{K_t}\left[\left(\rho'_{i+1,j,k} - \rho'_{i,j,k}\right)\Delta z^n_{i+\frac{1}{2},j,k}\right] \\ + \frac{\nu^z_{i+\frac{1}{2},j,k+\frac{1}{2}}\frac{\tilde{u}^{n+1}_{i+\frac{1}{2},j,k+1} - \tilde{u}^{n+1}_{i+\frac{1}{2},j,k}}{\Delta z^n_{i+\frac{1}{2},j,k}} - \nu^z_{i+\frac{1}{2},j,k-\frac{1}{2}}\frac{\tilde{u}^{n+1}_{i+\frac{1}{2},j,k} - \tilde{u}^{n+1}_{i+\frac{1}{2},j,k-1}}{\Delta z^n_{i+\frac{1}{2},j,k}}}{\Delta z^n_{i+\frac{1}{2},j,k}}, \tag{9.20}$$

where the weighting coefficient θ ranges between 0 and 1 and generally is fixed at 1/2. A similar structure is obtained for the momentum equation in y-direction.

In matrix notation the above expression can be written in a more compact form:

$$\mathbf{A}^n_{i+\frac{1}{2},j}\mathbf{U}^{n+1}_{i+\frac{1}{2},j} = \mathbf{G}^n_{i+\frac{1}{2},j,k} - \frac{1}{Fr^2}\theta\frac{\Delta t}{\Delta x}\left(\eta^{n+1}_{i+1,j} - \eta^{n+1}_{i,j}\right)\Delta z_{i+\frac{1}{2},j,k}, \tag{9.21}$$

where

$$\mathbf{A}^{n+1}_{i+\frac{1}{2},j} = \begin{pmatrix} d_{i+\frac{1}{2},j,K_t} & -a_{K_t-\frac{1}{2}} & & \\ -a_{K_t-\frac{1}{2}} & d_{i+\frac{1}{2},j,K_t-1} & -a_{K_t-\frac{3}{2}} & \\ & \cdot & \cdot & \cdot \\ & & -a_{K_b+\frac{1}{2}} & d_{i+\frac{1}{2},j,K_b} \end{pmatrix}, \tag{9.22}$$

and the terms on the diagonal are defined as follows:

$$d_{i+\frac{1}{2},j,K_t} = \Delta z^n_{i+\frac{1}{2},j,K_t-\frac{1}{2}} + a_{K_t-\frac{1}{2}} - \gamma_t \Delta t, \tag{9.23}$$

$$d_{i+\frac{1}{2},j,K_L} = \Delta z^n_{i+\frac{1}{2},j,K_t-\frac{1}{2}} + a_{K_t-\frac{1}{2}} + a_{K_t-\frac{3}{2}} \; for \, L = K_t - 1 \,..\, K_b + 1, \tag{9.24}$$

$$d^{(N_z^2)}_{i+\frac{1}{2},j,K_b} = a_{K_b+\frac{1}{2}} + \Delta z^n_{i+\frac{1}{2},j,K_b+\frac{1}{2}} + a_{K_b}. \tag{9.25}$$

The extra-diagonal terms are defined as $a_k = \frac{\nu^z_k \Delta t}{\Delta z}$, while:

$$\mathbf{G}^n_{i+\frac{1}{2},j,k} = \begin{pmatrix} F\left(u^n_{i+\frac{1}{2}-a,j-b,K_t-d}\right) + \Delta t \; \gamma^n_t u^n_a - \frac{1}{Fr^2}(1-\theta)\frac{\eta^n_{i+1,j}-\eta^n_{i,j}}{\Delta x}\Delta z^n_{i+\frac{1}{2},j,k} - \\ -\frac{1}{Fr^2}\frac{\Delta t}{\Delta x}\left(\sum_{k_t}^{K_t}\frac{\rho'_{i+1,j,k}}{\rho_0}\Delta z^n_{i+1,i,k} - \sum_{k}^{K_t}\frac{\rho'_{i,j,k}}{\rho_0}\Delta z^n_{i,i,k}\right) \\ F\left(u^n_{i+\frac{1}{2}-a,j-b,K_t-1-d}\right) - \frac{1}{Fr^2}(1-\theta)\frac{\eta^n_{i+1,j}-\eta^n_{i,j}}{\Delta x}\Delta z^n_{i+\frac{1}{2},j,k} - \\ -\frac{1}{Fr^2}\frac{\Delta t}{\Delta x}\sum_{k}^{K_t}\left(\rho'_{i+1,j,k} - \rho'_{i,j,k}\right)\Delta z^n_{i+\frac{1}{2},j,k} \\ \cdot \\ F\left(u^n_{i+\frac{1}{2}-a,j-b,K_b+1-d}\right) - \frac{1}{Fr^2}(1-\theta)\frac{\eta^n_{i+1,j}-\eta^n_{i,j}}{\Delta x}\Delta z_{i+\frac{1}{2},j,k} - \\ -\frac{1}{Fr^2}\frac{\Delta t}{\Delta x}\left(\sum_{k_{b+1}}^{K_t}\frac{\rho'_{i+1,j,k}}{\rho_0}\Delta z^n_{i+1,i,k} - \sum_{k}^{K_t}\frac{\rho'_{i,j,k}}{\rho_0}\Delta z^n_{i,i,k}\right) \\ F\left(u^n_{i+\frac{1}{2}-a,j-b,K_b-d}\right) - \frac{1}{Fr^2}(1-\theta)\frac{\eta^n_{i+1,j}-\eta^n_{i,j}}{\Delta x}\Delta z^n_{i+\frac{1}{2},j,k} - \\ -\frac{1}{Fr^2}\frac{\Delta t}{\Delta x}\sum_{k_b}^{K_t}\left(\rho'_{i+1,j,k} - \rho'_{i,j,k}\right)\Delta z^n_{i+\frac{1}{2},j,k} \end{pmatrix} \tag{9.26}$$

The momentum equation in vertical z-direction takes the form:

$$\frac{\widetilde{w}^{n+1}_{i+\frac{1}{2},j,k} - w^n_{i+\frac{1}{2}-a,j-b,k-d}}{\Delta t} = \\ = \frac{\nu^z_{i+\frac{1}{2},j,k+\frac{1}{2}}\frac{\hat{w}^{n+1}_{i+\frac{1}{2},j,k+1} - \hat{w}^{n+1}_{i+\frac{1}{2},j,k}}{\Delta z^n_{i+\frac{1}{2},j,k}} - \nu^z_{i+\frac{1}{2},j,k-\frac{1}{2}}\frac{\hat{w}^{n+1}_{i+\frac{1}{2},j,k} - \hat{w}^{n+1}_{i+\frac{1}{2},j,k-1}}{\Delta z^n_{i+\frac{1}{2},j,k}}}{\Delta z^n_{i+\frac{1}{2},j,k}} \tag{9.27}$$

where the symbol ˜ means provisional velocity.

In order to determine $\eta_{i,j}$, the intermediate velocity field is required to satisfy, for each i and j the discrete analogue of the free-surface equation integrated on the water column (9.10):

$$\frac{\eta_{i,j}^{n+1}-\eta_{i,j}^{n}}{\Delta t}+\frac{\sum_{k=K_b}^{K_t} u_{i+\frac{1}{2},,j,k}^{n+\theta}\Delta z_{i+\frac{1}{2},j,k}^{n}-\sum_{k=K_b}^{K_t} u_{i-\frac{1}{2},,j,k}^{n+\theta}\Delta z_{i-\frac{1}{2},j,k}^{n}}{\Delta x}+ \\ +\frac{\sum_{k=K_b}^{K_t} v_{i,j+\frac{1}{2},k}^{n+\theta}\Delta z_{i,,j+\frac{1}{2},k}-\sum_{k=K_b}^{K_t} v_{i,j-\frac{1}{2},k}^{n+\theta}\Delta z_{i,j-\frac{1}{2},k}^{n}}{\Delta y}=0, \tag{9.28}$$

where:

$$u^{n+\theta}=\theta u^{n+1}+(1-\theta)\,u^{n}, \tag{9.29}$$

$$v^{n+\theta}=\theta v^{n+1}+(1-\theta)\,v^{n}. \tag{9.30}$$

The x-, y-momentum equations and (9.28) constitute a linear system in the horizontal provisional velocities and free surface (Casulli and Cheng, 1992).

This system can be reduced to a smaller five diagonal system of N_xN_y equations where the only unknows are the values $\eta_{i,j}$ by substitution of (9.21) in x-, y-direction in (9.28); we obtain:

$$\eta_{i,j}^{n+1}+\frac{\Delta t^2\theta^2}{Fr^2\Delta x^2}\left[\begin{array}{l}\left(\mathbf{\Delta z}^T\mathbf{A}^{-1}\mathbf{\Delta z}\right)_{i+\frac{1}{2}j}^{n}\left(h_{i+1,j}^{n+1}-h_{i,j}^{n+1}\right)-\\ -\left(\mathbf{\Delta z}^T\mathbf{A}^{-1}\mathbf{\Delta z}\right)_{i-\frac{1}{2}j}^{n}\left(h_{i,j}^{n+1}-h_{i-1,j}^{n+1}\right)\end{array}\right]+ \\ +\frac{\Delta t^2\theta^2}{Fr^2\Delta y^2}\left[\begin{array}{l}\left(\mathbf{\Delta z}^T\mathbf{A}^{-1}\mathbf{\Delta z}\right)_{ij+\frac{1}{2}}^{n}\left(h_{i,j+1}^{n+1}-h_{i,j}^{n+1}\right)-\\ -\left(\mathbf{\Delta z}^T\mathbf{A}^{-1}\mathbf{\Delta z}\right)_{ij-\frac{1}{2}}^{n}\left(h_{i,j}^{n+1}-h_{i,j-1}^{n+1}\right)\end{array}\right]= \\ =\eta_{i,j}^{n}-\theta\frac{\Delta t}{\Delta x}\left[\left(\mathbf{\Delta z}^T\mathbf{A}^{-1}\mathbf{G}\right)_{i+\frac{1}{2}j}^{n}-\left(\mathbf{\Delta z}^T\mathbf{A}^{-1}\mathbf{G}\right)_{i-\frac{1}{2}j}^{n}\right]- \\ -\theta\frac{\Delta t}{\Delta y}\left[\left(\mathbf{\Delta z}^T\mathbf{A}^{-1}\mathbf{G}\right)_{ij+\frac{1}{2}}^{n}-\left(\mathbf{\Delta z}^T\mathbf{A}^{-1}\mathbf{G}\right)_{ij-\frac{1}{2}}^{n}\right]- \\ -(1-\theta)\frac{\Delta t}{\Delta x}\left[\mathbf{\Delta z}^T\mathbf{U}_{i+\frac{1}{2}j}^{n}-\mathbf{\Delta z}^T\mathbf{U}_{i-\frac{1}{2}j}^{n}\right]- \\ -(1-\theta)\frac{\Delta t}{\Delta x}\left[\mathbf{\Delta z}^T\mathbf{V}_{ij+\frac{1}{2}}^{n}-\mathbf{\Delta z}^T\mathbf{V}_{ij-\frac{1}{2}}^{n}\right]. \tag{9.31}$$

Once the new free surface location is calculated, the horizontal provisional velocities can be easily determined and inserted in the following equations representing the correction of velocity due to hydrodynamic pressure:

$$u^{n+1}_{i+\frac{1}{2},j,k} = \widetilde{u}^{n+1}_{i+\frac{1}{2},j,k} - \frac{\Delta t}{\Delta x}\left(q^{n+1}_{i+1,j,k} - q^{n+1}_{i,j,k}\right), \tag{9.32}$$

$$v^{n+1}_{i,j+\frac{1}{2},k} = \widetilde{v}^{n+1}_{i,j+\frac{1}{2},k} - \frac{\Delta t}{\Delta x}\left(q^{n+1}_{i,j+1,k} - q^{n+1}_{i,j,k}\right), \tag{9.33}$$

$$w^{n+1}_{i,j,k+\frac{1}{2}} = \widetilde{w}^{n+1}_{i,j,k+\frac{1}{2}} - \frac{\Delta t}{\Delta x}\left(q^{n+1}_{i,j,k+1} - q^{n+1}_{i,j,k}\right). \tag{9.34}$$

For each computational cell the continuity is then imposed:

$$\frac{u^{n+1}_{i+\frac{1}{2}jk}\Delta z^{n+1}_{i+\frac{1}{2}jk} - u^{n+1}_{i-\frac{1}{2}jk}\Delta z^{n+1}_{i-\frac{1}{2}j}}{\Delta x} - \frac{v^{n+1}_{ij+\frac{1}{2}k}\Delta z^{n+1}_{ij+\frac{1}{2}k} - v^{n+1}_{ij-\frac{1}{2}k}\Delta z^{n+1}_{ij-\frac{1}{2}k}}{\Delta y} + w^{n+1}_{i,j,k+\frac{1}{2}} - w^{n}_{i,j,k-\frac{1}{2}} = 0 \tag{9.35}$$

By substituting the equations (9.32), (9.33) and (9.34) in (9.35) we obtain the Poisson equation for the hydrodynamic pressure:

$$\begin{aligned}
&\Delta t\frac{\left(q^{n+1}_{i+1,j,k} - q^{n+1}_{i,j,k}\right)\Delta z^{n+1}_{i+\frac{1}{2}jk} - \left(q^{n+1}_{i,j,k} - q^{n+1}_{i-1,j,k}\right)\Delta z^{n+1}_{i-\frac{1}{2}jk}}{\Delta x^2} + \\
&+\frac{\left(q^{n+1}_{i,j+1,k} - q^{n+1}_{i,j,k}\right)\Delta z^{n+1}_{ij+\frac{1}{2}k} - \left(q^{n+1}_{i,j,k} - q^{n+1}_{i,j-1,k}\right)\Delta z^{n+1}_{ij-\frac{1}{2}k}}{\Delta x^2} + \\
&+\frac{\left(q^{n+1}_{i,j,k+1} - q^{n+1}_{i,j,k}\right)}{\Delta z^{n+1}_{ijk+\frac{1}{2}}} - \frac{\left(q^{n+1}_{i,j,k} - q^{n+1}_{i,j,k-1}\right)}{\Delta z^{n+1}_{ijk-\frac{1}{2}}} = \\
&= \frac{\widetilde{u}^{n+1}_{i+\frac{1}{2}jk}\Delta z^{n+1}_{i+\frac{1}{2}jk} - \widetilde{u}^{n+1}_{i-\frac{1}{2}jk}\Delta z^{n+1}_{i-\frac{1}{2}j}}{\Delta x} + \\
&+\frac{\widetilde{v}^{n+1}_{ij+\frac{1}{2}k}\Delta z^{n+1}_{ij+\frac{1}{2}k} - \widetilde{v}^{n+1}_{ij-\frac{1}{2}k}\Delta z^{n+1}_{ij-\frac{1}{2}k}}{\Delta y} + \widetilde{w}^{n+1}_{i,j,k+\frac{1}{2}} - \widetilde{w}^{n+1}_{i,j,k-\frac{1}{2}}.
\end{aligned} \tag{9.36}$$

This equation constitutes a symmetric epta-diagonal system for the $N_xN_y(N_z-1)$ unknowns $q^{n+1}_{i,j,k}$, which can be solved using the preconditioned conjugate gradient method (Casulli and Stelling, 1998). Once the hydrodynamic pressure $q^{n+1}_{i,j,k}$ is computed, the corresponding velocity field is readly determined by (9.32), (9.33) and (9.34).

Transport equation

The transport scalar equation, representing the advective part of (9.5), can be discretized as follows:

$$\Delta z^n_{i,j,k} S^{n+1}_{i,j,k} - \Delta z^n_{i,j,k} S^n_{i,j,k} + \frac{\Delta t}{\Delta x} \Delta z^n_{i,j,k} \left[u^{n+\theta}_{i+\frac{1}{2}jk} \left(S^n_e\right)_i - u^{n+\theta}_{i-\frac{1}{2}jk} \left(S^n_w\right)_i \right] + \tag{9.37}$$

$$+ \frac{\Delta t}{\Delta y} \Delta z^n_{i,j,k} \left[v^{n+\theta}_{ij+\frac{1}{2}k} \left(S^n_n\right)_j - v^{n+\theta}_{ij-\frac{1}{2}k} \left(S^n_s\right)_j \right] + \Delta t \left[w^{n+\theta}_{ijk+\frac{1}{2}} \left(S^{n+\theta}_{up}\right)_k - v^{n+\theta}_{ijk-\frac{1}{2}} \left(S^{n+\theta}_{low}\right)_k \right] = 0,$$

where S_e, S_w, S_n, S_n, S_u, S_l are unknows values interpolated on the cell faces with respect to East, West, North, South, Upper and Lower sides.

In order to obtain a conservative scheme the following expressions are imposed:

$$\left(S_{low}\right)_k = \left(S_{up}\right)_{k-1}, \left(S_w\right)_i = \left(S_e\right)_{i-1}, \left(S_s\right)_j = \left(S_n\right)_{j-1}. \tag{9.38}$$

Along the vertical direction, in order to reduce the numerical diffusion, the so-called $\beta-$method, namely a linear combination of an Up-Wind scheme and a QUICK scheme, is used to interpolate the concentration to the upper and lower face (Gross, 1998).

The Up-Wind scheme provides:

$$w^{n+\theta}_{k+\frac{1}{2}} S^{n+\theta}_{up} = \frac{w^{n+\theta}_{k+\frac{1}{2}} + \left| w^{n+\theta}_{k+\frac{1}{2}} \right|}{2} \left[\theta S^{n+1}_k + (1-\theta) S^n_k \right] + \tag{9.39}$$

$$+ \frac{w^{n+\theta}_{k+\frac{1}{2}} - \left| w^{n+\theta}_{k+\frac{1}{2}} \right|}{2} \left[\theta S^{n+1}_{k+1} + (1-\theta) S^n_{k+1} \right],$$

while the QUICK scheme gives:

$$w^{n+\theta}_{k+\frac{1}{2}} S^{n+\theta}_{up} = w^{n+\theta}_{k+\frac{1}{2}} \left[\theta \frac{S^{n+1}_k + S^{n+1}_{k+1}}{2} + (1-\theta) \frac{S^n_k + S^n_{k+1}}{2} \right] - \tag{9.40}$$

$$- \frac{S^n_{k-1} - 2S^n_k + S^n_{k+1}}{8} \cdot \frac{w^{n+\theta}_{k+\frac{1}{2}} + \left| w^{n+\theta}_{k+\frac{1}{2}} \right|}{2} - \frac{S^n_k - 2S^n_{k+1} + S^n_{k+2}}{8} \cdot \frac{w^{n+\theta}_{k+\frac{1}{2}} - \left| w^{n+\theta}_{k+\frac{1}{2}} \right|}{2}.$$

The weight of these two contributions is assigned through the β parameter, which is defined in terms of the Courant number c according to the following criterion:

$$\beta = \left\{ \begin{array}{ll} 0 & |c_{\max}| \leq 1 \\ \frac{(|c_{\max}|-1)}{4|c_{\max}|} & 1 \leq |c_{\max}| \leq 3 \\ \frac{(|c_{\max}|-2)}{|c_{\max}|} & |c_{\max}| > 3 \end{array} \right\}, \tag{9.41}$$

where $c_{\max} = \max\left\{\left|c_{k-\frac{1}{2}}\right|, \left|c_{k+\frac{1}{2}}\right|, \left|c_{k+\frac{3}{2}}\right|\right\}$.

Advective horizontal terms are discretized in explicit way because the planimetric dimension of cells is large enough to avoid limiting condition on time step (Rizzi, 1999). Hence, Lax Wendroff algorithm is used, which is made up of an Up-Wind scheme plus another corrective term in order to reduce numerical diffusion.

The latter term can produce spurious oscillations in case of strong scalar gradients; hence a flux-limiter Φ has been introduced to inhibit the above effect:

$$F_{i+\frac{1}{2},j,k} = u^n_{i+\frac{1}{2},j,k} S^n_e = \frac{u^n_{i+\frac{1}{2},j,k} + \left|u^n_{i+\frac{1}{2},j,k}\right|}{2} S^n_{i,j,k} + \frac{u^n_{i+\frac{1}{2},j,k} - \left|u^n_{i+\frac{1}{2},j,k}\right|}{2} S^n_{i+1,j,k} + \tag{9.42}$$
$$+ \Phi_{i+\frac{1}{2},j,k} \frac{1}{2} \left|u^n_{i+\frac{1}{2},j,k}\right| \left(1 - \frac{\Delta t}{\Delta x} \left|u^n_{i+\frac{1}{2},j,k}\right|\right) \left(S^n_{i+1,j,k} - S^n_{i,j,k}\right).$$

Several limiters are available in the literature; in the present formulation a monotonized centered filter is adopted due to its versatility:

$$\Phi(\psi) = \max\left(0, \min\left(\frac{1+\psi}{2}, 2, 2\psi\right)\right), \tag{9.43}$$

where:

$$\psi = \frac{S^n_{I,j,k} - S^n_{I-1,j,k}}{S^n_{i,j,k} - S^n_{i-1,j,k}}, \tag{9.44}$$

and:

$$I = \left\{ \begin{array}{ll} i-1 & if\ u^n_{i+\frac{1}{2},j,k} \geq 0 \\ i+1 & if\ u^n_{i+\frac{1}{2},j,k} \leq 0 \end{array} \right\}. \tag{9.45}$$

In a similar way, discretization in y-direction leads to the following expression:

$$G_{i,j+\frac{1}{2},k} = v^n_{i,j+\frac{1}{2},k} S^n_n. \tag{9.46}$$

Notice that the bidimensional field produces other advective mixed fluxes; they are corrected using the method proposed by Leveque (1996). In case of $(u, v) > 0$ the equation

in y-direction can be corrected as follows:

$$G_{i,j-\frac{1}{2},k} = G_{i,j-\frac{1}{2},k} - \frac{1}{2}\frac{\Delta t}{\Delta x} u^n_{i-\frac{1}{2},j,k} v^n_{i-\frac{1}{2},j,k} \left(S^n_{i,j,k} - S^n_{i-1,j,k}\right) - \tag{9.47}$$
$$-\Phi_{i-\frac{1}{2},j,k} \frac{1}{2}\frac{\Delta t}{\Delta x} v^n_{i-\frac{1}{2},j,k} u^n_{i-\frac{1}{2},j,k} \left(1 - \frac{\Delta t}{\Delta x} u^n_{i-\frac{1}{2},j,k}\right) \left(S^n_{i,j,k} - S^n_{i-1,j,k}\right)$$

Finally, diffusive terms are discretized using the Crank-Nicolson method.

9.2. Test cases

In order to check the correct implementation of the model some test cases have been conducted, trying to reproduce well-known solutions.

The first test concernes the case of a small amplitude non-breaking wave, with relatively large ratio between the total depth and the wave length. In this case the hydrostatic approximation does not hold and the wave celerity can be expressed by:

$$c = \sqrt{\frac{g\lambda}{2\pi} \tanh\left(\frac{2\pi H}{\lambda}\right)}, \tag{9.48}$$

where λ is the wave length and H is the total depth.

The computational domain is described by a cube of length 10m, discretized with regular cells with $\Delta x = \Delta y = \Delta z = 0.5m$. The free surface of the inviscid fluid that fills the basin is imposed with a constant slope $\eta = 0.02x - 0.1$ m.

The displacement of the free surface at the end of the basin is shown in figure 9.2: the wave speed calculated with the hydrostatic approximation doesn't conform to the analytical solution expressed by the dispersion relation (9.48) while the solution obtained through the quasi-non-hydrostatic model reproduces the analytical solution fairly well.

The second test refers to an uni-nodal standing wave in a rectangular basin, with inviscid fluid and slip condition at the bed.

The governing differential equations are:

$$\frac{\partial Q}{\partial t} = g\left(h + \eta\right)\frac{\partial \eta}{\partial x}, \tag{9.49}$$

$$\frac{\partial \eta}{\partial t} + \frac{\partial Q}{\partial x} = 0, \tag{9.50}$$

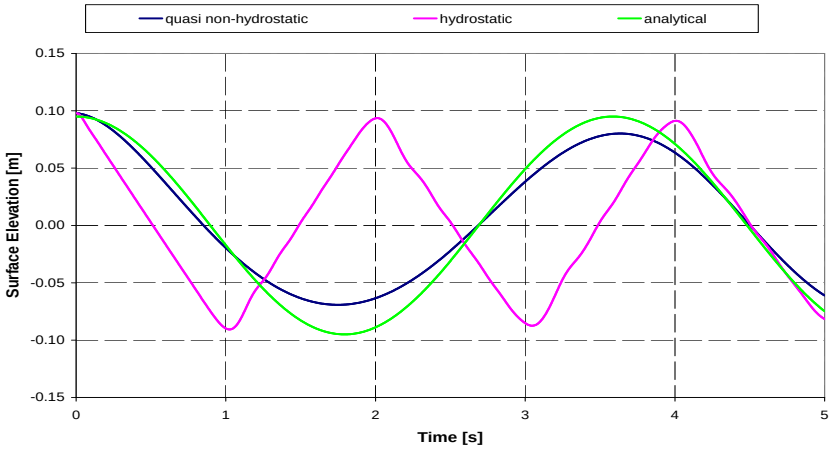

Figure 9.2.: Free-surface waves of small amplitude.

$$\frac{\partial U}{\partial t} + g\frac{\partial \eta}{\partial x} = 0, \tag{9.51}$$

$$\frac{\partial W}{\partial z} + \frac{\partial U}{\partial x} = 0, \tag{9.52}$$

where Q is the discharge and U the average velocity. The standing wave is introduced as a given water elevation at one boundary: a cosine wave with an amplitude of $0.4m$ at the left-hand boundary, where the velocity is set equal to zero.

The analytical solution, in this case, is given by:

$$\eta = A\ \cos(kx)\cos(\omega t)\,, \tag{9.53}$$

$$U = \left(A\frac{C_o}{h}\right)\sin(kx)\sin(\omega t)\,, \tag{9.54}$$

where k is the wave number $\left(=\frac{2\pi}{L}\right)$, L is the wave length, C_o is the wave celerity $\left(=\sqrt{gh}\right)$ and $\omega = k\ C_o$. The comparison in terms of the estimated values of water elevation and velocity on a domain 3962 m long and 10 m deep, with a period of complete oscillation of 800 s, displays a fairly good agreement between numerical and analytical solution, though numerical results seem to diverge more rapidly from the exact solution as the simulation proceeds than the solution developed by Falconer and Cox (1988) (see figures 9.3 and 9.4).

The third example is the classical "lock-exchange" problem: a rectangular basin 2 m long

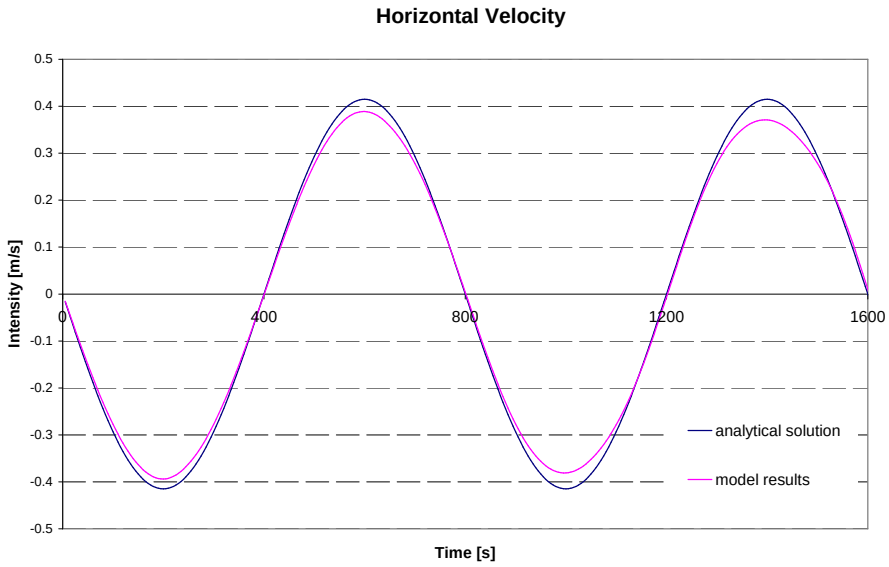

Figure 9.3.: Uni-nodal standing wave: comparison between numerical and analytical predicitions of velocity.

and 0.3 m deep is initially filled with two fluids characterized by different density, separated by a vertical dam. The fluid located in the left part is cold (and presents a density equal to 999.97 $kg\ m^{-3}$) while in the right part the box is filled by a warm fluid with density equal to 979.77 $kg\ m^{-3}$. The initial velocities are zero, eddy viscosity $\upsilon^t = 10^{-4} m^2/s$, and the discretization parameter are $\Delta x = \Delta y = 0.07\ m$ and $\Delta z = 0.01\ m$, with $\Delta t = 0.01 s$. Once the dam is removed, the solution displays a more discontinuos character in the case of the hydrostatic assumption (figure 9.5).

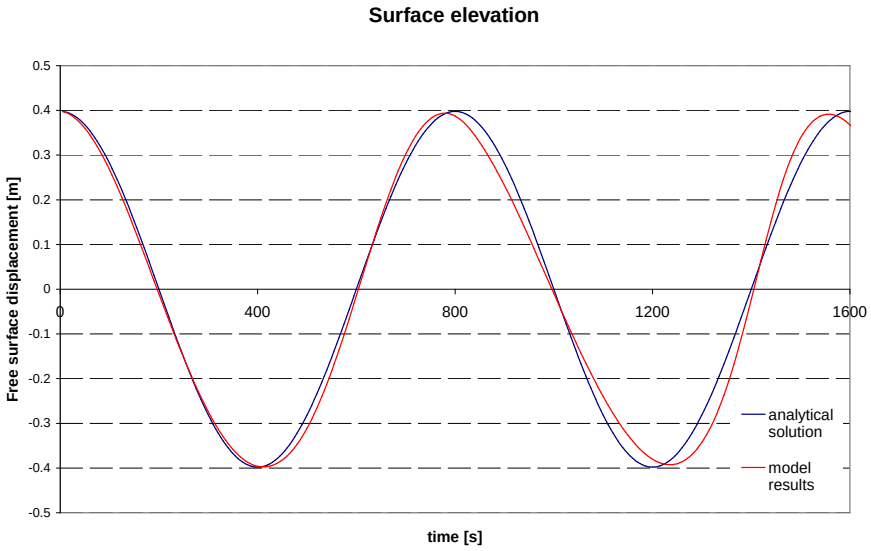

Figure 9.4.: Comparison between numerical and analytical predictions of free surface displacement.

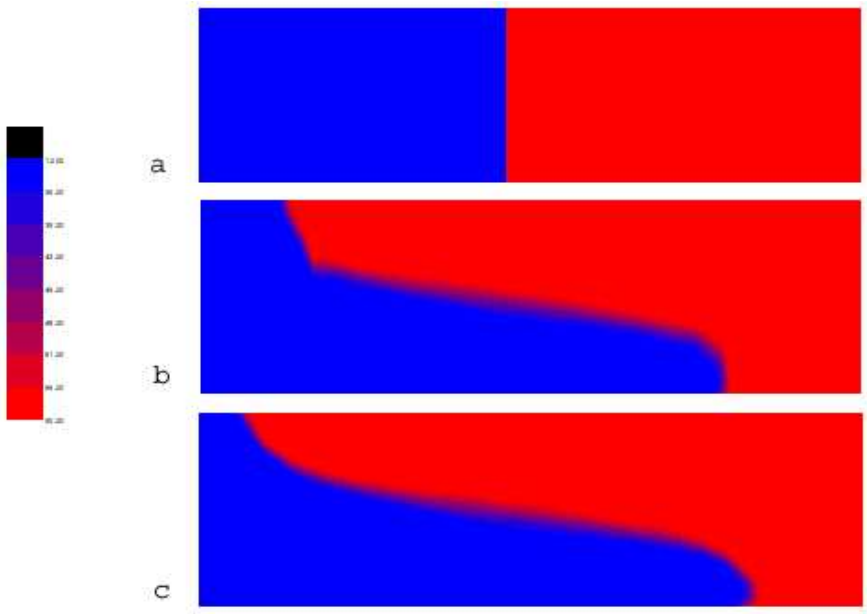

Figure 9.5.: Baroclinic circulation: (a) initial condition; (b) hydrostatic approximation (c) hydrodynamic pressure correction, after $t = 9s$.

9.3. Simulation

The physical domain of Tovel lake has been reproduced using a grid made up by $N_x = 104 \cdot N_y = 86 \cdot N_z = 50$ rectangular cells characterized by fixed length Δx and width Δy equal to $10m$, and with thickness Δz_k variable from 2 m in hypolimnion to 20 cm in epilimnion and metalimnion.

The batimetry of the lake is represented in figure 9.6:

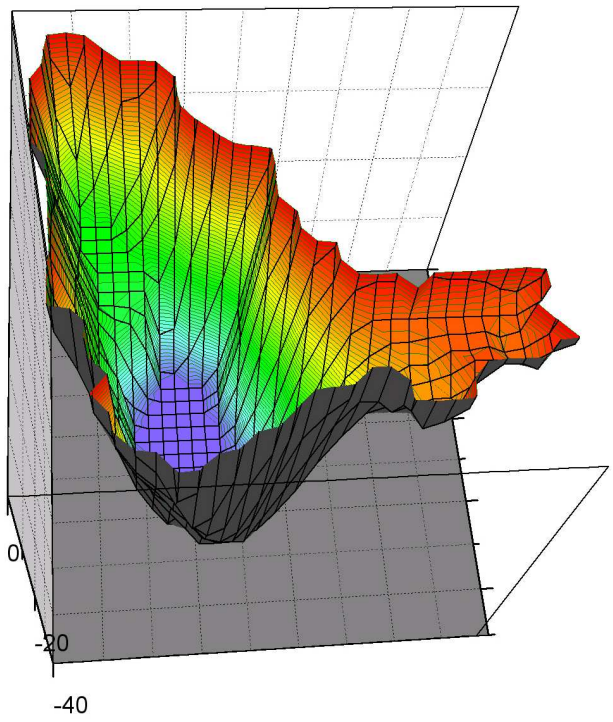

Figure 9.6.: Lake Tovel computational domain.

The Red Bay is located in the right part of figure 9.6: it is well distinguishable as well as the gulf located before the slope that joins the shallow part with the deeper interior lake.

In the following we focus the attention on the hydrodynamic pattern induced by wind: in particular, we investigate flow exchanges between Red Bay and the main lake.

The numerical simulations cover two different periods, corrisponding to those covered by field measurements through ADCP (chapter 5), in order to check the performance of the model on complex topography.

The wind field has been imposed using 5 weather stations; two of them correspond to

actual stations (belonging to the University of Trento and to the "Istituto Agrario di San Michele all'Adige", respectively), while three are are fictitious and are used to simulate the presence of sheltered zones (see figure 9.7).

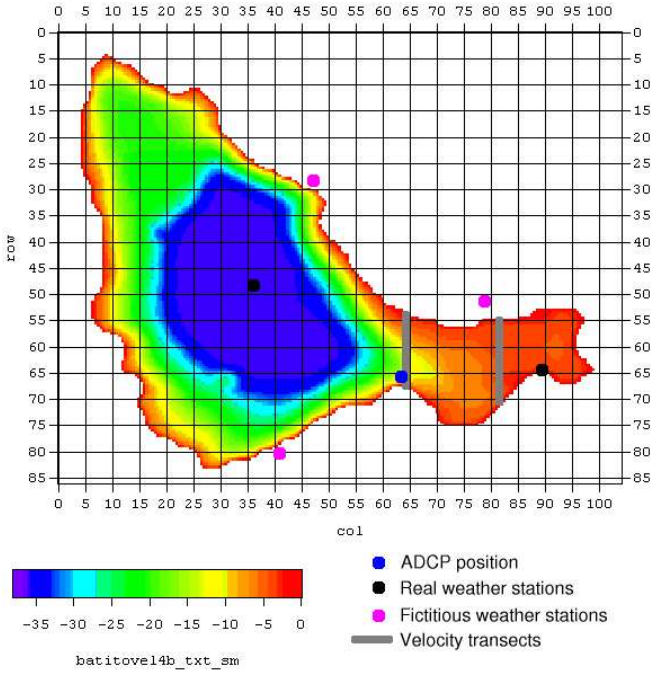

Figure 9.7.: Lake Tovel planimetric domain discretized in cells.

9.3.1. First simulation

The first simulation corresponds to a period of strong stratification, when the free surface level is still high (roughly 1177,5 m a.m.s.l.) and the wind blows quite strongly.

The simulation starts on July 18th, at midday, and finishes after 72 hours, on July 21st.

Since the ADCP instrument measured the velocities on the water column roughly corresponding to cell (i=68, j=65), results of the model refer to that point.

Measured and computed results are quite similar, as shown in figure 9.8. In fact, neglecting the upper and lower zones not covered by ADCP due to strong echo effects, the predicition of velocity direction is fairly satisfactory, the disagreement being possibly due to inaccuracy of topographic survey or weather conditions reconstruction. The model results support the idea that flow in Tovel lake develops along the main lake direction; furthermore currents do not respond instantaneously to wind forcing: in fact, both the model and

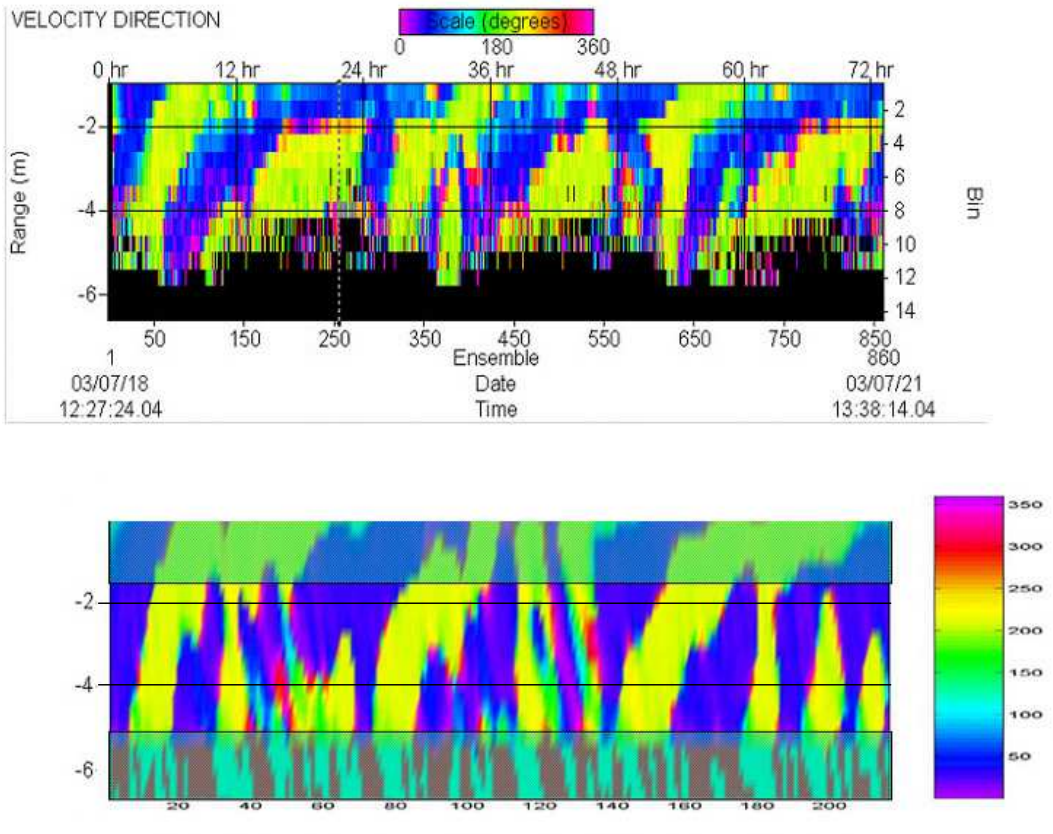

Figure 9.8.: Comparison between measured and simulated velocity direction from July 18th to 21st.

field data suggest that the circulation moves in opposite direction with respect to wind direction.

Model results suggest the importance of baroclinic terms, which are responsible for the propagation of internal waves and account for the isopycnal surfaces tilting: numerical tests carried out without these terms lead to results which differ strongly from observed data.

The model reveals that direction change begins at the bottom, because the adjustement of lake to internal gravity dominates, for most of the time, the external forces.

The velocity direction simulated along a cross-sectional transect displays a different behaviour depending upon lake topography, as shown in figure 9.9, where counterflowing motion is displayed not only along the vertical but also on horizontal surface layers.

The figure 9.10 shows the tilting of isopycnal surfaces, with accumulation of warm waters

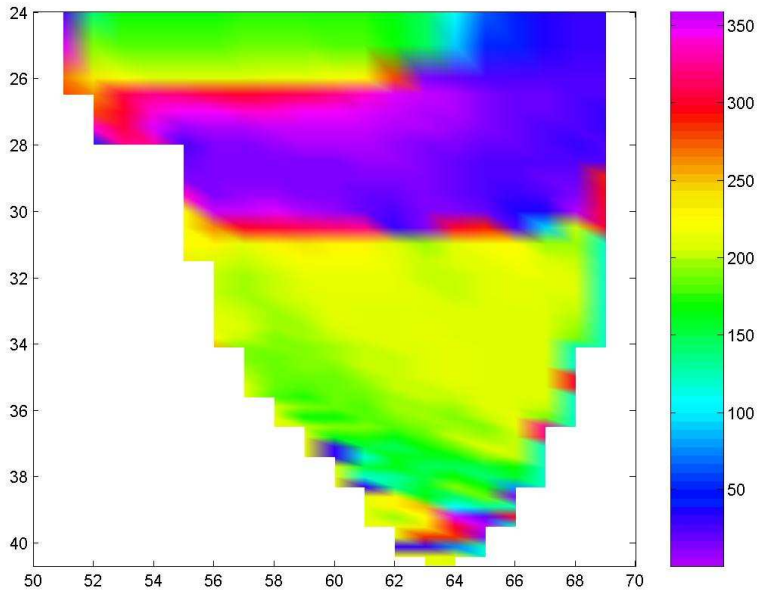

Figure 9.9.: Section of the lake along cells i=68 representing velocity directions

in the downwind end. The internal layers undergo both stretching and squeezing, as it is typical of a seiche vertical mode greater than one.

The figure 9.11 shows a multiple inversion of velocity profile; in the figure velocity is directed to the North at the surface, because of nocturnal breeze. $1 \div 1.5\ m$ below the surface we can distinguish a first inversion; below $3 \div 4\ m$ another inversion occurs. It is worth to note the complexity of the velocity field that developes at the "joining slope zone", where the ADCP has been positioned.

Finally, the behaviour of free surface and isopycnal surface corresponding to 14 °C are reproduced in figures 9.12 and 9.13. The isopycnal surface has been reconstructed by means of linear interpolation using temperature values computed at cell centres.

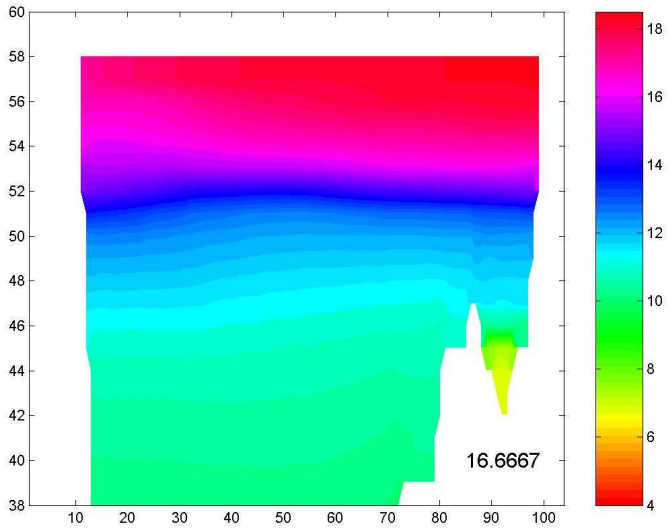

Figure 9.10.: Vertical section of the upper part of Lake Tovel: temperature field.

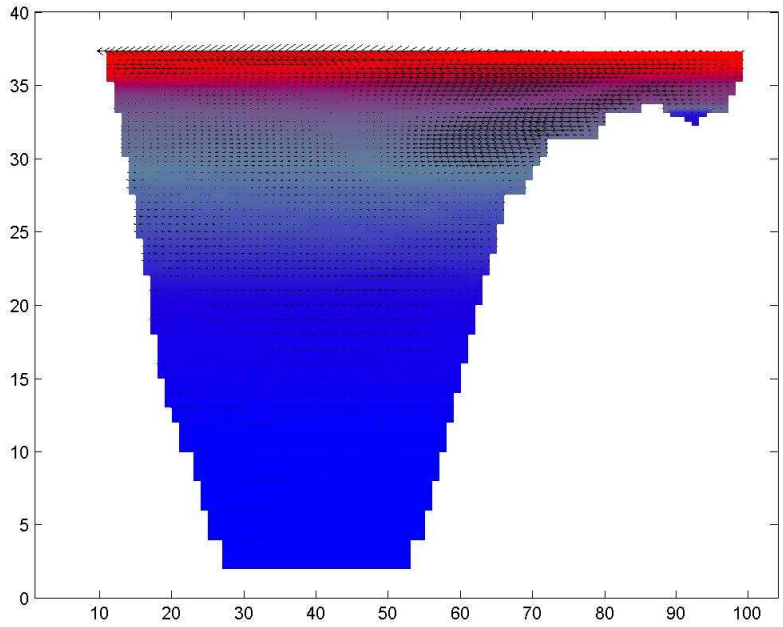

Figure 9.11.: Vertical section of Lake Tovel: velocity field.

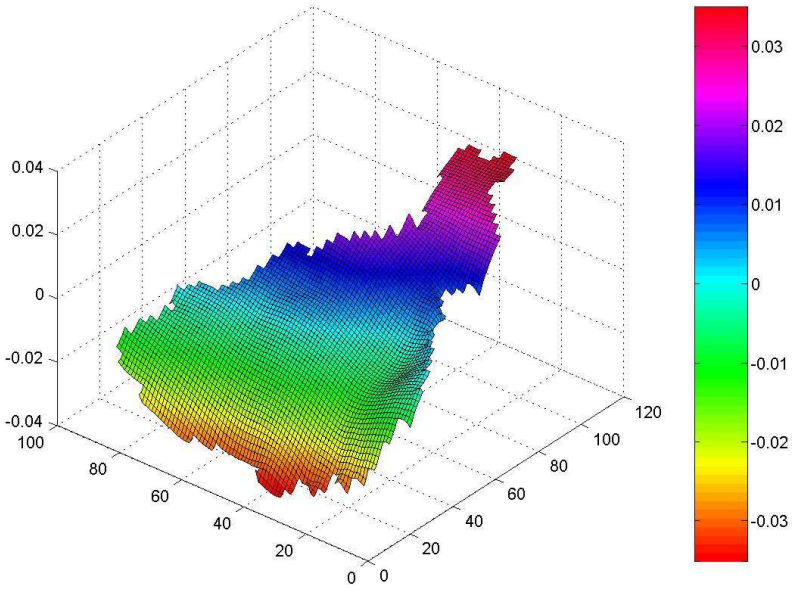

Figure 9.12.: Altimetric behaviour of free surface.

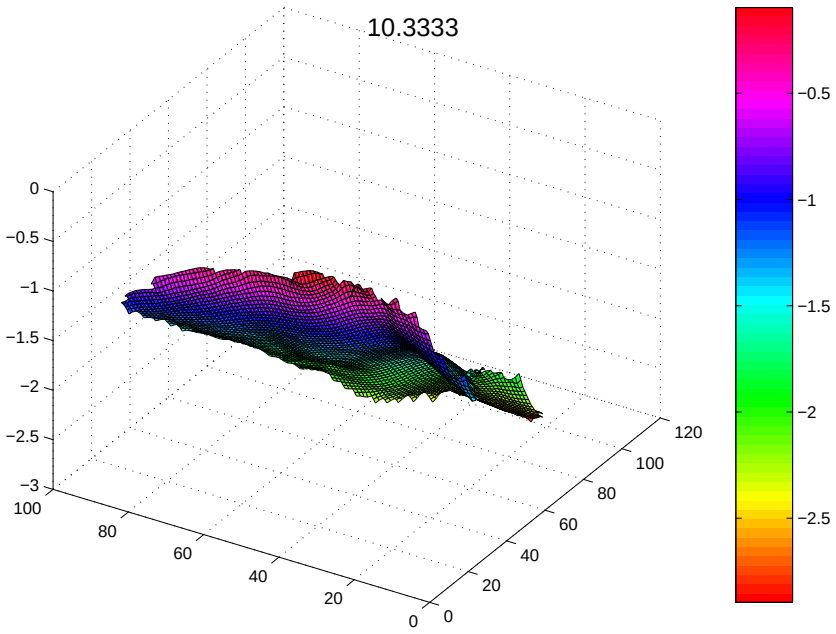

Figure 9.13.: Altimetric behaviour of isopycnal surface corresponding to 14 °C.

9.3.2. Second simulation

Since the ADCP has been positioned in the same place in October, when the stratification of the lake was very weak and the water level low, another simulation has been performed with reference to that period of observation.

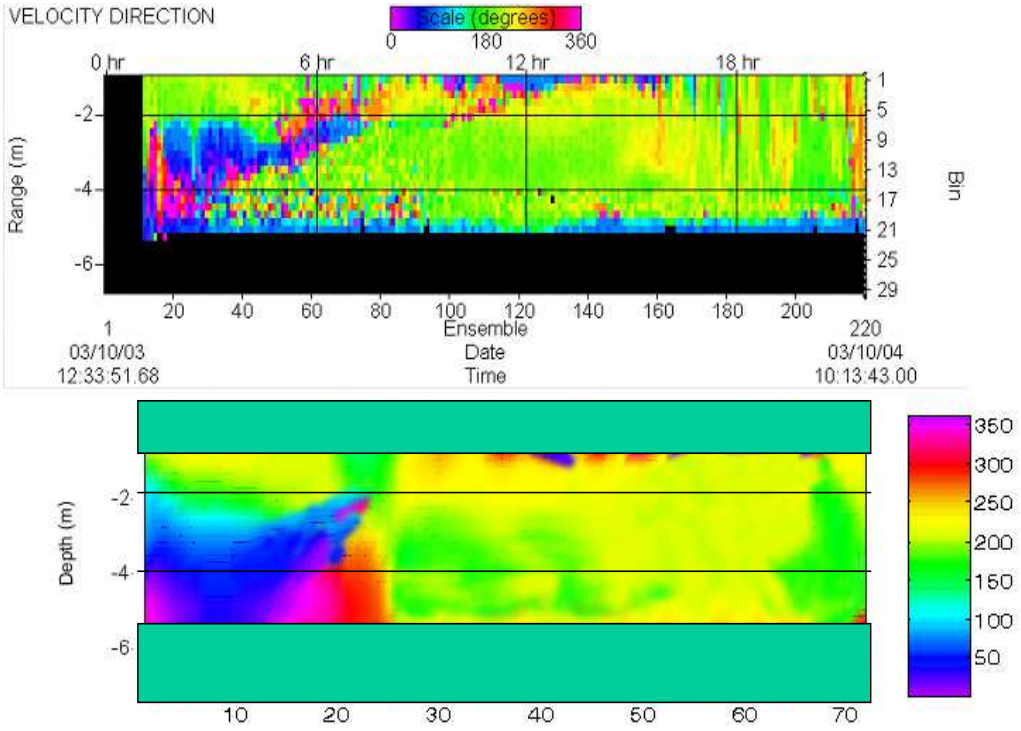

Figure 9.14.: Comparison between measured and simulated velocity direction from 3rd to 4th October.

Figure 9.15 displays the behaviour of the superficial velocity field at 12:00 obtained by averaging the value of velocity within the first meter below the surface. It is possible to divide the lake in two parts: in the Southern part velocities are directed towards the Red Bay, while in the Northern part flow goes in the opposite direction. As the wind changes direction, nearly at 17:00, the velocities in the whole lake change direction towards the North, with a certain time lag (see figure 9.16).

As night is approaching the velocity field exhibits four zones of vorticity (see figure 9.17) which tend to join together in the subsequent morning, before the start of the breeze flowing up-valley (see figure 9.18).

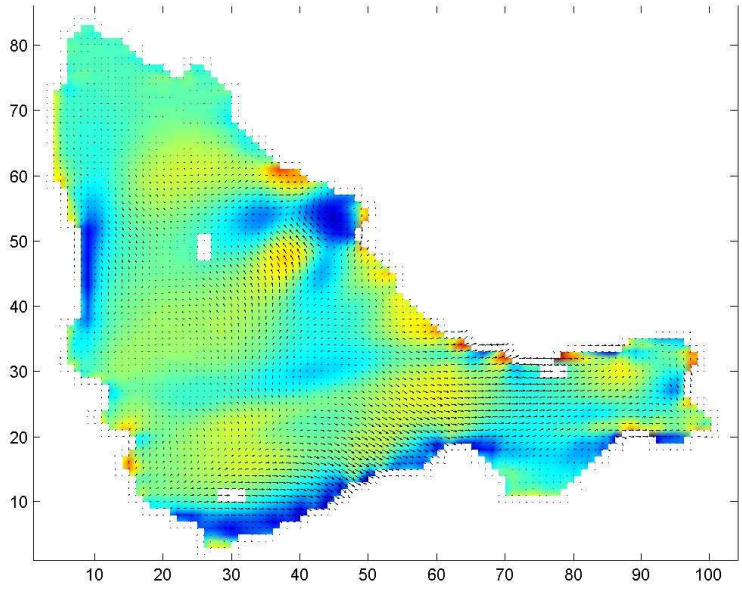

Figure 9.15.: Superficial velocity field at 12AM.

Finally, a section located in front of the Red Bay is represented in figure 9.19. In the afternoon we can distinguish a superficial circulation entering the Red Bay from the Western part and outgoing from the Eastern part. At the depth of 1 m below the surface velocities are directed towards the North. Under these conditions the passive transport could be important in accumulating in Red Bay red algae floating on the water surface.

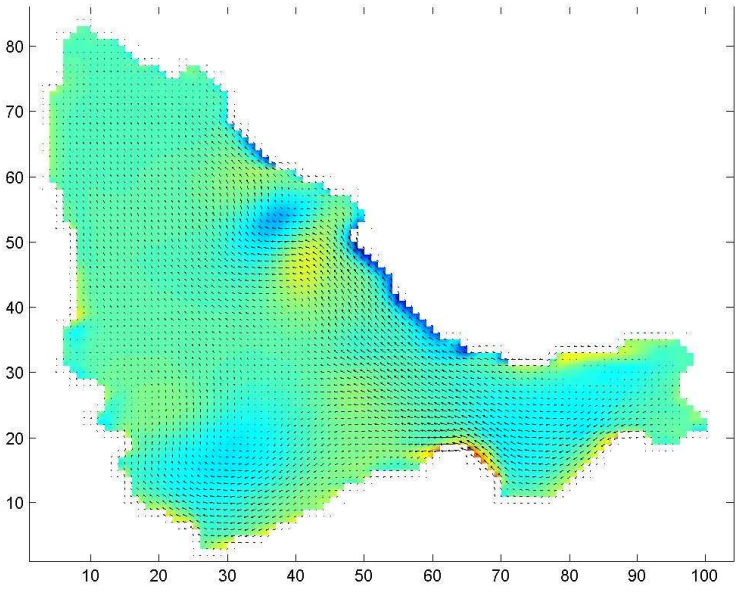

Figure 9.16.: Superficial velocity field at 5PM.

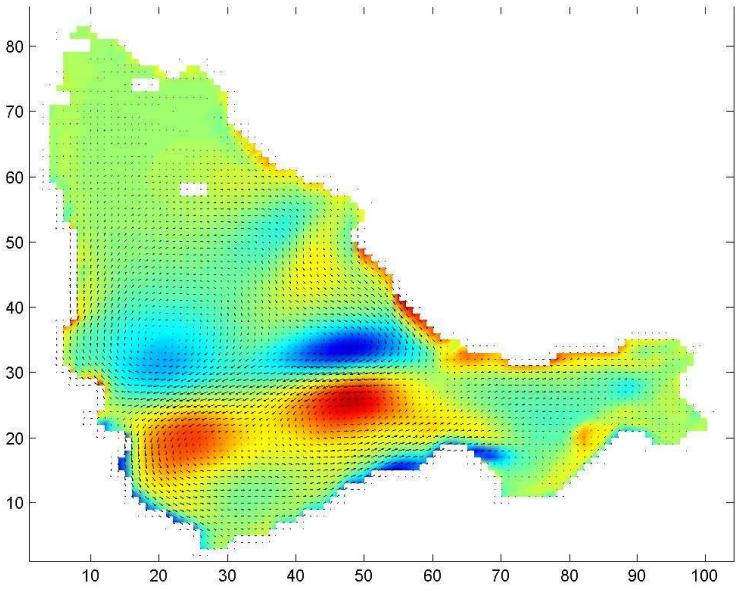

Figure 9.17.: Superficial velocity field at 8PM.

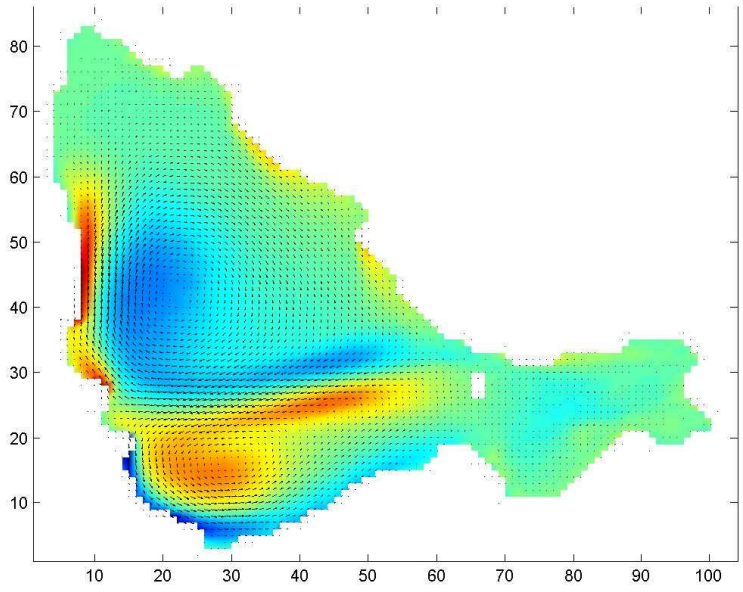

Figure 9.18.: Superficial velocity field at 6AM.

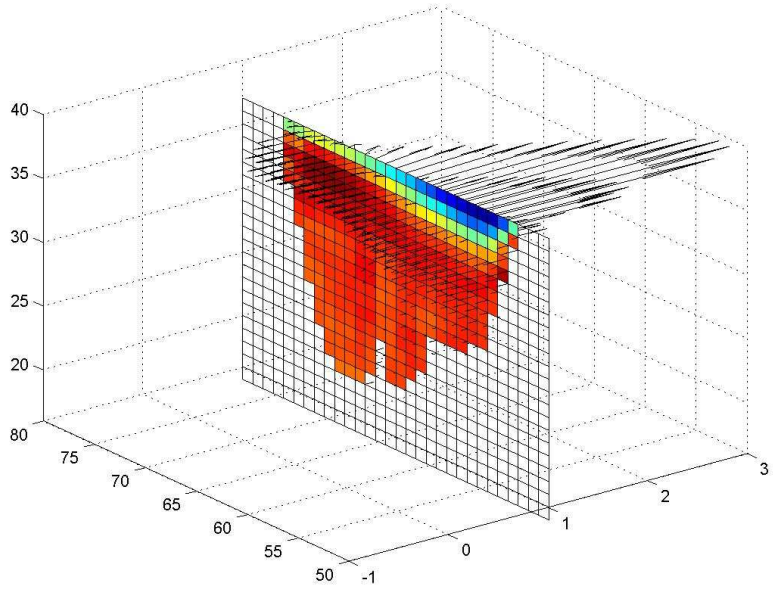

Figure 9.19.: 3D representation of velocity field at the mouth of Red Bay.

Bibliography

J. Antenucci and J. Imberger. On internal waves near the high frequency limit in an enclosed basin. *Journal of Geophysical Research (Oceans)*, 106:22465–22474, 2001.

J. P. Antenucci and A. Imerito. *The CWR Dynamic Reservoir Simulation Model (DYRESM).* University of Western Australia, 2001.

A. Cacciatori. *Analysis of the Non-Dimensional Numbers.* Master's Thesis, University of Padova, 2000.

V. Casulli. A semi-implicit finite difference method for non-hydrostatic, free-surface flows. *Numer. Methods Fluids*, pages 425–440, 1999.

V. Casulli and E. Cattani. Stability, accuracy and efficiency of a semi-implicit method for three-dimensional shallow water flow. *Comput. Math. Appl.*, pages 99–112, 1994.

V. Casulli and R. Cheng. Semi-implicit finite difference methods for three-dimensional shallow water flow. *Numer. Methods Fluids*, pages 629–648, 1992.

V. Casulli and G. S. Stelling. Numerical simulation of 3d quasi-hydrostatic, free-surface flows. *Hydraul. Eng.*, pages 678–686, 1998.

M. De Franceschi, A. Marzadro, and D. Zardi. Local meteorology over a small alpine lake. In *Proceedings of 27th International Conference on Alpine Meteorology and MAP-Meeting 2003*, 2003.

G. H. Goudsmit, F. Peters, M. Gloor, and A. Wuest. Boundary versus diapycnal mixing in stratified natural waters. *J. Geophysical Research*, pages 903–914, 1997.

E. S. Gross. A semi-implicit method for vertical transport in multidimensional models. *Numer. Meth. Fluids*, pages 157–186, 1998.

D. P. Hamilton and S. G. Schladow. Prediction of water quality in lakes and reservoirs. *Ecological Modelling*, pages 91–110, 1996.

B. Henderson-Sellers. Role of eddy diffusivity in thermocline formation. *Environmental Engineering Division*, pages 517–531, 1976.

B. R. Hodges, J. Imberger, B. Laval, and J. Appt. Modeling the hydrodynamics of stratified lakes. *Hydroinformatics J.*, pages 101–104, 2000.

D. A. Horn, J. Imberger, and G. Ivey. The degeneration of large scale interfacial gravity waves in lakes. *J. Fluid Mech.*, pages 181–207, 2001.

G. Hutchinson. *A Treatise of Limnology.* John Wiley and Sons, 1957.

K. Hutter. *Hydrodynamics of lakes.* CISM, Italy, 1984.

J. Imberger. *Limnology Now.* Margalef, 1994.

J. Imberger. Mixing and turbulent fluxes in the metalimnion of a stratified lake. *Limnology and Oceanography*, pages 392–409, 2001.

J. Imberger. Thermal characteristics of standing waves: An illustration of dynamic processes. In *Hydrobiologia*, pages 7–29, 1985a.

J. Imberger. The diurnal mixed layer. *Limnology and Oceanography*, 30(4):737–770, 1985b.

J. Imberger. Characterizing the dynamical regimes of a lake. In *Handbook.* CWR, University of Western Australia, 1999.

J. Imberger and P. F. Hamblin. Dynamics of lakes, reservoirs and cooling ponds. *J. Fluid Mech.*, pages 153–187, 1982.

J. Imberger and J. Patterson. *Physical Limnology.* Academic Press, 1990.

J. Imberger and J. C. Patterson. *A Dynamic Reservoir Simulation Model*, pages 310–361. Fischer, H. B., 1980.

D. Imboden and A. Wuest. *Physics and Chemistry of Lakes.* Springer-Verlag, 1995.

D. Johnson, R. Stocker, R. Head, J. Imberger, and C. Pattiarchi. *A Compact, Low-Cost GPS Drifter for Use in the Oceanic Nearshore Zone, Lakes and Estuaries.* CWR, Western Australia University, 2001.

W. Lewis. Tropical limnology. *Ecological Systems*, pages 159–184, 1987.

W. M. Lewis. Basis for protection and management of tropical lakes. In *Lakes and Reservoirs: Research and Management*, pages 159–184, 2000.

J. L. Martin and S. C. McCutcheon. *Hydrodynamics and Transport for Water Quality Modeling.* Lewis Publishers, 1999.

S. G. Monismith. Wind-forced motions in stratified lakes and their effects on mixed-layer shear. *Limnology and Oceanography*, pages 771–783, 1985.

M. E. A. Munnich. Observations of the second vertical mode of the internal seiche in an alpine lake. *Limnol. Oceanogr.*, pages 1705–1719, 1992.

R. Ragotzkie. *Lakes: Chemistry, Geology and Physics.* Springer-Verlag, 1978.

RDI. *Acoustic Doppler Current Profilers: Principles of Operation.* RD Instruments, California, USA, 1996.

G. Rizzi. *Un Modello Idrotermodinamico Per Piccoli Laghi: Applicazione al Caso Del Lago Di Serraia.* Master's thesis, University of Trento, 1999.

E. Roget and J. Colomer. Flow characteristics of a gravity current induced by differential cooling in a small lake. *Aquatic Sciences*, pages 367–377, 1996.

A. Saggio and J. Imberger. Internal wave weather in a stratified lake. *Limnology and Oceanography*, 43(8):1780–1795, 1998.

Son-Tek. *Acoustic Doppler Velocimeter Ocean Probe: Technical Manual.* Son Tek/YSI, USA, 1996.

D. H. N. Spence. *Light Quality and Plant Response under Water.* Academic Press, New York, 1981.

R. Stocker and J. Imberger. Horizontal dispersion in the surface layer of a stratified lake. *Limnology and Oceanography, submitted*, 2002.

J. J. Sturman, C. E. Hodham, and G. N. Ivey. Steady convective exchange flows down slopes. *Aquatic Sciences*, pages 260–278, 1999.

R. Thompson and J. Imberger. Response of a numerical model of a stratified lake to wind stress. In *Second International Symposium on Stratified Flows*, 1980.

J. Tobias, A. Wuest, A. Stips, and W. Eugster. Observation of a quasi shear-free lacustrine convective boundary layer. *J. Geophysical Research, submitted*, 2002.

M. Tonetta. *Analisi Sperimentale e Caratterizzazione Idrotermodinamica Del Lago Di Tovel.* Master's Thesis, University of Trento, 2003.

V. Tonolli. *Introduzione Allo Studio Della Limnologia.* Istituto Italiano di Idrobiologia, 1964.

R. G. Wetzel. *Limnology.* Saunders College Publishing, 1983.

D. Williams. Determination of light extinction coefficients in lakes and reservoirs. In *Surface Water Impoundments.* ASCE, 1980.